# NUMERICAL MODELLING OF COLD CRUCIBLE INDUCTION MELTING (CCIM) PROCESS AND FABRICATION OF HIGH VALUE ADDED COMPONENTS OF TITANIUM AND ITS ALLOYS

ION QUINTANA AZPIAZU

Supervisors:

Dr. Zigor Azpilgain

Dr. David Pardo


A thesis submitted for the degree of

Doctor por Mondragon Unibertsitatea

Mechanical and Manufacturing Department

Mondragon Unibertsitatea

10 December 2013

# PREFACE

Declaration

I hereby declare that this dissertation is the result of my own work and that, to the best of my knowledge and belief, no part of this dissertation has been previously submitted for any similar qualification or degree.

*Ion Quintana*

(December 2013)

# ACKNOWLEDGMENTS

Quiero dar las gracias a todas esas personas e instituciones que me han acompañado durante todo este tiempo y que han hecho posible que esta tesis viera la luz.

En primer lugar, quiero dar las gracias a toda mi familia por su cariño y paciencia. Por haberme educado de la forma que lo han hecho. Quisiera agradecer a mis directores de tesis Dr. Zigor Azpilgain y Dr. David Pardo por su dirección, ayuda y consejos. Quisiera también agradecer a la línea de procesos avanzados de conformación de materiales por haberme dado la oportunidad de realizar esta tesis.

I would like to acknowledge Prof. Egbert Baake from Institute of Electrotechnology Leibniz University Hannover for the opportunity he gave me to spend three months with him on a doctoral stay there and for everyday support.

También quisiera agradecer a todos los amigos, compañeros y trabajadores que me han acompañado en esta etapa de mi vida. No empezaré a agradecer personalmente a cada uno de ellos, ya que me olvidaría de alguno. Solamente agradecerles por estar allí tanto en los buenos como en malos momentos, por sus aportaciones científicas y no tan científicas, por dar un motivo para venir feliz a trabajar. Solamente decir a todos ellos que las huellas de las personas que caminaron juntos nunca se borran.

Mil esker bihotzez danoi.

*Ama,*

*zaila da zu ez ikusten,*

*ez entzuten*

*eta ez sentitzen ohitzea,*

*baina erraza da zu maitatzen jarraitzea.*

# ABSTRACT (ENGLISH VERSION)

This dissertation concerns the development of a numerical modelling of cold crucible induction melting (CCIM) and the fabrication of high value added components of titanium and its alloys.

Titanium and its alloys have emerged as a very attractive metal for numerous applications: medical prostheses, aerospace industry, automotive industry, power generation, sport equipment, and marine engineering. The reason lie in their attractive properties, such as excellent biocompatibility, high specific strength, excellent corrosion resistance, excellent high temperature creep resistance, and good fracture toughness. However, the application of titanium is often limited by its relatively high cost. This high cost of titanium makes casting very attractive route. However, is it difficult to cast these alloys by conventional casting techniques because of the titanium reactivity at high temperatures, which reacts with the crucible and mould components. The CCIM process is currently the most effective means of melting these alloys.

The CCIM is an innovative process to melt high melting point reactive materials such as titanium alloys. The melting and casting of the material is performed in vacuum or in a protective atmosphere in order to prevent any contamination of the charge. Moreover, a water cooled segmented crucible is used instead of a ceramic crucible to avoid any kind of reaction among the charge and the crucible. The magnetic field generated by an external coil penetrates through the slits of the crucible and generates induced currents in the charge, which are responsible of melting it due to Joule heating.

The drawbacks of this process are the poor efficiency due to great percentage of heat that is removed by the cooling system and the small superheat of the melt, which can cause solidification problems.

In this dissertation, we have selected the CCIM process to melt and cast titanium alloys. The aim of this dissertation consists on increasing the scientific knowledge about the CCIM process by means of both a numerical and an experimental approach.

The main part of the dissertation focuses on the development of a numerical modelling of CCIM to optimize of the main parameters of the process. The task of optimizing melt superheat faces the challenge of finding optimal combination of crucible height to diameter ratio, number of inductor turns, crucible

design, current strength, and frequency. Variation of any of the after mentioned factors influences the shape of melt meniscus and, as a result, flow pattern and energy balance. The second part deals with the set-up of an installation of CCIM and the fabrications of titanium components.

As a result of the present work some goals have been achieved, being the most important:

a) Development of numerical modelling of CCIM,

b) setting up of a CCIM installation, and

c) casting of titanium parts.

# ABSTRACT (SPANISH VERSION)

Esta tesis trata sobre el desarrollo de un modelo numérico del “cold crucible induction melting (CCIM)” y la fabricación de componentes de alto valor añadido de titanio y sus aleaciones mediante este proceso.

El titanio y sus aleaciones se han convertido en un metal muy atractivo para numerosas aplicaciones: prótesis médicas, industria aeroespacial, industria de automoción, generación de energía, deporte e ingeniería marina. La razón radica en sus propiedades atractivas, tales como excelente biocompatibilidad, alta resistencia específica, excelente resistencia a la corrosión, excelente resistencia a la fluencia a alta temperatura y buena resistencia a la fractura. Sin embargo, la aplicación de titanio es a menudo limitada por su coste relativamente alto. Los procesos de fundición conducen a productos de menores costes. Sin embargo, es difícil fundir estas aleaciones por técnicas de moldeo convencionales, debido a la reactividad de titanio a altas temperaturas, que reacciona con el crisol y molde. El proceso CCIM es actualmente el medio más eficaz de fusión de estas aleaciones.

El CCIM es un proceso innovador en la que la fusión y colada del material se realiza bajo vacío o dentro de una atmósfera protectora y donde se utiliza un crisol refrigerado segmentado de cobre en vez de los habituales crisoles cerámicos para evitar cualquier tipo de reacción entre la carga y el crisol. El campo magnético generado por una bobina externa penetra a través de las ranuras del crisol y genera corrientes inducidas en la carga, las cuales son las responsables de la fusión debido al calentamiento Joule.

Los inconvenientes de este proceso son la baja eficiencia debido al gran porcentaje de calor que se elimina por el sistema de refrigeración y el pequeño sobrecalentamiento del metal fundido, que puede causar problemas de solidificación.

En esta tesis, hemos seleccionado el proceso CCIM para fundir y colar las aleaciones de titanio. El objetivo de esta tesis consiste en aumentar el conocimiento científico sobre el proceso CCIM tanto de un modo numérico como un modo experimental.

La parte principal de la tesis se centra en el desarrollo de un modelo numérico de CCIM para optimizar de los principales parámetros del proceso. La tarea de optimizar sobrecalentamiento se enfrenta al reto de encontrar la combinación óptima de la altura del crisol a diámetro, número de espiras del inductor, diseño

del crisol, intensidad de corriente y frecuencia. La variación de cualquiera de los factores mencionados influye en la forma del menisco del metal líquido y, como resultado, el patrón del fluido y el balance de energía. La segunda parte trata de la puesta en marcha de una instalación de CCIM y la fabricación de componentes de alto valor añadido de titanio.

Como resultado de este trabajo se han logrado algunos objetivos, siendo los más importantes:

a) Desarrollo de modelos numéricos del CCIM.

b) Puesta a punto de una instalación CCIM.

c) Fundición de piezas de titanio.

# ABSTRACT (BASQUE VERSION)

Tesi honek “Cold crucible induction melting (CCIM)” prozesuaren simulazio numerikoaren gainean eta prozesu honen bidez titaniozko balio erantsi altuko osagaiak ekoizteko modua tratatzen du.

Titanioak eta bere aleazioek interes handia sortu dute aplikazio industrial askotan: mediku protesiak, aeronautika, automozioa, energia generazioa, kirol ekipamendua eta itsas ingeniaritza. Arrazoia bere ezaugarri erakargarrietan errotzen da: biokonpatibilitate bikaina, erresistentzia espezifiko altua, korrosioaren aurkako erresistentzia ezin hobea, tenperatura alturako isurpenaren aurkako erresistentzia paregabea eta hausturaren aurkako erresistentzia. Hala ere, bere kostu altuak bere aplikazioak murrizten ditu. Galdaketa-prozesuek kostu txikiagoko produktuetara daramate. Hala ere, zaila da aleazio hauek galdaketa prozesu konbentzionalekin urtzea, tenperatura handitan erreaktibotasun handia daukate eta. CCIM prozesua aleazio hauek galdatzeko prozesu eraginkorren arten dago gaur egun.

CCIM prozesua material erreaktiboak urtzeko prozesu berritzailea da. Bai urtze bai galdaketa hutsean edo atmosfera babesle baten egiten da materialaren erreakzioa saihesteko. Gainera, ohiko zeramikozko arragoen ordez segmentudun kobrezko arragoa erabiltzen da. Kanpoko harilak sortutako kanpo magnetikoa arragoaren arteketatik barneratzen da eta indukziozko korronteak sortzen ditu kargan, karga bera urtuz Joule beroketagatik.

Prozesu honen arazoak efizientzia eskasa (hozte sistemak xurgatzen duen beroagatik) eta solidotze-arazoak eragin ditzakeen gainberotze txikia dira.

Tesi honetan, CCIM prozesua aukeratu dugu titaniozko aleazioak galdaketa prozesuaren bidez fabrikatzeko. Tesi honen helburua CCIM prozesuaren gaineko ezaguera zientifikoa handitzean datza bai ikuspegi teorikoa bai ikuspegi esperimentala erabiliz.

Tesiko alderdi nagusia prozesuaren parametro nagusiak optimizatzeko CCIM prozesuaren zenbakizko modelizazioaren garapenaran gainean tratatzen du. Gainberotze tenperatura optimizatzeko zeregina arragoaren altura diametro ratioa, harilaren espira kopurua, arragoaren diseinua, korrontea eta frekuentziaren balio optimoa aurkitzean datza. Aipatutako faktoreen edozein aldaketek meniskoaren

egoeran eragiten du, eta ondorioz, jariakinaren patroian eta energi balantzean. Tesiaren bigarren atalak CCIM instalazio bat abiarazteaz eta titaniozko osagaiak fabrikatzeaz dihardu

Lan honen emaitz garrantzitsuenak hurrengokoak dira:

a) CCIM prozesuaren modelo numerikoaren garapena.

b) CCIM prozesuaren instalazio baten abiaraztea.

c) Titaniozko piezen galdaketa.

# CONTENTS

**Preface** ..... **iii**

**Acknowledgments** ..... **v**

**Abstract (English version)** ..... **ix**

**Abstract (Spanish version)** ..... **xi**

**Abstract (Basque version)** ..... **xiii**

**Contents** ..... **xv**

**List of tables** ..... **xix**

**List of figures** ..... **xxi**

**Glossary** ..... **xxiii**

**1 Introduction** ..... **1**

1.1 Motivation and background ..... 1

1.2 Objectives ..... 2

1.3 Outline of the present dissertation ..... 3

**2 Casting processes of titanium** ..... **5**

2.1 Introduction ..... 5

2.2 Process I: VIM ..... 6

2.3 Process II: VAR ..... 9

2.4 Process III: ESR ..... 11

2.5 Process IV: Triple melt ..... 12

2.6 Process V: EBM ..... 12

2.7 Process VI: PAM ..... 14

2.8 Process VII: CCIM/ ISM ..... 14

2.9 Conclusion: Why CCIM is select as an adequate process for high value added applications ..... 16

**3 Cold crucible induction melting ..... 17**
3.1 A detailed description of CCIM ..... 17
3.1.1 Stages of CCIM ..... 18
3.1.2 Advantages/disadvantages ..... 20
3.1.3 Materials melt in CCIM ..... 21
3.1.4 CCIM applications ..... 21
3.1.5 Brief history of CCIM ..... 21
3.2 Parameters ..... 22
3.2.1 Superheat and efficiency ..... 22
3.2.2 Power (Current) ..... 23
3.2.3 Frequency ..... 25
3.2.4 Influence of the crucible filling level ..... 26
3.2.5 Crucible design ..... 27
3.2.6 Coil design ..... 30
3.2.7 Type of atmosphere and partial pressure of the gas ..... 30
3.2.8 Skull formation ..... 31
3.2.9 Improve of superheat using a DC magnetic field ..... 31
3.2.10 Power demand ..... 32
3.3 Investment casting of titanium ..... 32
3.3.1 Reactivity and alpha case ..... 34
3.3.2 Fluidity ..... 37
3.4 Casting processes ..... 38
3.5 Conclusions ..... 40

**4 Mathematical formulation of the problem ..... 41**
4.1 Approach to magnetohydrodynamics ..... 41
4.2 Governing equations: partial differential equations and boundary conditions ..... 42
4.2.1 Electromagnetic - Time and frequency domain ..... 42
4.2.2 Heat transfer - Time domain ..... 46
4.2.3 Navier-Stokes equations - Time domain ..... 47
4.3 Coupling conditions ..... 56
4.4 Conclusions ..... 57

**5 Numerical modelling ..... 59**
5.1 Numerical modelling (Literature Review) ..... 59
5.1.1 Numerical modelling of induction furnaces ..... 59
5.1.2 Numerical modelling of free surface ..... 61
5.1.3 Numerical modelling of CCIM ..... 61
5.2 Method and hypothesis ..... 62
5.3 Description of the discretization method for 2D numerical models ..... 64
5.3.1 2D hydrostatic steady state free surface model ..... 65
5.3.2 2D hydrodynamic free surface model ..... 66

5.4 Description of the discretization method for 3D numerical models ..... 67
5.5 Simulation advantages/limitations ..... 69
5.6 Conclusions ..... 69

**6 Numerical results ..... 71**
6.1 Validation of numerical models ..... 71
6.1.1 Meniscus shape ..... 71
6.1.2 Temperature ..... 74
6.1.3 Power efficiency ..... 75
6.2 2D simulations ..... 76
6.3 3D simulations ..... 78
6.3.1 Influence of the current in the meniscus shape and the superheat ..... 81
6.3.2 Influence of the frequency in the meniscus shape and the superheat for a given current ..... 83
6.3.3 Influence of the slit thickness in the efficiency ..... 84
6.4 Conclusions ..... 84

**7 Experimental results ..... 87**
7.1 CCIM facility ..... 87
7.2 CCIM facility's set-up ..... 90
7.3 Experiments ..... 91
7.4 Results ..... 94
7.5 Conclusions ..... 95

**8 Main accomplishments ..... 97**

**9 Conclusions and future research ..... 101**
9.1 Concluding remarks ..... 101
9.2 Future research ..... 103

**References ..... 105**

# LIST OF TABLES

Table 2-1. Comparison of different melting processes. ..... 6

Table 3-1. Effect of coil frequency on the maximum temperature under conditions of either fixed coil current $I$ or fixed electrical power $P_e$ for TiAl intermetallics (Bojarevics 2004). ..... 25

Table 5-1. Properties of Ti-6Al-4V ..... 63

Table 6-1. Comparison among experimental and modelling results ..... 76

Table 6-2. Power losses in each element of CCIM. ..... 84

# LIST OF FIGURES

Figure 2.1. Installation of VIM (Zanner 2004). ..... 7
Figure 2.2. Scheme of VAR installation (Lütjering 2007). ..... 9
Figure 2.3. Schematic diagram of EBM (Sakamoto 1992). ..... 12
Figure 2.4. A CCIM installation. ..... 15
Figure 2.5. a) Maxillofacial prosthesis and b) turbine blades. ..... 16
Figure 3.1. Scheme of a CCIM installation. ..... 18
Figure 3.2. Melting, the first step of the process (Umbrashko 2005). ..... 19
Figure 3.3. Free surfaces (○ experimental measurements and ─ numerical calculation) for different inductor effective currents $I_{ef}$: (a) $I_{ef}$ =1929 A, b) $I_{ef}$ =2956 A, and c) $I_{ef}$ =3566 A (Spitans 2013). ..... 23
Figure 3.4. Water and metal temperatures during CCIM of 3.6 kg of an Al alloy (Bojarevics 2004). ..... 24
Figure 3.5. Energy efficiency of CCIM furnace when melting Al and TiAl alloys (Bojarevics 2004). ..... 24
Figure 3.6. Influence of the frequency on the meniscus shape and superheat (Baake 2003a) ..... 26
Figure 3.7. Influence of the filling level in the superheat (Baake 2003a) ..... 26
Figure 3.8. Comparison of numerically simulated temperatures for various melt weights of TiAl and measured temperature data for 4 kg load (Bojarevics 2004). ..... 27
Figure 3.9. Influence of the H/D ratio in the superheat (Baake 2003a). ..... 28
Figure 3.10. a) Effect of the slit width on the resistance of the crucible respect $R_0$, which is evaluated under condition of neither charge nor crucible and b) effect of the slit width on the inductance of the crucible (Iwai 1995) ..... 28
Figure 3.11. Heat generation in the charge and the crucible in relation to slit width (Iwai 1995) ..... 29
Figure 3.12. Effect of the slit width on the ratio of heat generation in the charge, crucible, and coil with respect to the total heat (Iwai 1995). ..... 29
Figure 3.13. Al loss rate (at%/s) as a function of melting chamber pressure and melt temperature (Gomes 2013). ..... 31
Figure 3.14. Basic steps of investment casting (ASM 1988). ..... 33
Figure 3.15. Standard free energy of formation of oxides (Kuang 2001). ..... 36
Figure 3.16. Schematic effect of surface turbulence during mould filling (Harding 2006). ..... 38
Figure 3.17. a) Top gated gravity casting and b) bottom gated gravity casting (Harding 2004). ..... 39
Figure 4.1. Typical point velocity measurement in turbulent flow (Versteeg 2007). ..... 51
Figure 4.2. Coupling conditions. ..... 57

Figure 5.1.Turbulent viscosity distribution (Pa·s) in case of $k$-$\varepsilon$ (middle) and LES 3D modelling on mesh with $0.25 \cdot 10^6$ (left) and $3.5 \cdot 10^6$ (right) elements (Umbrashko 2006). ..... 60

Figure 5.2. Crucible of the CCIM installation at Mondragon Unibertsitatea. ..... 63

Figure 5.3. Algorithm for coupled electromagnetic and hydrodynamic free surface dynamic calculation. ..... 67

Figure 5.4. Model geometry. ..... 68

Figure 6.1. Induction furnace at the Institute of Electrotechnology of Hannover (Spitans 2013). ..... 72

Figure 6.2. Meniscus shape comparison among different models and experimental data. ..... 72

Figure 6.3. Lavers *et al*. experiments crucible geometry (Lavers 1988b). ..... 73

Figure 6.4. Meniscus shape. ..... 73

Figure 6.5. Sketch of the induction furnace with cold crucible (Baake 2007). ..... 74

Figure 6.6. a) Measured (Baake 2007) and b) simulated temperature (ºC) distribution. ..... 75

Figure 6.7. Sketch of cold crucible induction furnace (Ernst 2009). ..... 75

Figure 6.8. Free surfaces for different inductor effective currents $I_{ef}$ : 500, 2000, and 3000 A. ..... 76

Figure 6.9. Difference between magnetic and hydrostatic pressure along the free surface before and after deformation for a current of 3000 A. ..... 77

Figure 6.10. Free surface shapes at different time moments for a current $I$=2000 A and $f$=385 Hz. ..... 77

Figure 6.11. Vorticity in the melt (1/s) at $t$=0.255 s for a current $I$=4500 A and a frequency $f$=2 kHz for a crucible geometry of CCIM at MU. ..... 78

Figure 6.12. Magnetic flux lines. ..... 79

Figure 6.13. Normal component of the current density (A/m$^2$). ..... 79

Figure 6.14. a) Radial Lorentz forces (N/m$^3$) and b) axial Lorentz forces (N/m$^3$). ..... 80

Figure 6.15. Velocity vector (m/s). ..... 80

Figure 6.16. Temperature (ºC) in the melt after 20 seconds. ..... 81

Figure 6.17.Influence of the current in the meniscus shape and the temperature (ºC) for different inductor effective currents $I_{ef}$; $I_{ef}$ =500 A (left), $I_{ef}$ =2000 A (center), and $I_{ef}$ =3000 A (right). ..... 82

Figure 6.18. Influence of the current in the meniscus shape and the velocity (m/s) for different inductor effective currents $I_{ef}$; $I_{ef}$ =500 A (left), $I_{ef}$ =2000 A (center), and $I_{ef}$ =3000 A (right). ..... 82

Figure 6.19. Influence of the current in the meniscus shape and the temperature (ºC) at different frequencies; $f$ =1 kHz (left), $f$ =5 kHz (center), and $f$ =9 kHz (right). ..... 83

Figure 6.20. Influence of the frequency in the meniscus shape and the velocity (m/s) for different frequencies; $f$ =1 kHz (left), $f$ =5 kHz (center), and $f$ =9 kHz (right). ..... 84

Figure 7.1. CCIM installation. ..... 87

Figure 7.2. CCIM sketch. ..... 88

Figure 7.3. Crucible. ..... 89

Figure 7.4. Rotary piston pump H149 (left) and mechanical booster MB43 pump (right). ..... 90

Figure 7.5. Turbine blade. ..... 91

Figure 7.6. a) Wax turbine blade and b) mould design. ..... 92

Figure 7.7. Ceramic mould. ..... 92

Figure 7.8. Melting of titanium. ..... 93

Figure 7.9. Titanium pucks. ..... 94

Figure 7.10. Fabricated parts. ..... 94

# GLOSSARY

## Roman symbols

| | |
|---|---|
| **B** | magnetic flux density field |
| **E** | electric field intensity |
| **D** | electric displacement |
| **H** | magnetic field intensity |
| **J** | electric current density |
| $j$ | imaginary unit |
| $B_0$ | magnetic flux density field amplitude |
| $B_{eff}$ | the magnetic field strength (r.m.s. value) |
| **u** | fluid velocity |
| $\mathbf{J_e}$ | external current density |
| $f$ | frequency |
| **g** | gravitational acceleration |
| **P** | electric polarization vector |
| **M** | magnetization vector |
| **A** | magnetic vector potential |
| $I$ | inductor current |

| | |
|---|---|
| $p$ | pressure |
| $\mathbf{F}$ | electromagnetic forces |
| $U$ | mean value velocity |
| $Q$ | heat |
| $\mathbf{q}$ | heat flux vector |
| $\mathbf{n}$ | direction of the normal vector |
| $T$ | temperature |
| $T_{amb}$ | ambient temperature |
| $u_{x,}\, u_{y,}\, u_z$ | fluid velocity in $x$, $y$, and $z$ directions |
| $U_x$, $U_y$, $U_z$ | mean value velocity in $x$, $y$, and $z$ directions |
| $u_x'$, $u_y'$, $u_z'$ | fluid velocity fluctuations in $x$, $y$, and $z$ directions |
| $P$ | mean pressure |
| $p'$ | pressure fluctuation |
| $F_{x,}\, F_{y,}\, F_z$ | external forces in $x$, $y$, and $z$ directions |
| $\mathbf{S}$ | strain-rate tensor |
| $k_t$ | thermal conductivity |
| $k_T$ | turbulent thermal conductivity |
| $t$ | time |
| $C_p$ | specific heat capacity |
| $Pr_T$ | turbulent Prandtl number |
| $R_e$ | Reynolds number |
| $R_m$ | Reynolds magnetic number |
| $H$ | crucible height |
| $D$ | crucible diameter |

| | |
|---|---|
| $L$ | characteristic length |
| $U_e$ | internal energy |
| $h_m$ | height of the dome |
| $e$ | emissivity |
| $U_A$ | Alfvén velocity |
| $k$ | turbulent kinetic energy |
| $P_k$ | production term |
| $k_v$ | von Kárman constant |
| $f_0$ | normal stress of the boundary |
| $U_{ref,} I_{T,} L_T$ | model constants of $k$-$\omega$ turbulence model |
| $\mathbf{u}_{\mathbf{tang}}$ | fluid velocity in tangential direction |
| $P_{HS}$ | hydrostatic pressure |
| $P_{ST}$ | surface tension pressure |
| $P_{EM}$ | magnetic pressure |
| $P_{HD}$ | hydrodynamic |
| $n_x$, $n_y$ | normal vector components in $x$ and $y$ direction |
| $P_a$ | surrounding pressure ($P_a$=0) |
| $\Delta g^0_f$ | Gibbs free energy of formation |
| $P_e$ | electrical power |

## Greek symbols

| | |
|---|---|
| $\varepsilon_0$ | permittivity of vacuum |
| $\varepsilon_r$ | relative permittivity |
| $\varepsilon$ | dissipation rate |
| $\omega$ | specific dissipation rate |

| | |
|---|---|
| $\sigma$ | electrical conductivity |
| $\sigma_B$ | Stefan-Boltzmann constant |
| $\gamma$ | surface tension |
| $\delta$ | skin depth |
| $\mu_0$ | permeability of vacuum |
| $\mu_r$ | relative permeability |
| $\omega_f$ | angular frequency |
| $\tau$ | viscous stress tensor |
| $\rho$ | density |
| $\Gamma$ | curvature of the free surface |
| $\mu$ | dynamic viscosity |
| $\mu_T$ | dynamic turbulent viscosity |
| $\mu_{eff}$ | effective viscosity ($\mu_{eff} = \mu + \mu_T$) |
| $\rho_e$ | electric charge density |
| $\rho_s$ | surface charge density |
| $\alpha, \beta_{0,} \beta_0^*, \sigma^*, \sigma_1^*$ | model constants of $k$-$\omega$ turbulence model |
| $\delta_w^+$ | distance from the wall to the computational domain |

## Operators

| | |
|---|---|
| $\Delta$ | variation |
| $\nabla$ | Nabla operator |

## Abbreviations

| | |
|---|---|
| VIM | Vacuum induction melting |
| VAR | Vacuum arc remelting |
| EBM | Electron beam melting |

| | |
|---|---|
| PAM | Plasma arc melting |
| CCIM | Cold crucible induction melting |
| ESR | Electroslag remelting |
| ISM | Induction skull melting |
| MHD | Magnetohydrodynamics |
| HIP | Hot isostatic pressing |
| FEM | Finite element method |
| FVM | Finite element method |
| VOF | Volume of fluid method |
| RANS | Reynolds averaged Navier-Stokes |
| LES | Large eddy simulation |
| DNS | Direct current |
| RNG | Renormalization group |
| PDE | partial differential equations |
| ALE | Arbitrary Lagrangian-Eulerian |
| AC | Alternating current |
| DC | Direct current |
| 2D | Two dimensional |
| 3D | Three dimensional |

# CHAPTER 1
# INTRODUCTION

In this first chapter we present the framework of the dissertation and the motivation to carry out this research. Then, we detail the research objectives. At last, we explain the working methodology followed to accomplish the objectives and we summarize the main chapters of the dissertation.

## 1.1 Motivation and background

This dissertation concerns the development of a numerical modelling of cold crucible induction melting (CCIM) process. This numerical models lead to a better understanding of the parameters of the process and will help for the production of high value added components of titanium and its alloys. The main part of the dissertation focuses on the development of a numerical modelling of CCIM to optimize the main parameters of the process. The second part deals with the set-up of an installation of CCIM and the production of high value added components of titanium and its alloys.

In the last years, titanium and its alloys are getting much attention because of their excellent biocompatibility, light weight, excellent balance of mechanical properties, and excellent corrosion resistance (Niinomi 2008, Niinomi 2003a, Niinomi 2003b, Kudrman 2007, Bi 1997, Da Rocha 2005, Jovanovic 2006, Mohammadi 2001). These great characteristics make titanium and its alloys very interesting for numerous applications such as medical prostheses (Wetzel 2008) and aerospace industry (Harding 2003, Tetsui 2011). However, the relatively high costs during the fabrication of these components have restricted their applications (Nastac 2006). If the aim is to manufacture cheap components, a casting route is often the most cost effective means of producing engineering components (Harding 2006, Yongliang 2008, Gomes 2011, Nelson 1992, Larsen 1996). However, it is difficult to cast titanium by conventional casting techniques because of its reactivity at high temperatures, which reacts with the crucible and mould components. Among different casting processes (VIM, VAR, ESR, EBM, ESR), the cold crucible induction melting (CCIM) process is currently the most effective way to melt these alloys for the fabrication of high value added components (Reed 2003, Bojarevics 2003, Dlouhy 2003).

The CCIM process uses a segmented water cooled cooper crucible to avoid contamination of reactive alloys. The cooper wall is made of electrically insulated segment. Thus, the magnetic field supplied by the induction coil passes through the crucible segments. This magnetic field generates induced currents that heat and melt the metal charge. The drawbacks of this process are the poor efficiency due to great percentage of heat that is removed by the cooling system and the small superheat of the melt, which can cause solidification problems.

In this dissertation, we have selected the CCIM process to melt and cast titanium alloys. In order to overcome the drawbacks of the process, we have developed a numerical model. Practical experiments show that the superheat of the entire melt, which is determined by the electromagnetic, hydrodynamic, and thermal processes factors, is one of the key parameters of this technological process. The task of optimizing melt superheat faces the challenge of finding optimal combination of crucible height to diameter ratio, coil design, crucible design, current strength, and frequency. Variation of any of the aforementioned factors influences the shape of melt meniscus and, as a result, flow pattern and energy balance.

Besides performing numerical calculations for the optimization of the process, we have also set up an installation of CCIM and we have cast different titanium parts.

## 1.2 Objectives

The main objective of this dissertation is the development of a numerical model of a of cold crucible induction melting (CCIM) that helps for the production of high value added components of titanium and its alloys. For such purpose, the following specific objectives have been identified:

- Analysis of different methodologies to simulate CCIM.
- Development of a simulation methodology capable of representing a CCIM process in an accurate way.
- Calculations of the free surface of melt.
- Electromagnetic analysis of induction system including estimation of power losses, distribution of eddy currents, heat sources, and Lorentz forces.
- Study of transient 3D hydrodynamics problems.
- Model verification comparing results to available experimental data or to other computational results.
- Set-up and optimization of a CCIM installation.

- Evaluation of the influence of the main parameters of CCIM.
- Identification of parts to manufacture.
- Selection of mould material.
- Design of filling and rising system of the mould.
- Fabrication of titanium parts.

## 1.3 Outline of the present dissertation

This dissertation covers both theoretical and experimental work. The research exposed in this dissertation is divided into nine chapters. The first one is this introduction.

Chapter 2 describes the state of the art of existing casting processes of titanium and titanium alloys. Different technologies to melt and cast titanium are briefly presented and we explain why the cold crucible induction melting (CCIM) process has been the choice for the fabrication of high value added components.

Chapter 3 deals with the literature review of CCIM. We study in detail the influence of the parameters of CCIM in the superheat of the melt and in the efficiency of the process. In addition, we present a brief review of investment casting of titanium and titanium alloys, which is the traditional route to cast titanium parts in combination with CCIM. Finally, we report some methods to tilt the molten metal form the crucible to the moulds.

In chapter 4, the theoretical background of the studied physical phenomena is presented. It contains a basic description of the main physical principles of magnetohydrodynamics, which covers electromagnetism, fluid dynamic, and temperature. After describing a general approach to magnetohydrodynamic problems, we explain the governing equations and boundary conditions of electromagnetic, heat transfer, and fluid mechanics fields and we depict the coupling conditions.

Chapter 5 describes the numerical modelling method used to simulate the CCIM problem. First, we give a literature review of numerical methods used for modelling CCIM and we introduce the one used in our simulations. Then, we explain the hypothesis applied to the numerical modelling and we describe both two and three dimensional models. Finally, we detail the advantages and limitations of our simulation methodology.

In Chapter 6, we first validate our numerical models comparing the numerical results with experimental results carried out by other authors. Then, we present additional numerical results in 2D and 3D.

In Chapter 7 we present the cold crucible induction melting furnace at Mondragon Unibertsitatea (MU). We state the characteristics of the facility and the problems that we have overcome during the setting-up of the installation, which is capable of melting 1 kg of Ti-6Al-4V. We also explain the experiments that we have performed to obtain high value added components.

Chapter 8 contains the main accomplishments of this dissertation.

Chapter 9 describes the conclusions of this dissertation and the future work.

CHAPTER 2

# CASTING PROCESSES OF TITANIUM

This chapter is an introduction to the state of the art of existing casting processes of titanium and titanium alloys. Different technologies to melt and cast titanium are briefly presented and an explanation of why the cold crucible induction melting (CCIM) process has been the choice for the fabrication of high value added components is given.

## 2.1 Introduction

Titanium and its alloys have emerged as a very attractive metal for numerous applications: medical prostheses, aerospace industry, automotive industry, power generation, sport equipment, and marine engineering. The reason lie in their attractive properties, such as excellent biocompatibility, high specific strength, excellent corrosion resistance, excellent high temperature creep resistance and good fracture toughness (Niinomi 2008, Kudrman 2007, Niinomi 2007). However, the application of titanium is often limited by its relatively high cost (Nastac 2006, Keller 1997).

This high cost of titanium makes net shape manufacturing a very attractive route. If the aim is to achieve cheap products, casting is a near net shape manufacturing route that offers significant cost advantages over forgings or fabricated structures (Yongliang 2008, Gomes 2011, Nelson 1992, Larsen 1996, Bermingham 2007). However, the wide use of titanium alloys casting has been limited because of its reactivity in molten states, poor fluidity, the alpha-case formation, and the casting defects (Reed 2004).

Currently, in the industry, there are a great variety of processes to melt titanium and titanium alloys. The principal melting processes of titanium are listed in table 2-1. Each processes or technology has its advantages and disadvantages. Generally, the selection of melting process of titanium must be done considering alloys composition, the size and shape of the required product, the production operation cost, and the quality requirements.

Table 2-1. Comparison of different melting processes.

| Melting method | | Pressure | Efficiency | Composition change | Applications |
|---|---|---|---|---|---|
| Refractory crucible melting | Vacuum induction melting (VIM) | Vacuum/ inert gas | Middle | Low | Ingots<br>Final parts<br>Electrodes |
| Cold crucible melting | Vacuum arc remelting (VAR) | Vacuum | Low | Low | Ingots<br>Final parts |
| | Electron beam melting (EBM) | High vacuum | Low | High | Ingots<br>Final parts |
| | Plasma arc melting (PAM) | Inert gas | Middle | Low | Ingots<br>Final parts |
| | Cold crucible induction melting (CCIM) | Inert gas | Middle | Low | Final parts |
| | Electroslag remelting (ESR) | Air | Low | Low | Ingots |

The majority of casting processes reported in Table 2-1 are based on vacuum melting and were developed 50 years ago. During the World War II, the designers and metallurgists started using refractory metals (alloys of Ti, Nb, Mo, and W) and nickel base superalloys to produce products (such as gas turbine engines and nuclear reactors) that required a combination of high temperature, stress, and oxidative operational environments. These materials in liquid state are very reactive with oxygen, nitrogen, carbon, and in many cases with hydrogen. Furthermore, during solidification, the reaction products precipitate as ceramic and/or intermetallic particles which act as nucleation sites for fatigue cracks. In order to solve these drawbacks, these products started to be made in vacuum because early work showed that melting these materials in a vacuum or controlled atmosphere produced an improvement in fracture toughness and resistance to fatigue. Up until the late 1940s vacuum melting processes were vacuum induction melting (VIM), vacuum arc remelting (VAR), and electron beam melting (EBM). There were laboratory scale units used to produce small research quantities of materials (Zanner 2004).

During the 1950s and 1960s the commercial demand for these vacuum melted materials increased. This tremendous growth generated great innovations in furnace design, operation, and process control to create the mature vacuum melting industry of today. Thanks to vacuum melt processing, it is possible the existence of many of the advanced alloy systems that are used today in the aerospace, automotive, and energy industries.

In the past few years, several new melting techniques have been industrialized for the production of superalloys, titanium alloys, and steels. These techniques include plasma arc melting (PAM), triple melt (VIM + ESR + VAR), and cold crucible induction melting (CCIM).

## 2.2 Process I: VIM

Vacuum induction melting (VIM) process is the melting of metals by induction performed under vacuum or controlled atmosphere. In VIM, the charge (the metal) is located inside a ceramic crucible. A coil that

surrounds the crucible generates induced currents in the charge by electromagnetic induction that are responsible of heating and melting the charge.

The first large commercial furnaces of VIM were installed in Germany in 1923 (Zanner 2004). However, it was not until 1950s when the process first became important since it was found that heat resisting alloys or superalloys (which contain large amounts of reactive elements such as aluminum or titanium) had superior service life and reliability when were melted in vacuum. Jet engine produced by VIM offered great advance in performance and durability, which has been so important to both military and commercial aviation. The success in the production of superalloys by VIM for the gas turbine industry stimulated interest of VIM for the manufacture of critical products used in other sector as nuclear reactors and electronics (CMP 1987).

VIM furnaces utilize a ceramic crucible to place the metal. Heating is accomplished with an AC magnetic field generated by a water cooled coil surrounding the crucible. As the ceramic crucible is transparent for the magnetic field, eddy currents within the metal are generated, creating internal resistance heating. The depth of penetration of the eddy currents is inversely proportional to the coil frequency. Greater stirring of the molten metal is achieved at larger penetration depths. Thus, the frequency of the power supply must be tuned to the furnace geometry. In addition, the coil must also be carefully insulated to prevent voltage breakdown between coil turns in the vacuum ambient.

The basic equipment of VIM is composed by melt chamber, mould chamber, pumping system, power supply, and a control station (Figure 2.1). In some furnaces, the melt chamber and mould chamber are separated. When are separated, they are also separately pumped to enable the furnace to operate in a semicontinuos mode. This improves efficiency because it allows a melt to be started while the mould chamber is being prepared at the beginning of a cycle. The mould chamber contains the ingot moulds, independent instrumentation, and sometimes primary and secondary tundishes. The control station contains all valve actuators, sensor instruments, and recorders for control of the process. Melt observation is conducted directly through shielded sights or by video cameras and recorders. Both the crucible and coil are located inside a melt chamber.

Figure 2.1. Installation of VIM (Zanner 2004).

The products obtained from VIM are usually long cylindrical ingots cast in iron or steel moulds. These ingots range in diameter from 0.1 m to 1 m. Since ingots are usually very long (>2 m) compared to the diameter, solidification is almost horizontal from the mould wall into the center. This condition results in entrapped solidification shrinkage or pipe cavity, and for this reason, these ingots are primarily used as electrodes for subsequent vacuum arc remelting (VAR) or electroslag remelting (ESR) processes (Zanner 2004). The casting weight vary from 1 kg to 30 tons or even more, depending on whether the furnace is being used for precision casting or for the production of ingots or electrodes for further processing (Ald 2012). Besides titanium and titanium alloys, VIM is used to melt and cast superalloys based nickel and cobalt and high-strength steels which require vacuum processing because they contain refractory and reactive elements such as Nb, Ti, and Al. VIM is also used to melt special copper base, uranium, and other unique materials (CMP 1987).

### Advantages/disadvantages

The specific advantages of vacuum induction melting include (CMP 1987, Si-Young 2007):

- **Elimination of gases:** under very low pressures ($10^{-3}$ mbar) undesirable gases and potentially harmful volatile elements are eliminated from the charged raw materials during the melting.

- **Close control of chemical analysis:** exceptional and reproducible control of reactive element containing compositions is possible because of the lack of atmosphere. Thus, it is possible to achieve a very close compositional tolerance (an excellent chemistry precision). Furthermore, the charge material chemistry is the same one as that desired for the casting.

- **Slag free melting:** melting in vacuum eliminates the need for a protective slag cover and decreases the potential of accidental slag contamination or inclusions in the ingot.

- **Melt protection:** vacuum prevents deleterious contaminating reactions with atmospheric gases.

- **Controlled superheating:** possibility of control the superheat.

The shortfalls include the fact that the melting and processing take place in a ceramic crucible and the difficulty in feeding solidification shrinkage (CMP 1987). The use of an oxide refractory introduces exogenous oxide particles into the alloy. Several approaches have been developed over the years to mitigate such as add a tundishes system with porous ceramic filters. However, there are not methods to eliminate these inclusions completely.

As there is no practical alternative to VIM process for obtaining close chemical control and homogeneity required by specification (Mitchell 1992), the industrial solution has been to assume that the metal produced by VIM contains inclusions and further refinement is necessary in order to remove them by remelting processes (Mitchell 1994).

## 2.3 Process II: VAR

Vacuum arc remelting (VAR) is the oldest remelting processes. VAR is a continuous remelting of a consumable electrode by means of an arc under vacuum. Two can be the origin of these electrodes: a) ingots produced by ESR, VIM, and EBM are utilized as electrodes in the VAR process in order to improve their purity and refine their structure (Zanner 2004); b) mechanically compacted blocks of sponge and alloying elements are also used as melt electrode. In this case, the sponge and alloying elements are blended together in a twin cone blender. This mixture is then placed in a die and mechanically compacted at room temperature into blocks using a hydraulic press. The as-compacted blocks have adequate "green strength" to remain intact during handling and melting. These blocks are welded together in an inert gas welding chamber to create the first melt electrode (Lütjering 2007).

The electrode is suspended from a water cooled copper ram into a long cylindrical water cooled cooper crucible. The entire assembly containing the electrode and crucible is evacuated and the electrode and crucible are connected to the negative and positive bus bars, respectively, of a large DC power supply. Melting starts after an arc is started between the electrode and the base plate of the copper mould. The intense heat generated by the electric arc melts the tip of the electrode. Molten metal drops drips from the electrode into a molten pool contained by the crucible and a new ingot is progressively formed in the water cooled mould (Figure 2.2).

VAR process is mostly used to fabricate ingots. Ingots produced by VAR range in size from 0.05 m to 1 m in diameter and weigh from 1 kg to 15000 kg (Lütjering 2007).

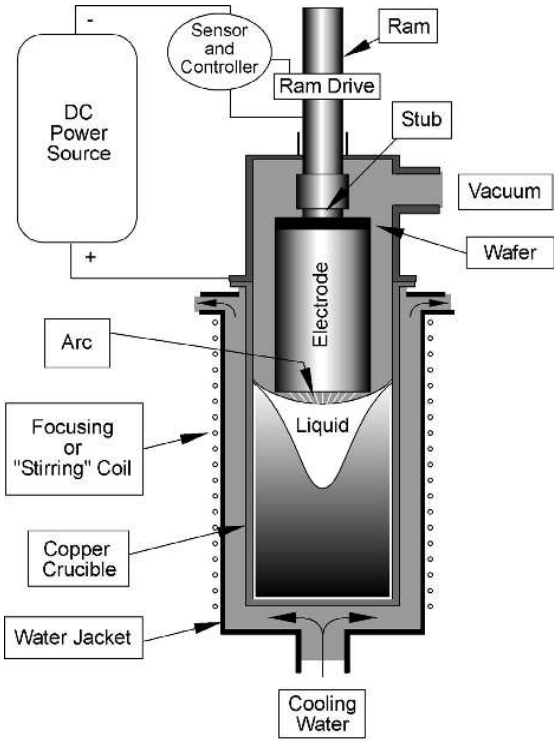


Figure 2.2. Scheme of VAR installation (Lütjering 2007).

Initially developed in the 1950s as a process for the production of titanium alloy ingots, it was rapidly picked up by superalloys producers in order to make ingots of forging grades of alloys (Mitchell 1994). The process requires a homogeneous electrode of a diameter slightly smaller than the final ingot. The VAR process does not change the basic alloy composition and no additions can be incorporated during the operation. The original intent of the process was to remove any residual inclusion content in the VIM electrode. However, with the development of the VIM process for producing cleaner electrodes, the role of VAR has become less to remove inclusions and more of solidification control.

The arc is the most important parameter of the VAR process. It provides the electrical conduction path that couples the electrode and molten pool and provides the heat for melting. The arc is sustained by ionized metal vapors evolved by evaporation from the electrode (cathode) and molten pool (anode). Ingot quality is controlled by how uniformly the arc injects current into the molten pool. Melt rate and the electrode gap are manipulated to control the arc and provide a steady heat source. Arc behavior is optimized when the arc behaves as a macro-uniform heat source (Zanner 2004).

Solidification starts at the crucible wall and proceeds inward with upward curvature so that the columnar dendrites are almost vertical at the ingot centerline. Furthermore, the ingot solidification pattern is essentially directional (Mitchell 1994). When the thermal gradient in the center region is low (caused by a high melt rate creating a deep pool), equiaxed grains will be found in the center region of the ingot. There is a general consensus in the industry that ingots with complete columnar structure yield the highest-quality material. Since molten metal is dropped continuously form the electrode to the pool, the solidification is upwards. Thus, the solidification shrinkage is constantly being fed, resulting in a solid ingot (Zanner 2004).

### Advantages/disadvantages

The specific advantages of VAR are the following (Si-Young 2007):

- **Improvement of cleanliness by removal of oxides:** Oxide removal is achieved by chemical and physical processes.
- Solidification control.
- Decrease of undesirable trace elements of high vapor pressures content.
- Remove of dissolved gasses, such as hydrogen and nitrogen.
- **Directional solidification:** Achievement of directional solidification of the ingot from bottom to top in order to avoid macro-segregation and minimize micro-segregation.
- Absence of ceramics.

The drawbacks are (Si-Young 2007):

- The necessity to employ prealloyed electrodes in order to produce castings makes it extremely difficult and expensive to produce nonstandard grades of titanium.
- Castings must undergo HIP treatment to minimize the internal porosities.
- Application of VAR process is not suitable for the fabrication of thin wall and complex parts. Only for the fabrication of ingots and simply large parts.
- Sensitivity of solidification structure to the arc.

However, in spite of the merit of directional solidification, various defects such as freckles, white spots, and porosities can occur in a remelted ingot. In order to avoid these ingot defects, it is necessary to control the correlated operating parameters such as use of homogeneous electrode, remelting rate, liquid pool depth, and arc column.

## 2.4 Process III: ESR

An alternative remelting process to VAR that has been widely used for several years is the electroslag remelting process (ESR). Invented in the United States, it was extensively developed in the USSR in the 1960s and became of general use in that decade. However, nowadays, it is not extensively used. The reasons are probably more connected with the cost of changing specifications historically written for VAR than with the intrinsic quality issues of ESR, because a number of studies have shown that a properly conducted ESR process is capable of producing superalloys that are at least as free from defects as those produced by VAR ingots (Mitchell 1994).

The equipment is similar to VAR. However, the melting is performed using a slag rather than under a vacuum. Whereas VAR needs vacuum for refining, in ESR the consumable electrode is dipped into a pool of slag in a water cooled mould. An electric current (usually AC) passes through the slag, between the electrode and the ingot being formed and superheats the slag so that drops of metal are melted from the electrode. These drops travel through the slag to the bottom of the water cooled mould, where they solidify. As the developing droplets pass through the slag, the metal is cleaned of non-metallic impurities, which are removed by chemical reaction with the slag or by physical flotation to the top of the molten pool.

The slag pool is carried upwards as the ingot forms. The new ingot of refined material builds up slowly from the bottom of the mould. It is homogeneous, directionally solidified, and free from the central unsoundness that can occur in conventionally cast ingots as they solidify from the outside inwards (Ald 2012).

The primary purpose of the ESR is to form an ingot which will constitute the most stable electrode for VAR. The principal differences between ESR and VAR lie in the more complex ESR chemical system and in the slightly different thermal regimes (Mitchell 1992).

### Advantages/disadvantages

The ESR process has two significant technical advantages over VAR; first, it is less sensitive to electrode quality; second, it removes more inclusions than VAR (Mitchell 1994).

Probably, its mayor disadvantage lies in the differences in heat transfer regime between the two processes, which results in ESR ingots having a longer solidification time at the ingot center when operating at the limit of the permissible range on ingot diameters. As a result, there is a tendency for ESR ingots to have a coarser ingot center structure than VAR ingots (Mitchell 1994). As in VAR, various defects such as freckles can occur in ingots remelted by ESR. Reasons for the occurrence of these defects are the same as in VAR. It is important to note that white spots normally do not occur in ESR ingots.

## 2.5 Process IV: Triple melt

An attempt has been made recently to combine the merits of the two remelting process noted above in a process called triple melt. In this process, the electrode is created by VIM, remelted by ESR, and then remelted again by VAR. The objective is to take the advantage of chemical refining offered by ESR and the microstructure control in the final ingot with VAR process (Mitchell 1994).

## 2.6 Process V: EBM

Electron beam melting (EBM) is a process where the charge located inside a cooper water cooled hearth (or crucible) is melted by electron beam gun (Figure 2.3). Subsequently, the molten metal passes through one or several refining hearth before flowing into a mould in order to form an ingot or a slab.

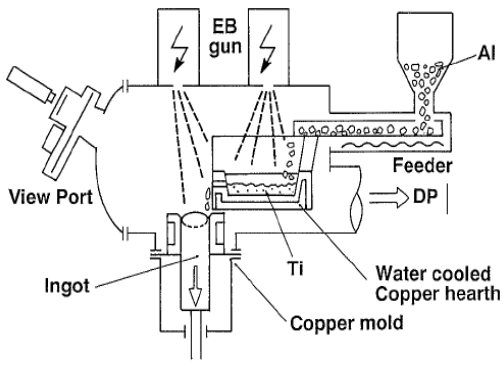


Figure 2.3. Schematic diagram of EBM (Sakamoto 1992).

In EBM, the heat input from the electron beam is balanced against the rate of heat extraction from the water cooled cooper hearth. This maintains a thin layer of solid titanium alloy in contact with the crucible. Electron guns must operate at voltage, power, and pressure levels below the conditions for high voltage breakdown or arc down.

Up to the 1960s, EBM was primarily used to consolidate Ta, Nb, Mo, and W by drip melting into water cooled cooper crucibles. In some instances, the resulting ingots were subsequently vacuum arc remelted. These materials were electron beam melted because they are embrittled by O, N, and in some cases H, and they have very high melting points. Refractory metals were the first candidates for EBM, because the furnace chamber operating pressures were quite low, approx. 0.133 Pa, and the ambient furnace conditions could be tolerated by the available electron gun technology (Zanner 2004). Until recently, although electron beam heating was an accepted industrial technique, in melting applications it had the well-deserved reputation of unreliable and complex (Mitchell 1994).

Electron beam guns represent high temperature heat sources capable of exceeding the melting and even evaporation temperatures of all materials. By magnetic deflection and rapid scanning at high frequencies, the electron beam can be effectively directed at targets of multiple shapes and is thus the most flexible heat source in remelting technology.

The commercial furnaces of electron beam melting to melt titanium and titanium alloys are not fit for melting TiAl because the evaporation loss in this kind of titanium alloys is evident (Su 2005).

Among the feature of EBM (Si-Young 2007), it is possible to remark: a) The flexibility and controllability of the process temperature, speed, and reactions; b) The use of a wide variety of feedstock materials on terms of materials quality, size, and shape.

### Advantages/disadvantages

The main advantages of this processing include a) the removal of high-density inclusions of WC by sinking to the bottom of the hearth, decomposition, and/or capture of hard α-particles (TiN) because of the long time in the liquid, b) the ability to recycle Ti scrap (Zanner 2004), and c) the improvement in ingot quality, since melting is conducted under higher vacuum and for a longer time, thus, enabling more complete degassing and dissolution of low density inclusions (Semiatin 2004).

One of the biggest, yet unexploited, advantages of electron beam melting is the potential to precisely control solidification. Since the electron beam can be accurately focused and deflected much faster than the thermal diffusion speed in the ingot, it should be possible to control, in space and time, the thermal environment in the solidification region. Online coupling of this control capability with numerical simulation could provide the potential to use EBM as the final melt process and the potential to process superalloys that are subject to severe macrosegration (Zanner 2004).

However, EBM melting process use the water cooled copper crucibles, thus an EBM process cannot solve the HIP treatment problem due to porosity (Si-Young 2007). Furthermore, it is difficult to adjust

chemistry of alloys because some alloying elements with higher vapor pressure (Al, Sn, and Cr) easily vaporize under vacuum range required for working for EBM (Semiatin 2004, Suzuki 2003). In addition, it is also difficult to control chemical composition of alloying elements in the specified range because the control of the melt rate has not been quantitatively characterized.

## 2.7 Process VI: PAM

Plasma arc melting (PAM) is a technique in which a thermal plasma is used to melt the feed material. Plasma arc melting furnaces are usually operated under slightly positive pressure to prevent the potential atmospheric contamination by oxygen and nitrogen. Plasma torches are normally operated with argon plasma gas. The operating pressure is around 1 Pa (ASM 1988). Also, the high pressure is an essential requirement for preventing the selective evaporation of alloying elements that are characterized by high activity coefficient or vapor pressures such as Al, Cr, and Mg in titanium alloys.

Plasma technique has been employed as a melting process frequently over the years, but with the exception of some titanium applications, the method has not been widely accepted. The reasons for this are a complex mixture of commercial and technical factors. Although the process appears rather simple, in practice the equipment and operation are comparably complex (Mitchell 1994).

### Advantages/disadvantages

Plasma arc melting is characterized by the following distinct advantages (Jha 2008):

- PAM can be used at atmospheric pressure, resulting in extremely low alloy losses.
- PAM can handle charge of different type and densities.
- Refractory contamination is avoided through skull.

The disadvantages of PAM are the impossibility to control the superheat (increased power results in increased melting rates instead of superheat) and the use of an expensive electrode. Furthermore, the PAM process uses the water cooled cooper crucibles. Hence, the PAM process is not free from porosity and low fluidity problems in titanium casting.

## 2.8 Process VII: CCIM/ ISM

The cold crucible induction melting (CCIM) has been established for many years as being a clean and rapid technique for melting reactive alloys. Instead of the typical ceramic crucibles used in VIM, the alloys are commonly induction melted in a water cooled cooper crucible to prevent the contamination.

The crucible wall is segmented so that the magnetic field generated by the coil surrounding the crucible penetrates through the slits. This magnetic field generates induced currents to melt the charge by Joule effect. Furthermore, the Lorentz forces generated in the charge due to the variable magnetic field push the melt away from the water cooled crucible wall to minimise heat loss. The first metal to melt immediately re-solidifies on the inside of the cooper container and acts as a protective layer for the remainder of the melt. This skull is located at all contact areas of crucible and melt, at the bottom as well as at the wall. After pouring the molten metal into a mould, a thin skin of metal remains in the crucible and is called a "skull", and hence, the process is often called induction skull melting (ISM).

The basic components of a CCIM machine are a chamber, a power supply, a water cooled cooper crucible, a coil, and a mould (Figure 2.4). In order to prevent the reaction of titanium with oxygen and nitrogen, melting, casting, and cooling are performed in vacuum or in inert atmosphere. At present, the maximum capacity of these furnaces is approx. 100 kg of Ti (Harding 2011).

Figure 2.4. A CCIM installation.

### Advantages/disadvantages

The process offers several advantages:

- The melt stock can be basically anything that physically fits into the crucible.
- Capable of melting nearly any alloy.
- CCIM offers homogeneity of alloys due its inherent molten metal stirring caused by the magnetic field of the induction coil.
- Since the charge is melted by the applied magnetic field, there is no need for electrode fabrication.

- Copper crucible avoids any contamination of the charge material.

Disadvantages include the requirement of a much larger power supply than VIM, low melt weight, a limited melt superheat, skull removal every time the melt chemistry is changed, and a very poor efficiency.

## 2.9 Conclusion: Why CCIM is select as an adequate process for high value added applications

In this chapter, we have briefly described different existing processes for melting and casting titanium. More detailed information of each process can be found elsewhere (Mitchell 1992, Lütjering 2007, Sakamoto 1992, ASM 1988, Mitchell 2009, Birben 2007).

Our aim is to select a suitable melting process for the fabrication of high value added components of titanium and its alloys such as maxillofacial prostheses and turbine blades (Figure 2.5). In this dissertation, one of the parts selected to fabricate in titanium has been a turbine blade.

a) b)

Figure 2.5. a) Maxillofacial prosthesis and b) turbine blades.

As has been previously stated, the melting process of titanium must be selected with consideration for alloys composition, shape, size, economics, and working factors.

Mostly, high value added components require a good chemical composition and zero inclusion. As has been reported, the currently available methods for melting titanium mainly include VAR, VIM, ESR, EBM, PAM, and CCIM.

VIM process cannot support products without inclusion. Hence, it is not a proper choice. Among the remaining methods, VAR, ESR, and PAM requires very high quality electrodes and raw materials, and needs additional alloy melting and casting to prepare the electrodes, which frequently have many shrinkage holes and impurities that adversely affect the quality of final products. Because EBM is conducted under a high vacuum, there is an evaporation of high vapour pressure elements that can lead to noticeable changes in composition, decreasing the mechanical properties of the components.

Thus we have selected CCIM as the most suitable melting process for our application.

CHAPTER 3

# COLD CRUCIBLE INDUCTION MELTING

In this chapter, the main features of cold crucible induction melting process are described. Moreover, the influence of the parameters of CCIM in the superheat of the melt and in the efficiency of the process is studied in detail. In addition, a brief review of investment casting of titanium and titanium alloys, which is the traditional route to cast titanium parts in combination with CCIM, is also presented. Finally, some methods to tilt the molten metal form the crucible to the mould are reported.

## 3.1 A detailed description of CCIM

The cold crucible induction melting (CCIM) is one of the few processes suitable for melting reactive metal alloys as titanium and tantalum. Its principal feature is the use of a water cooled cooper crucible to prevent the contamination of the metal. As the crucible is segmented, the magnetic field generated by the coil surrounding the crucible can penetrate through the slits of the crucible and melt the charge by Joule effect. Furthermore, both melting and casting are performed under vacuum or controlled atmosphere to ensure the lack of contamination of titanium with nitrogen and oxygen.

Once the charge is melted, the metal is held away from the wall due to the Lorentz forces. Thus, the heat loss by conduction from the copper crucible is minimized. Moreover, because of these electromagnetic forces, the molten metal exhibits a meniscus shape.

When the metal starts to melt, the first part immediately re-solidifies inside the copper crucible, since the melt is in contact with the crucible and acts as a protective layer for the remainder of the melt. This layer is commonly called “skull”. Characteristics of the skull such as the height and width depend on CCIM parameters as the power. After pouring the molten metal into a mould, this skull remains in the crucible. Because of the presence of the skull, the process is often called induction skull melting (ISM).

The basic components of a CCIM machine are the chamber, a power supply, a water cooled cooper crucible, a coil, a mould, a cooling circuit, and a pumping system (Figure 3.1). Generally, the crucible and the mould are located in the same chamber. In order to prevent the reaction of titanium with oxygen and nitrogen, melting, casting, and solidification are performed under vacuum or inert atmosphere. Typical melt weights are between 5 and 100 kg (Harding 2011).

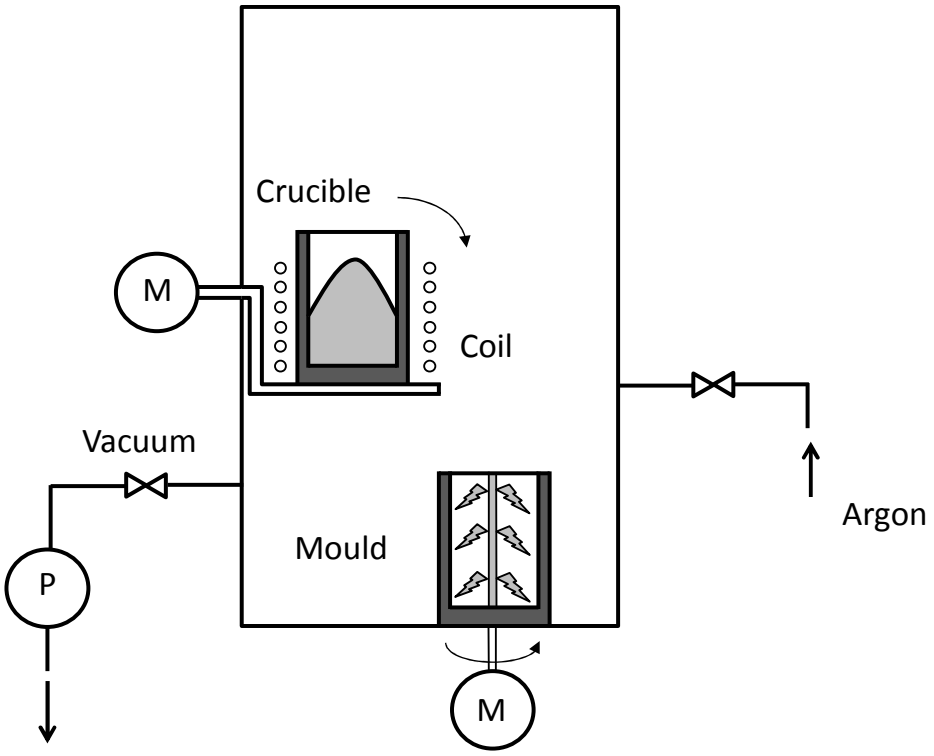


Figure 3.1. Scheme of a CCIM installation.

### 3.1.1 Stages of CCIM

CCIM has two distinguished stages: melting and casting. The first stage is related to the melting of the metal and it happens inside the cooper crucible. The second stage concerns to the casting and solidification of the metal in the mould after the pouring.

*Melting*

The first stage of the process is carried out inside the segmented water cooled cooper crucible. This crucible is surrounded by a coil supplying enough energy to melt and stir the molten metal. The magnetic field generated by the coil produces eddy currents in the metal. Due to the resistance of the metal, the charge is heated and melted by Joule heating. In addition, the metal is stirred and becomes in a suspended state under the effect of the electromagnetic fields.

When the charge starts to melt, a solidified layer called skull arises between the cooper crucible and the melt due to severe water cooling. This inner layer has the same ingredients as those of the melt and

therefore avoids contamination of the melt by the crucible, enabling the melting of pure metals or alloys (Figure 3.2).

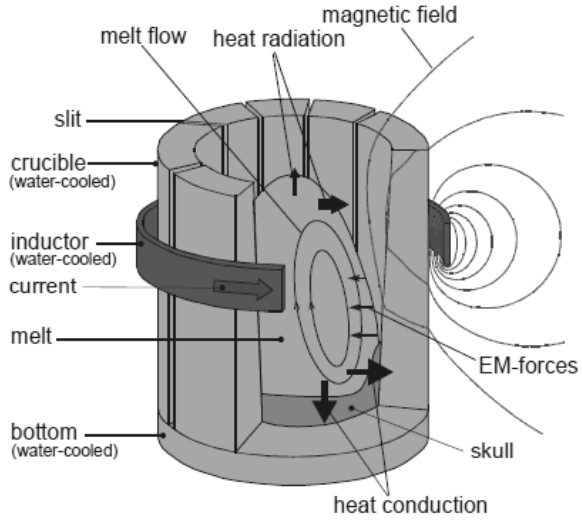


Figure 3.2. Melting, the first step of the process (Umbrashko 2005).

The main features of this stage are the superheat of the melt and the efficiency of the process. Hence, an optimal selection of the main parameters of CCIM (power supplied, frequency, crucible design, filling level of the crucible, coil design, and type of atmosphere) is essential in order to maximize both superheat and efficiency.

Physically, the problem can be described in the following way: according to Ampere's law, an alternating current that flows through a coil generates a time-harmonic magnetic field. Ideally, the magnitude of the magnetic field is related to the current by the proportionality factor $\mu_0$, which is the constant permeability for the space or vacuum. This magnetic field penetrates inside the segmented crucible through its slits. By Faraday's law, a voltage is induced in the charge, with an intensity proportional to the rate of change of the magnetic flux in the area encircled by the loop of the conductor and opposite in sign. The currents generated by the induced voltage, commonly called Foucault, dissipate the heat due to Joule effect. Moreover, the currents generated by this induced voltage results in a magnetic field that opposes the external magnetic field. At the same time, electromagnetic forces are also generated (Lorentz forces), which makes the charge to levitate, keeping it away from the crucible walls and avoiding the contamination of the molten metal. The Lorentz forces at a point is defined as the cross product of the electric current and the magnetic field vectors. Given that eddy currents and the associated magnetic field are tangential to the material surface, the Lorentz force is always normal and pointing into the surface.

In a classical induction furnace, the free surface is deformed in a static dome or meniscus shape. After some simplifications, the height $h_m$ of the dome is the result of the balance between the static pressure and the electromagnetic pressure (Fautrelle 2009, Xue 2009):

$$h_m = \frac{B_{eff}^2}{2\mu_r \mu_0 \rho g}, \tag{3.1}$$

where $B_{eff}$ is the magnetic field strength (r.m.s. value), $\mu_0$ is the permeability of vacuum, $\mu_r$ is the relative permeability, $\rho$ is the density, and $g$ is the gravity. The same equation can be applied to CCIM.

The mathematical formulation of the problem is discussed in detail in chapter 4.

*Casting*

The second stage consists of pouring the molten metal from the crucible to the mould, which is followed by a solidification process. For the case of titanium and titanium alloys, refractory moulds are often used with materials that do not react with the titanium alloys or have inhibitors that reduce or avoid these reactions. Furthermore, in order to increase the fluidity of the metal and fill all the cavities of the moulds, centrifugal casting and/or moulds preheated to high temperatures (800ºC-900ºC) are used.

### 3.1.2 Advantages/disadvantages

As reported in chapter 2, the CCIM exhibits several advantages:

- The melt stock can be basically anything that physically fits into the crucible.
- It is capable of melting nearly any alloy.
- CCIM offers homogeneity in alloys due to its inherent molten metal stirring caused by the magnetic field of the induction coil.
- Since the charge is melted by the applied magnetic field, there is no need for electrode fabrication.
- Copper crucible avoids any contamination of the charge material.

The major problem in CCIM is that the cooling water of the crucible carries out a large amount of heat, reducing the melting efficiency of the cold crucible. This energetic efficiency is low, about 5 to 20%. Furthermore, the superheat achieved by the melt is limited.

Although skull melting processes are capable of providing molten metal of high purity, they all have the disadvantage of providing only a low superheat, since much of the energy applied is lost in the water cooled crucible. The low superheat is often counter acted by pouring the molten alloy rapidly into the mould. However, this result in surface turbulence can generate bubbles, which are readily trapped by the rapidly solidifying metal (Harding 2006).

Other disadvantages include the requirement of a much larger power supply than VIM, low melt weight, and skull removal every time the melt chemistry is changed.

### 3.1.3 Materials melt in CCIM

The materials used in CCIM can be metals, ceramics, glasses, and even nuclear waste. Among the metals, the typical ones employed in CCIM are reactive metals such as Ti, TiAl, Zr, and Mo.

### 3.1.4 CCIM applications

Some applications of CCIM include:

- Fabrication of different products of titanium and titanium alloys such as intermetallics for a) biomaterials applications because of its excellent biocompatibility, corrosion resistance, and mechanical properties (Niinomi 2003a, Guillemot 2004); b) aeronautic components such as turbine blades, turbocharger rotors, and exhaust blades (Harding 2003, Tetsui 2011); c) automotive industry such as connection rods, exhaust system, and suspension springs (Gomes 2011); d) sports such golf club heads of titanium (Harding 2003).

- Fabrication of TiAl matrix composites (Kampe 1994, Niu 2012).

- Vitrification of radioactive waste (Sugilal 2007, Jouan 1996, Gombert 2003).

- Vitrification of glasses (Gombert 2003, Arellano 2007).

- Artificial generation of particulate material of inorganic compounds such as CsOH, NaOH, $SnO_2$, and $UO_2$ (Riemer 2011).

- Production of silicon (Kim 2007).

- Fabrication of directional solidification products (Hongsheng 2005).

### 3.1.5 Brief history of CCIM

In the 1970s, the U.S. Bureau of Mines (USBM) developed the first induction melting unit capable of economically melting reactive metals in a water cooled cooper crucible. Known as “induction slag” melting, this process used nonconductive calcium fluoride as electrically insulating slag between the titanium charge and the cooper crucible to prevent the arcing and crucible damage (Reed 1990). In 1980, the Duriron Co. investigated the casting of its own reactive metal components using its own variation of USBM’s induction slag process (Peters 1996). During the 80s, the technology was further developed into CCIM, which permits the melting of virtually any reactive metal or alloy without using an insulating slag.

Since the beginning of the 1980s, intensive experimental studies have been carried out. Several groups of physicists and engineers have been active in this field, particularly at Research Institutes in Moscow and Grenoble. Tir published investigations on how to improve the efficiency of CCIM (Tir 1984, Nikiforova 1984, Nikiforova 1990). The MADYLAM group coordinated by Garnier (Delage 1984, Delage 1981,

Gagnoud 1988, Gagnoud 1985, Gagnoud 1991) also presented remarkable theoretical and experimental results.

At the same time, several groups in Germany started researching in this process. The team directed by Choudhury at the ALD Company produced great advances (Choudhury 1996, Choudhury 1997). ALD, a manufacturer of modern melting units, concentrated on developing production processes for innovative and competitive TiAl parts for the automobile industry. Mathematical models of the electromagnetic, thermal, and fluid flow fields in CCIM were developed by the team of Muehlbauer at the Hanover University. In addition to these theoretical studies, experimental melting and casting tests of TiAl exhaust valves for automotive applications were also performed in Hanover (Bernier 2000, Baake 2003a).

Intensive investigations of the cold crucible processing of reactive metals were also undertaken in China (Guo 1999, Yanqing 2001), United Kingdom (Harding 2003, Bojarevics 2003), and other countries.

At the beginning stage of the cold crucible technology, the complexity of the problem only allowed analytical investigations of the induction cold crucible melting. Nevertheless, the improvement in the computer resources has made possible to perform advanced numerical models, coupling electromagnetic, thermal, and fluid flow fields.

## 3.2 Parameters

In the CCIM process, it is possible to distinguish parameters that act in the melting steps and parameters that play an important role in the casting process. The first ones have an influence in the superheat of the melt and in the efficiency of the process (section 3.2). The later ones, namely the intrinsic parameters of the investment casting process (section 3.3) and the tilting system of the molten metal from the crucible to the mould (Section 3.4), play an important role in the soundness of the fabricated parts.

### 3.2.1 Superheat and efficiency

The superheat of CCIM tends to be very small because there is a great heat loss by conduction from the charge to the crucible. This is undesired because together with the poor fluidity of titanium and titanium alloys, misruns can appear in thin wall castings. Hence, it is very important to generate a significant amount of superheat in order to avoid both misruns and cold laps in the cast parts (Gomes 2011). The superheating temperature of the entire melt is determined by the electromagnetic, hydrodynamic, and thermal behavior of the CCIM installation (Umbrashko 2005). Baake *et al.* (Baake 2003a) showed that the maximum superheating temperature is attained near the crucible wall and above the wall skull. At this point, the melt is close to the crucible wall but without direct contact to the skull. Thus, the ratio between the induced power density and the heat loss is maximum. In the center region of the melt, the temperature distribution is quite homogeneous due to the good turbulent mixing of the melt. The lowest temperature

values are attained near the skull, where no power is directly induced and high heat conduction losses occur.

Hence, it is important a good selection of parameters values in order to maximize both the superheat and the efficiency. The most important parameters of the melting step of CCIM are the power supplied (the current that emanates through the coil), the frequency, the crucible design, the filling level of the crucible, the coil design, and the type of atmosphere. Variations in any of the above factors influence the shape of the melt meniscus, and also the flow pattern and energy balance. Therefore, the influence in the superheat and the efficiency of the each parameter should be analyzed taking into account all of them.

### 3.2.2 Power (Current)

One of the first consequences of increasing the power is that the meniscus/dome height increases (Figure 3.3). In addition, there is less melt surface in contact with the crucible. This occurs because the Lorentz forces are greater. This change in the meniscus shape affects in the superheat and the efficiency.

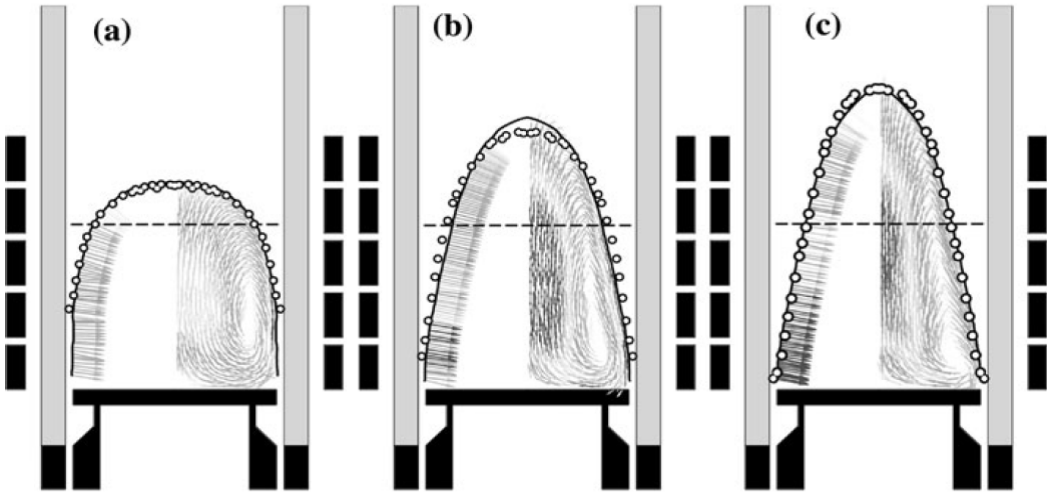


Figure 3.3. Free surfaces (○ experimental measurements and ─ numerical calculation) for different inductor effective currents $I_{ef}$: (a) $I_{ef}$ =1929 A, b) $I_{ef}$ =2956 A, and c) $I_{ef}$ =3566 A (Spitans 2013).

Bojarevics *et al.* (Bojarevics 2004) reported that superheat increases with higher power (Figure 3.4). However, the superheat only rises until a particular value. This value depends on the characteristic of the installation and the parameters used. From that value, there is not a consistent increment in the superheat. An explanation of this phenomenon is that rising the power tends to increase the melt temperature and this reduces the combined thickness of the mushy zone and the solid skull, increasing the heat loss through the base and the wall. Guo *et al.* (Guo 2000) noted that the thickness of the skull wall decreases and its height falls continuously with higher power. According to Baake *et al.* (Baake 2003a), there is not an increment of the superheat because the meniscus is keep far from the crucible, reducing the electromagnetic coupling and hence, the total power generation in the melt.

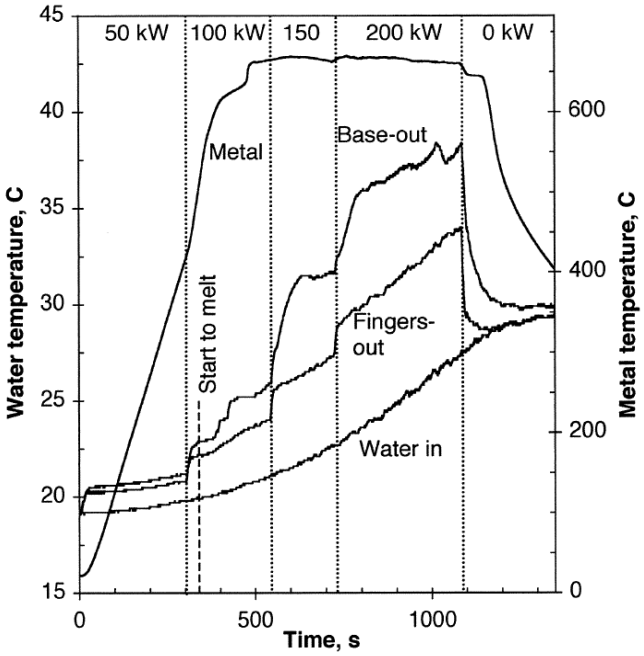


Figure 3.4. Water and metal temperatures during CCIM of 3.6 kg of an Al alloy (Bojarevics 2004).

Bojarevics *et al.* (Bojarevics 2004) also demonstrated that the efficiency of the process reduces rising the power because the molten metal temperature does not increase whereas the heat loss of the crucible does (Figure 3.5).

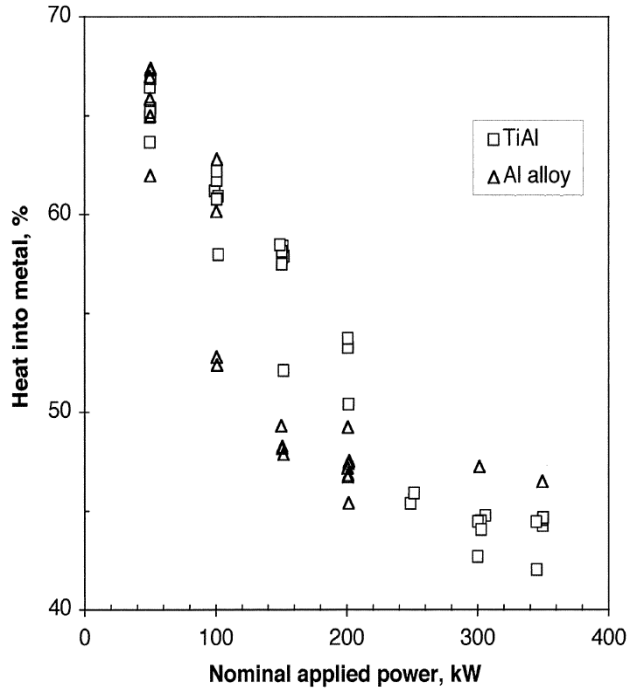


Figure 3.5. Energy efficiency of CCIM furnace when melting Al and TiAl alloys (Bojarevics 2004).

### 3.2.3 Frequency

The influence of the frequency in the meniscus shape is less sensitive than that of the power. Spitans *et al*. (Spitans 2010) observed that the largest meniscus deformation occurs at a particular frequency (400 Hz in their experiment). A frequency increase generates a sharp surface deformation only near the crucible wall. The surface becomes flat close to the symmetry axis (from 5 kHz the height of the meniscus remains almost constant).

The theory predicts that the power released within the inductively heated charge increases proportionally with the square root of the AC frequency. However, this is true only for a given fixed external magnetic field intensity, which is equivalent to a fixed current magnitude in the exciting coil. Keeping the current constant and increasing the frequency, the heat induced in the charge rises (Table 3-1). However, a higher frequency entails a significant power loss in all the system (crucible, cables,…). Hence, for a fixed coil current, the superheat increases rising frequency, but this requires a higher power input in the power supply (Bojarevics 2004).

On the other hand, for a fixed power, a frequency reduction increases the current that emanates from the coil. Thus, melt temperature rises significantly. However, at low frequencies, instability of the free surface can appear, leading to free surface perturbations. Hence, larger frequencies are preferable for the confinement stability and heating rate, although electrical breakdown may appear in the coil.

The temperature variations for different frequencies under the conditions of both fixed current and fixed electrical power released in the melt are summarized in Table 3-1 (Bojarevics 2004).

Table 3-1. Effect of coil frequency on the maximum temperature under conditions of either fixed coil current $I$ or fixed electrical power $P_e$ for TiAl intermetallics (Bojarevics 2004).

| | Constant current | | | Constant power | | |
|---|---|---|---|---|---|---|
| $f$, kHz | $I$, A | $P_e$, kW | $T$, ºC | $I$, A | $P_e$, kW | $T$, ºC |
| 3.5 | 6700 | 160 | 1565 | 8040 | 220 | 1623 |
| 7 | 6700 | 223 | 1588 | 6700 | 220 | 1588 |
| 14 | 6700 | 345 | 1615 | 5695 | 220 | 1583 |

Baake *et al*. (Baake 2003a) observed the same results (Figure 3.6). With a fixed power, a lower operating frequency leads to a higher superheat, since the heat conduction losses through the wall skull decrease.

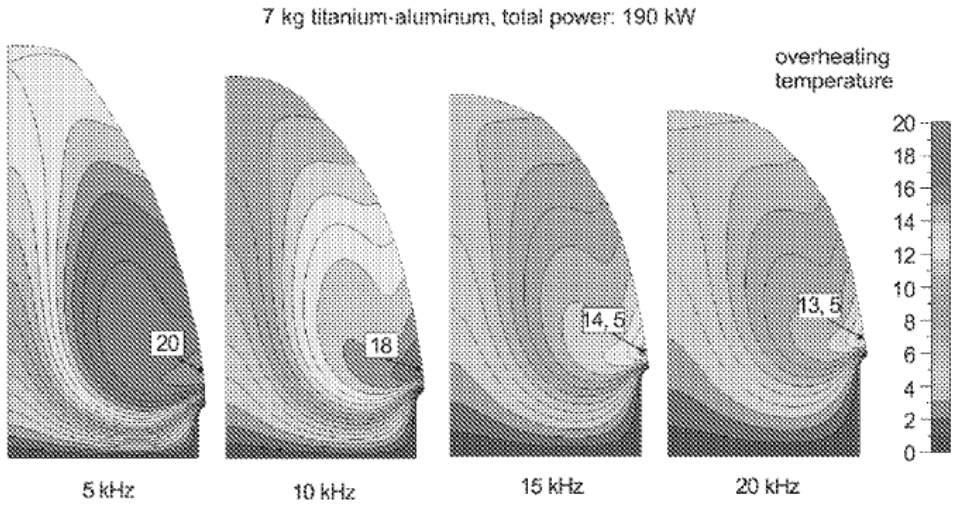


Figure 3.6. Influence of the frequency on the meniscus shape and superheat (Baake 2003a).

Regarding the efficiency, both Bojarevics *et al.* (Bojarevics 2011) and Delage *et al*. (Delage 1984) discovered that for a fixed current in the coil, the electrical efficiency improves when increasing the frequency until certain saturation value. This saturation value depends on characteristics of the CCIM installation.

### 3.2.4 Influence of the crucible filling level

The filling level is another important parameter affecting the superheat and the efficiency. The rise of the melt mass leads to a stronger electromagnetic coupling between the melt and the inductor. As a result, the electrical efficiency increases and the superheat improves (Figure 3.7). The main reason lies on the increment of the induced power in the melt, which overcompensates the heat conduction losses through the crucible (Baake 2003a). Hence, the melting process in CCIM should be always carried out with a maximum filling level to boost the superheat, taking always into consideration possible instabilities of the free surface, which can spill the melt out of the crucible.

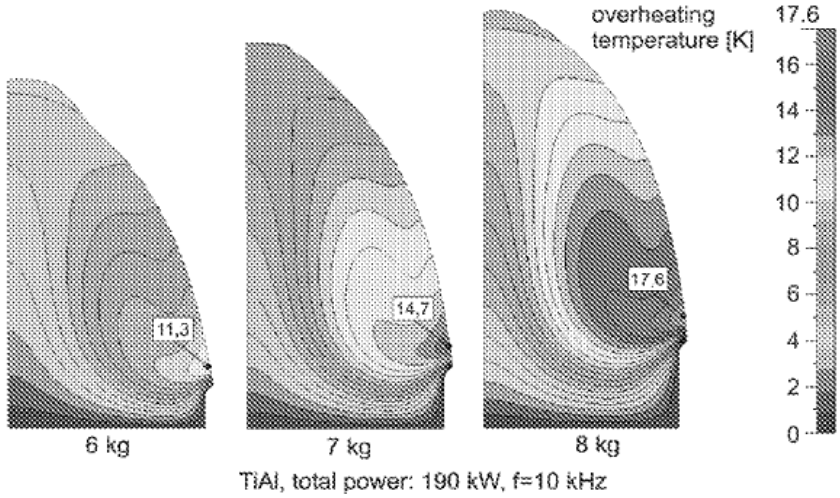


Figure 3.7. Influence of the filling level in the superheat (Baake 2003a).

Bojarevics *et al.* (Bojarevics 2004) stated that if the coil current input is kept constant for all charge weights, the resulting temperatures at the top part of the molten metal are significantly different. This is mostly related to the electrical efficiency of the coupled system: the higher the filling factor, the higher the efficiency and, as a result, the higher the temperature (Figure 3.8).

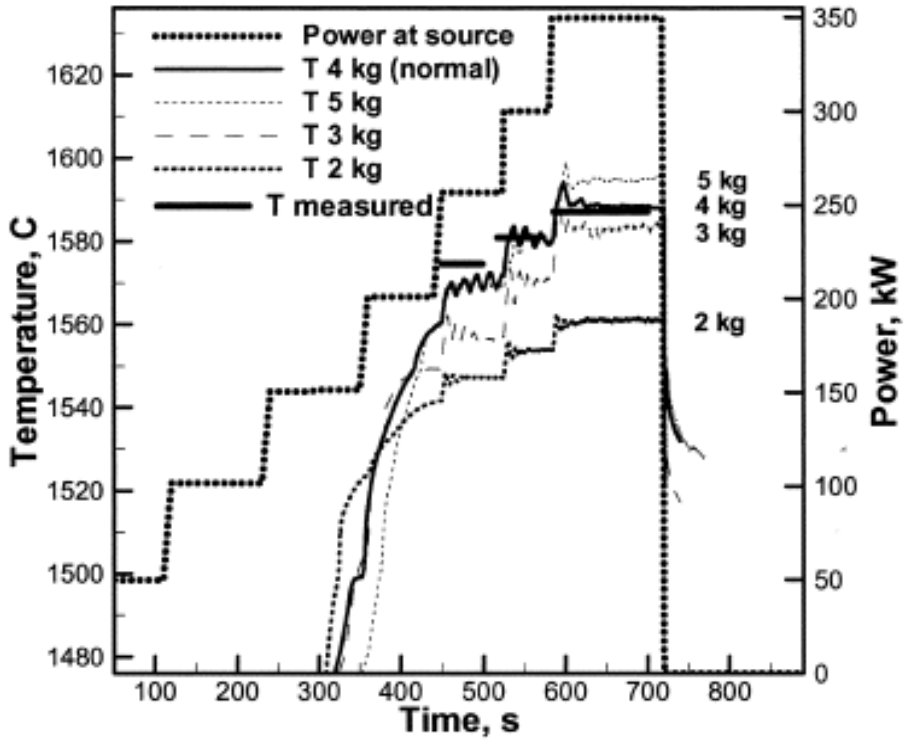


Figure 3.8. Comparison of numerically simulated temperatures for various melt weights of TiAl and measured temperature data for 4 kg load (Bojarevics 2004).

### 3.2.5 Crucible design

#### 3.2.5.1 Ratio height/diameter of the crucible (*H/D*)

The ratio between the height and the diameter of the crucible (*H/D*) is another important design criterion of CCIM, since it has an influence in the shape of the free surface. Baake *et al.* (Baake 2003a) showed that the electrical efficiency increases with higher *H/D* (the height of the crucible is kept constant while the diameter is reduced).

Despite heat conduction losses rise with higher *H/D* ratio due to the increment of the height of the wall skull, the induced power in the melt also increases. As a result, the superheat is improved (Figure 3.9).

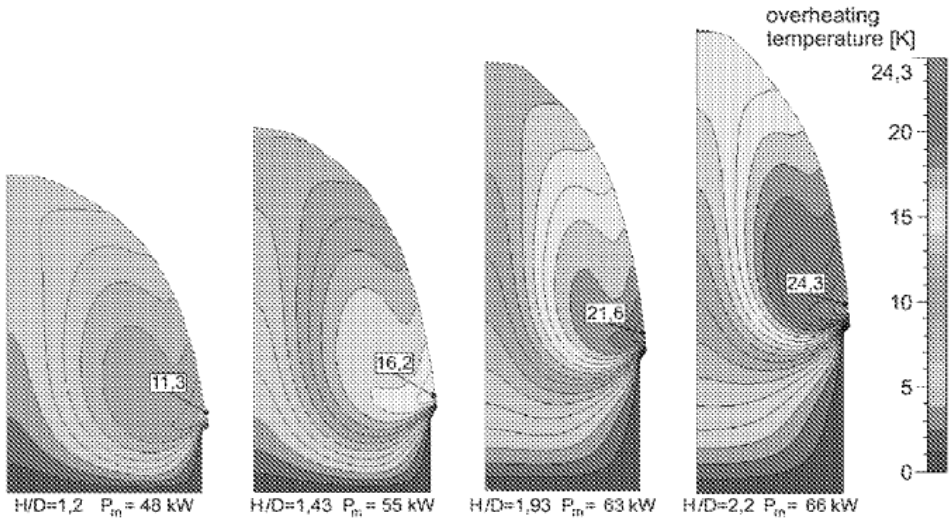


Figure 3.9. Influence of the H/D ratio in the superheat (Baake 2003a).

3.2.5.2 Number and dimensions of the slits

The power induced in the melt strongly depends on the number and width of the slits. The heat losses in the copper fingers are significant due to the copper high thermal and electric conductivities. Therefore, the goal is to optimize the number and position of the cooper sector in the crucible in order to minimize these losses. Cingoski *et al.* (Cingoski 1994) demonstrated that the efficiency of the furnace depends on the number and the width of the slits/gaps and wider air gaps improve the efficiency.

Iwai *et al.* (Iwai 1995) reported that the resistance of the crucible decreases and the inductance increases with wider slits (Figure 3.10).

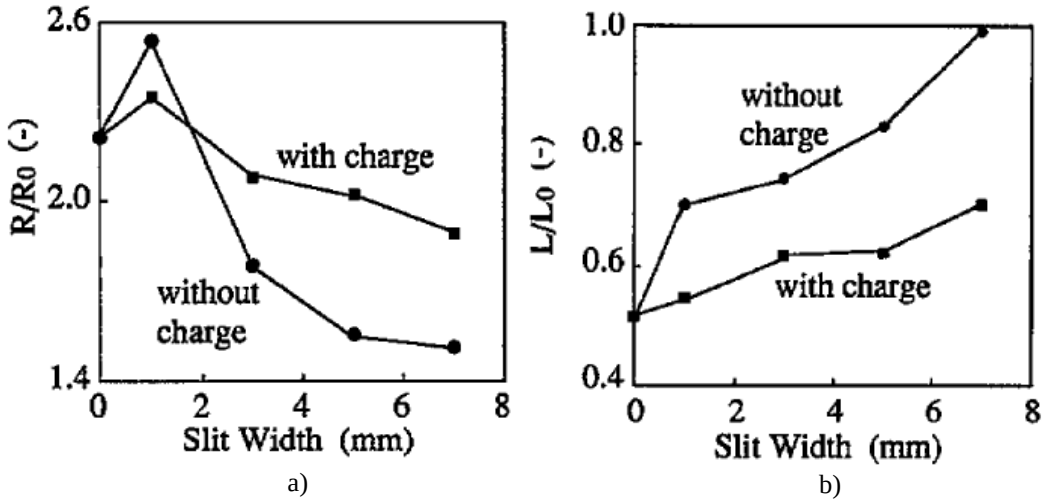


Figure 3.10. a) Effect of the slit width on the resistance of the crucible respect $R_0$, which is evaluated under condition of neither charge nor crucible and b) effect of the slit width on the inductance of the crucible (Iwai 1995).

Iwai *et al.* (Iwai 1995) reported that under a constant coil current and high frequencies, the total heat in the charge ($Q_{ch}$) and the crucible ($Q_{cr}$) decreases with wider slits (Figure 3.11).

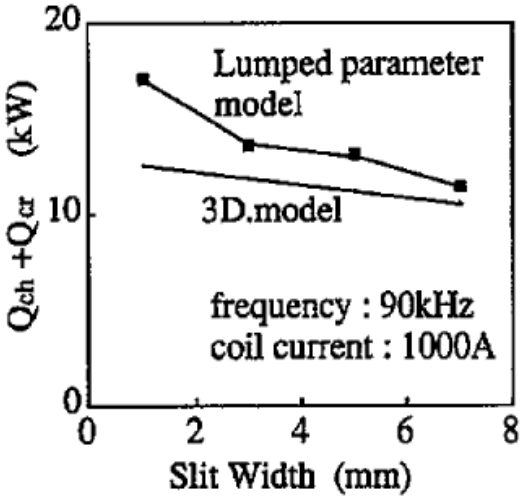


Figure 3.11. Heat generation in the charge and the crucible in relation to slit width (Iwai 1995) .

Figure 3.12 shows the effect of slit width on the ratio of the heat generation in the charge, the crucible, and the coil regarding to the total heat. The larger the slit width, the larger are the ratios in the charge and the coil, and the smaller is the ratio in the crucible. Hence, there is an improvement of the efficiency, although the power in the melt decreases.

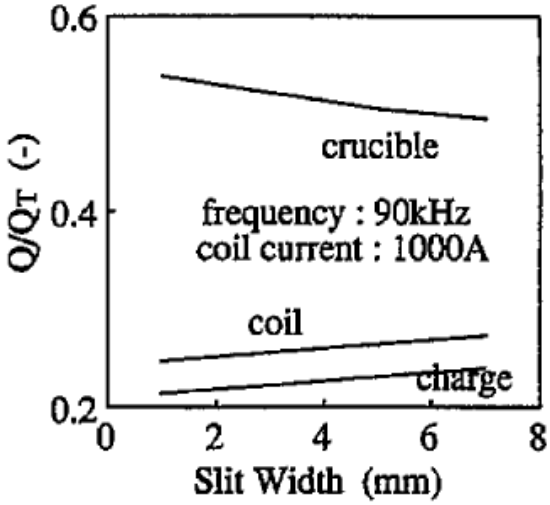


Figure 3.12. Effect of the slit width on the ratio of heat generation in the charge, crucible, and coil with respect to the total heat (Iwai 1995).

It is important to take into account that the contribution of the inductance is usually much larger than resistance at high frequencies. Narrow slits cold crucible produces low voltage operations (Iwai 1995). Furthermore, the width of the slits should be very narrow since wider slits allow molten metal load to

penetrate in the slits, where it freezes as skull. Skull formed with these irregular protrusions into the slits becomes extremely difficult to remove from the crucible and typically results in damage to the crucible.

On the other hand, several authors (Delage 1984, Delage 1983) have reported that there is an increment in eddy current losses (power transmitted) in the crucible for a given current with the increment in the number of segments. Hence, it is possible to reduce electrical losses by reducing the number of segments. Nikiforova *et al.* (Nikiforova 1990) reported that the efficiency decreases as the number of crucible segments increases. However, this method is not very promising since there is an abrupt fall in the release on the energy (Tir 1984). Usually, cold crucibles are made of several segments to keep the voltage drop low enough between two adjacent segments (Delage 1984).

For a fixed power, variations in the number of slits and their width change the total resistance of the crucible, and therefore, the current that flows for the coil also varies.

### 3.2.6 Coil design

The design of the coil is another important parameter of CCIM. Ruirun *et al.* (Ruirun 2012) demonstrated that the induction coil with racetrack section shows the optimal performance for increasing the magnetic field intensity.

The increase in the number of turns coil turns produces greater Lorentz forces, being the magnetic field distribution similar. However, the required voltage to drive the needed current limits the number of coil turns.

### 3.2.7 Type of atmosphere and partial pressure of the gas

Harding *et al.* (Harding 2003) showed that the superheat increases if the melting of the charge is performed in argon rather than in vacuum. Moreover, higher argon pressure increases the superheat of the melt. The average superheat was 33ºC when TiAl was vacuum melted, the superheat increased to 44ºC when TiAl was melted under a partial pressure of 200 mbar and to 62ºC with an argon pressure of 800 mbar.

The type of atmosphere and the partial pressure of the gas play a crucial role in the composition of the final components (Guo 2000). Depending on the vacuum level in the melting chamber, losses by evaporation of elements with high vapour pressure are very significant. This aspect is particularly important when melting TiAl based alloys due to the high vapour pressure of Al, which is 300 times higher than Ti, and its low melting temperature compared with Ti (Gomes 2013). On the other hand, if melting is performed at high pressure, metal contamination will occur between the molten metal and the atmosphere. Thus, a suitable equilibrium between pressures has to be established to avoid alloy contamination and/or excessive aluminium loss.

In case of titanium intermetallics as Ti-48Al, Gomes *et al*. (Gomes 2013) identified two threshold level pressures corresponding to a critical pressure (Pc) and an impending pressure (Pi). Melting pressure below around $10^{-1}$ mbar increases aluminium losses. The rate of loss, which is the ratio of aluminium atomic percentage to time (at%/s), increases as melting pressure decreases until a maximum rate is reached. Then, the loss rate keeps constant for lower pressures (Figure 3.13). Jingjie *et al.* (Jingjie 2002) developed a theoretical model to describe this evaporation.

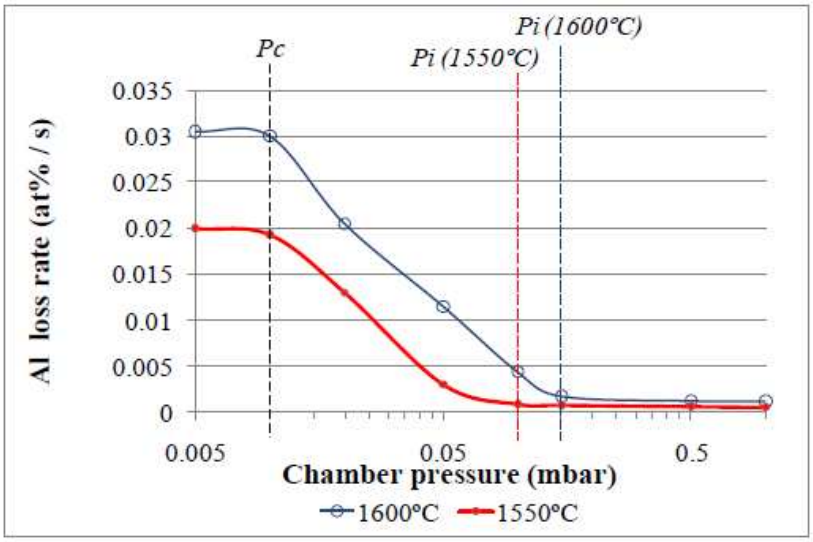


Figure 3.13. Al loss rate (at%/s) as a function of melting chamber pressure and melt temperature (Gomes 2013).

### 3.2.8 Skull formation

The skull acts as a protective layer. However, a great amount of skull in the crucible after pouring means that not all material in the charge has been used. Guo *et al.* (Guo 2005) investigated the ratio of skull weight and charge weight (*Rs*). They set up an exponential relationship between *Rs* and both the input power and the weight of the load. They noted that increasing the input power both the thickness of the skull bottom and the height of the skull wall decrease. Westphal *et al.* (Westphal 1995) calculated the skull thickness and height analytically.

### 3.2.9 Improve of superheat using a DC magnetic field

Harding *et al.* (Harding 2005) showed that the addition of a DC field increased the superheat in TiAl from 45ºC (AC field only) to 81ºC (DC+AC).

DC current flowing through the DC coil creates a DC magnetic field that is superimposed to the AC field. When the molten charge moves across the field lines of the DC field, additional currents are induced in the moving metal. Such currents react with the DC flux to produce a braking action that reduces the fluid velocity (Davidson 2001). Such damping reduces the turbulence in the liquid metal near the bottom of the

cold crucible, reducing the heat convective transferred from the liquid metal into the skull. Thereby, there is a significant increase of superheat (Widlund 2000, Bojarevics 2006).

### 3.2.10 Power demand

The total energy transmitted by the power supply is not only used to melt the charge. Electric losses appear both in the segments of the crucible and in the coil due to Joule effect. They also appear in the power leads and coaxial port. Thus, the power to heat, melt, and superheat the charge can be calculated as:

$$P_{melt}(t)=P_{power\ supply}(t)-P_{inductor}(t)-P_{crucible}(t)-P_{leads}(t)-P_{coaxial\ port}(t)-P_{loss}(t), \quad (3.2)$$

where $P_{melt}(t)$ is the power losses in the melt, $P_{power\ supply}(t)$ is the power losses in the power supply, $P_{inductor}(t)$ is the power losses in the inductor, $P_{crucible}(t)$ is the power losses in the crucible, $P_{leads}(t)$ is the power losses in the leads, $P_{coaxial\ port}(t)$ is the power losses in the coaxial port and $P_{loss}(t)$ is the remaining power losses.

In the melt, there is a heat flow from the melt through the skull to the crucible, where the heat is being removed by the cooling water. In addition, heat losses can occur due to radiation, especially for melt in crucibles with large diameter. In order to obtain an overall power balance, these losses must be replaced by an equivalent energy absorption in the melt ($P_{loss}$) (Gross 1999). The water of the crucible cooling system contains the ohmic losses due to the crucible currents and the conduction, radiation, and convective thermal losses of the melt. In case of the inductor losses, there are only ohmic losses. The remaining part of the power is used to melt the charge.

The required electrical power strongly depends on the selected frequency, which must be adjusted to the electrical conductivity of the melt and size of the crucible. The electromagnetic field is not only absorbed in the melt, but also in the inductor coil and the crucible, which are usually made of copper. These ohmic losses can become significant at an unfavourably chosen frequency. Above a characteristic frequency, where the skin depth is equal to about one half of the melt radius, only a small percentage of the overall power is lost in the copper coil (Gross 1999).

Westphal *et al.* (Westphal 1995) made very interesting analytical calculations of the power loss for each element, analyzing the influence of each parameter.

## 3.3 Investment casting of titanium

The second step of CCIM consists of casting. The traditional route to cast titanium part is the combination of cold crucible induction melting with the investment casting process (Bojarevics 2003b, Choudhury 1996, Choudhury 1997). The investment casting is the most used technology to cast high quality components (Mueller 2005). The reason is that investment casting offers several advantages in the

fabrication of titanium components in its applications in relation to permanent moulds and graphite moulds, which are the other feasible alternatives. The advantages of investment casting include:

- Very high precision.
- Fabrication of any shape or complexity castings.
- Production of near net shaped castings. The possibility to complete elimination or substantial minimization of machining work on castings may make the process very cost effective.
- Although castings of 20 kg or more are produced, small castings of 10 g can also be produced.
- Fabrication of thin walled castings (approx. 0.75 mm to 1.00 mm).

The process of the creation of investment moulds, which consist of covering the wax patterns with ceramic materials, involves a number of basic steps (Figure 3.14). Firstly, a wax pattern is produced with the same geometry of the final product. Wax gating is attached to the pattern to allow the metal to flow inside the mould. The wax assembly is then dipped in a series of ceramic slurries to build up a ceramic shell. The application of slurry coating and stucco (refractory particles) on wax pattern assembly is repeated, with drying between each successive coat, until a shell mould of sufficient thickness develops. The first layer consists normally of a fine coating in order to obtain a good surface finish on the casting. Subsequent layers are made of ceramic slurry and refractory granules. The wax is then removed from the shell in an autoclave by exposure to moderately high temperature and pressure. Finally, the shell is fired at high temperature to increase the strength of the ceramic mould (Aguilara 2011).

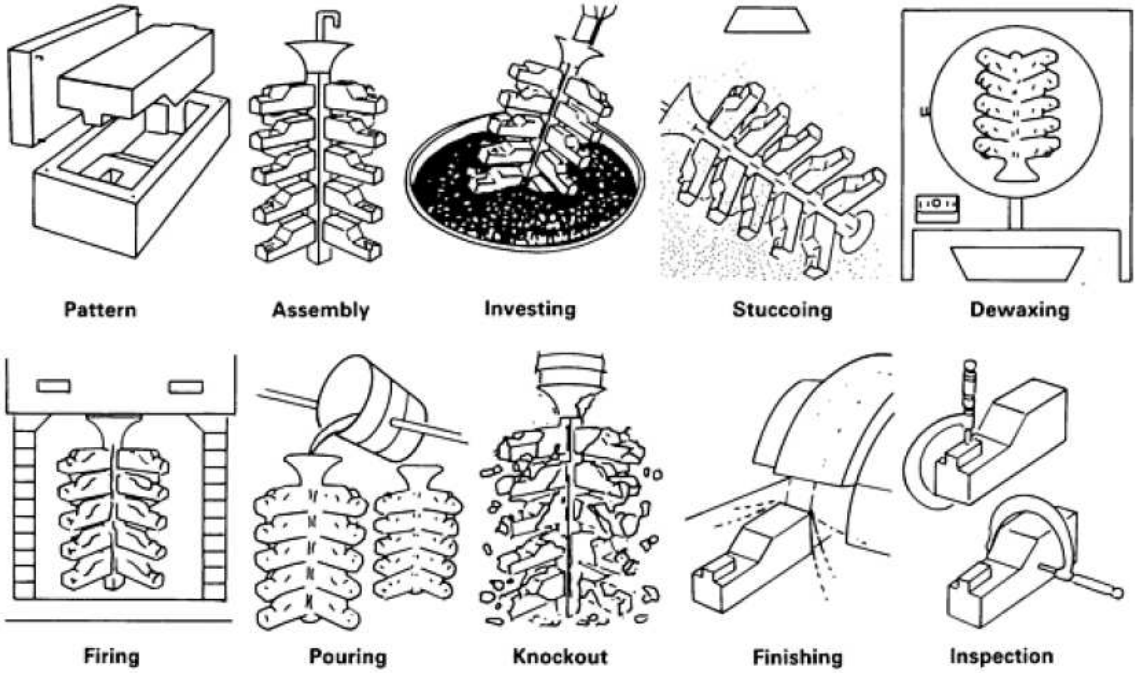


Figure 3.14. Basic steps of investment casting (ASM 1988).

The key requirements of an investment casting moulds include (Jones 2003):

- Sufficient green (unfired) strength to withstand wax removal without failure.
- Sufficient fired strength to withstand the weight of cast metal.
- Sufficiently weak to prevent hot-tearing in susceptible alloys.
- High thermal shock resistance to prevent cracking during metal pouring.
- High chemical stability.
- Low reactivity with the metals being cast to improve the surface finish.
- Sufficient mould permeability and thermal conductivity to maintain an adequate thermal transfer through the mould wall and hence, allow the metal to cool.
- Low thermal expansion to limit dimensional changes within the mould wall and ultimately, the casting.

### 3.3.1 Reactivity and alpha case

The production of quality titanium castings is a difficult task due to the next three factors:

1) High melting point.

2) Low fluidity.

3) Highly reactive with nearly all gasses, liquids, or solids.

Although each factor generates processing difficulties, it is the third one the one that most hinders the capability of titanium casting technology.

Due to the great chemical reactivity of titanium at high temperatures, reactions occur between molten titanium and the shell mould. This is due to the capability of titanium to reduce some oxides usually used for the fabrication of mould materials. The result of this interaction is an oxygen enriched surface layer known as alpha case (α-case) (Frueh 1997).

This hard surface layer of α-case is composed of titanium oxide, titanium silicates, and solid solutions (Papadopoulos 1999). Miyakawa *et al.*(Miyakawa 1989) reported that for titanium castings, the α-case is constituted by four layers.

The presence of the α-case is responsible for the inferior mechanical properties of titanium castings and compromises the mechanical properties (Papadopoulos 2009). It is a very deep brittle layer and lends itself to crack initiation and propagation.

Several researchers have investigated the α-case. Boettinger *et al.* (Boettinger 2000) predicted the α-case thickness by coupling the cooling histories obtained from heat flow simulations with a simple model for diffusion of oxygen in the bulk alloy for Ti-6Al-4V. Sung *et al.* (Sung 2007, Sung 2008) analyzed the formation of α-case and confirmed that it is formed not only by an interstitial element, but also by substitutional metallic elements dissolved from mould materials.

Investment mould oxide composition, mould temperature, and casting temperature are the most important parameters to reduce as much as possible the α-case layer and increase the soundness of the cast surface (Cruz 2005).

#### 3.3.1.1 Investment mould oxide composition

The most obvious difference in the investment casting of titanium alloys regarding other metals is the investment slurry formulation. In ferrous casting, the investment mould materials usually consist of zirconia, silica, and alumina. The same refractories cannot be used to construct moulds for titanium castings due to the titanium strong affinity with oxygen. These refractories would lead to moulds that would produce titanium castings with unacceptable surface finish and gross porosity.

It has been reported by many authors that moulds based in silica are not adequate to melt titanium. Until now, as reported by Gomes *et al.* (Gomes 2011), there are no refractory materials absolutely inert for titanium and titanium alloys. Interactions between titanium and mould materials always take place, leading to metal contamination.

Thermodynamic helps researchers to identify suitable mould materials. A typical analysis involves a comparison of the free energy of formation ($\Delta g^0_f$) of the candidate refractory in relation to titanium. This free energy of formation is also called Gibbs free energy of formation.

The comparison of the free energy of formation between compounds is a rather simplistic approach because it neglects solution effects. Moreover, most commercial binders in ceramic shell moulds are made from colloidal silica. Thus, regardless of the chemical stability of the refractory, its effectiveness will be undermined by the presence of the siliceous binder (Frueh 1997). However, researchers continue using this methodology.

As more negative is $\Delta g^0_f$, more stable is the compound. Figure 3.15 shows the standard free energy dependence on temperature, where it is possible to observe that $Y_2O_3$, $ZrO_2$, $Al_2O_3$, CaO, and MgO lead to good results.

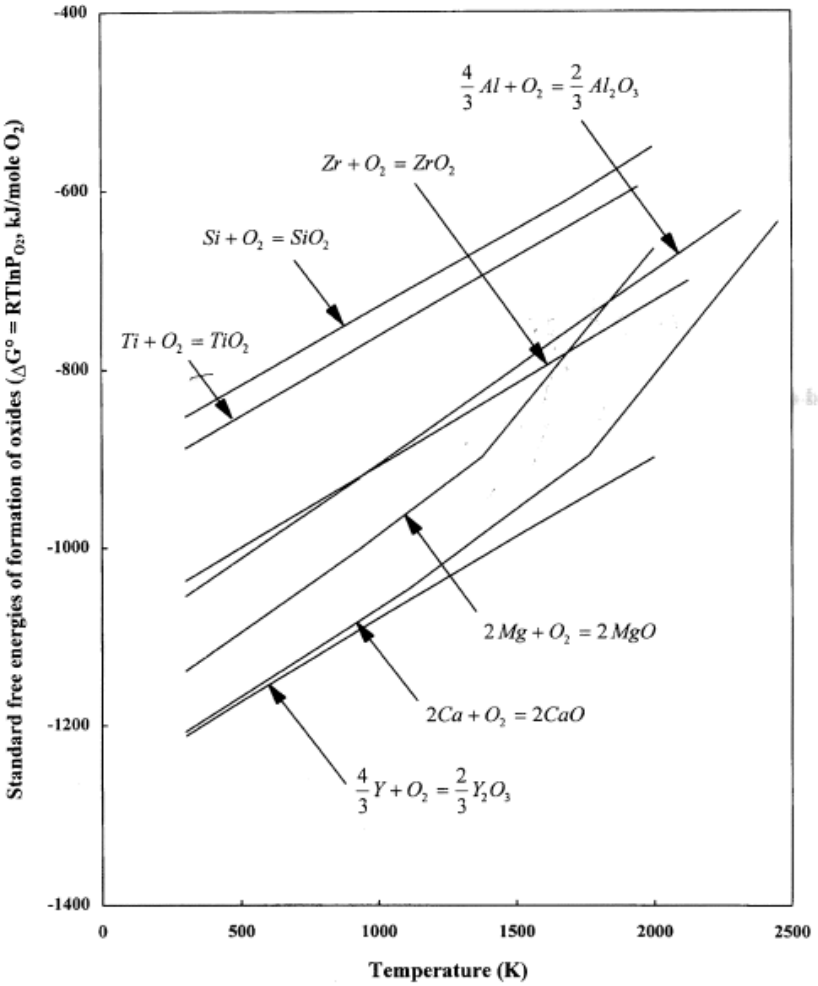


Figure 3.15. Standard free energy of formation of oxides (Kuang 2001).

Consistently, ceramics such as CaO (Tsutsumi 2010, Kim 2002), $ZrO_2$ (Lin 1999, Jia 2006), MgO (Hung 2003, Ida 1982, Hung 2004), $Al_2O_3$ (Yu 2010), and $Y_2O_3$ (Kim 2002, Renjie 2010, Suzuki 1997) have been adopted for mould materials, because their standard free energy are more negative than that of $TiO_2$.

Taking into account the Gibbs free energy of formation, Kostov *et al.* found that $Y_2O_3$ presents the most negative value among common metallic oxides, suggesting that it is a suitable material to be used as moulds for casting TiAl alloys (Kostov 2005). Suzuki *et al.* (Suzuki 1997) also demonstrated that $Y_2O_3$ exhibits a superior stability with the most favorable features of surface properties. However, the use of $Y_2O_3$ is limited by its prohibitive cost (Frueh 1997).

Among the other refractory materials, CaO is the most stable. However, CaO still has operative problems: it hydrates easily and it is difficult to manipulate (Kuang 2001). Thus, the process of making and storing CaO moulds becomes challenging. Pei-Ling *et al.* (Pei-Ling 2011) reported the same conclusion.

Kuang *et al.* (Kuang 2001) concluded that $ZrO_2$ is unsuitable as mould whereas $Al_2O_3$ shows good results. Kim *et al.* (Kim 2002) realized that not visible interaction exists between the $Al_2O_3$ moulds and TiAl

melts, nor an increase of hardness at the interface. However, pure titanium reacts with $Al_2O_3$, resulting in the formation of a TiO and a $Ti_3Al$ phases.

Hence, $Y_2O_3$ and CaO are the materials that less reaction have to titanium. However, they are not used because they are expensive and difficult to fabricate respectively. Among $ZrO_2$ and $Al_2O_3$, $Al_2O_3$ offers better results. The reactions of MgO are lower, although the duration of the bath is too short, converting MgO industrially inefficient.

More studies comparing different investment materials can be found in the literature (Miyakawa 1989, Zhao 2011, Altindis 2011, Kikuchi 2001).

#### 3.3.1.2 Mould temperature

The mould temperature is another important parameter during casting. If the mould temperature is too low, the metal cannot flow easily inside it. Preheating the ceramic mould is beneficial because fewer bubble defects appear in the final product since solidification rate is lower. Furthermore, the lower temperature gradient reduces the total level of porosity (Campbell 1991). However, higher temperature increases the risk of metal mould reactions affecting the surface structure and properties (Gomes 2011, Harding 2011). Thus, a reasonable value of the mould temperature is very important for the investment casting of titanium alloys.

Oliveira *et al.* (Oliveira 2006) reported that the critical temperature to avoid contamination was 600ºC. Above this temperature, the contamination was very severe. Iiyama *et al.* (Iiyama 2009) discovered that the α-case could increase to 500 μm if the mould temperature was above 600°C and recommended to carry out titanium casting at mould temperatures below 400ºC. They also reported that high mould temperatures adversely affected durability as well as mechanical strength of the parts.

#### 3.3.1.3 Casting temperature

The temperature of the titanium entering in the mould affects to the soundness of the casting. If the superheating temperature of the molten metal is poor, this can lead to shrinkage. However, if the temperature is too high, porosity and mould metal reactions may appear.

### 3.3.2 Fluidity

Section 3.3.1 discussed the negative influence of the reactivity of titanium in the properties to the final product. The other negative factor for production of quality titanium (together with the titanium high melting point) is the low fluidity of titanium.

Due to the low superheat of CCIM, it is difficult to fill thin castings, which results in casting defects. Furthermore, this poor fluidity leads to shrinkage and gas defects. The low superheat is often counter acted by pouring the molten alloy rapidly into the mould. But this can result in surface turbulence (Harding 2006).

The preheating of the moulds is one of the solutions to overcome this poor fluidity (Harding 2011, Wang 2011). Other factors that play an important role in the porosity and/or inadequate mould filling in titanium castings include:

- The pressure of inert gas and gas type (Zinelis 2000, Hero 1993).
- Permeability of the investment casting (Zinelis 2000, Hero 1993).
- Venting (Wang 2011, Hero 1993).

## 3.4 Casting processes

Investment casting process is the traditional route to cast titanium parts with the combination of cold crucible melting. This means the use of ceramics moulds instead of permanent or graphite moulds. Casting processes can also be differentiated depending on how the titanium is transferred from the crucible to the mould.

To date, titanium castings have been fabricated using gravity casting, tilting casting, countergravity casting, and centrifugal casting (Kuang 2001, Harding 2004).

- Gravity casting

The majority of castings of titanium are made using top gated gravity casting, which consist of pouring the metal downhill from the crucible into the mould. In order to overcome the poor fluidity of titanium alloys (caused by the low superheat), the molten metal is poured rapidly into the mould (Harding 2004). Unfortunately, turbulences occur once metal exceeds a critical velocity (Harding 2006). This can easily result in a thin oxide film defect. This surface turbulence also leads to the development and entrainment of bubbles, which sometimes are trapped inside the solidifying metal generating undesired porosity (Figure 3.16).

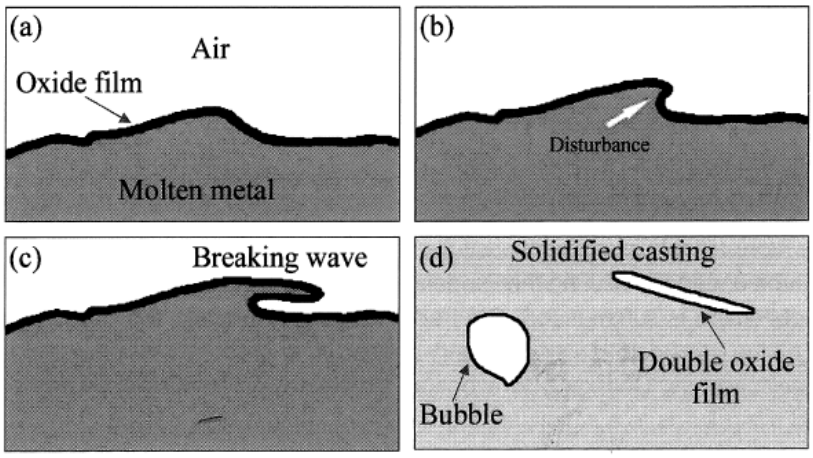


Figure 3.16. Schematic effect of surface turbulence during mould filling (Harding 2006).

Harding *et al.* (Harding 2006, Harding 2004) demonstrated that bottom gated gravity casting offers better results. As a result of controlling the critical velocity, the surface turbulence can be drastically reduced.

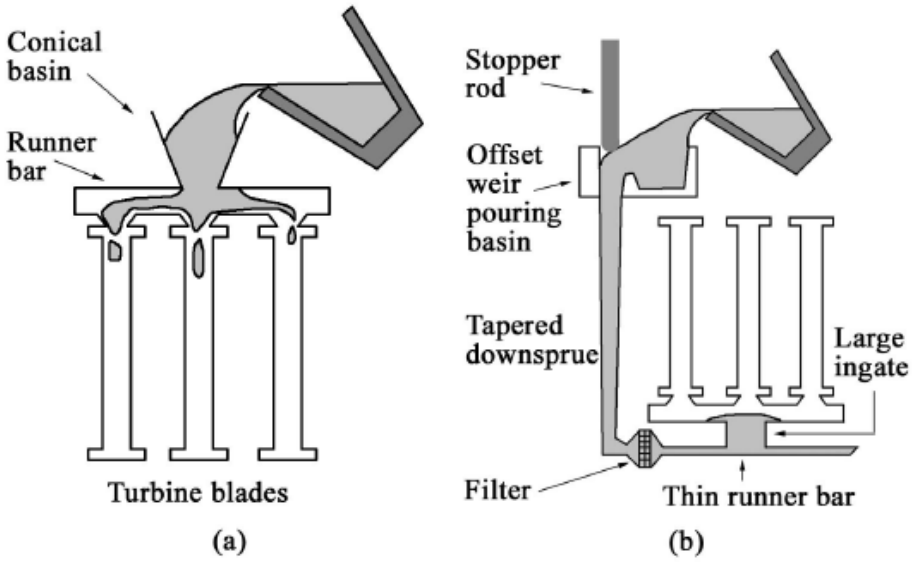


Figure 3.17. a) Top gated gravity casting and b) bottom gated gravity casting (Harding 2004).

- Tilting casting

A lower proportion of titanium casting is produced by a tilting technique, where the crucible and mould are brought together and rotated about their point of contact (Wang 2012).

- Countergravity casting

The third fundamental metal transfer mode is the countergravity filling, where metal is pumped uphill into the mould (Harding 2006).

- Centrifugal casting

The last technique is the centrifugal casting. The centrifugal forces enhance the fluidity of molten titanium. There are two ways of applying the centrifugal force: the vertical and horizontal ones.

In case of CCIM, all of these casting processes can be used. However, the centrifugal casting (together with the gravity casting) is the most used (Bojarevics 2003b, Harding 2011, Li 2010, Aoyama 2005). The rotational velocity of the mould is the most important parameter to control the porosity and the adequate filling of this casting process (Yongliang 2008, Li 2010).

In these processes, it is crucial to avoid turbulences. Before pouring, the free surface of most molten metals and alloys is covered by a film (usually an oxide) with a composition, thickness, and physical properties that depend on the alloy, the temperature, and the surrounding environment. Many molten metal transfer operations often occur under conditions that lead to surface turbulence, which result in the

surface folding over onto itself. Contact can occur between the oxide films. Thus, wetting and bonding do not occur between these films. Hence, these defects of liquid persist even in the solidified casting. Moreover, turbulent flow can also generate bubbles (Harding 2006).

Despite the improvements performed in these casting processes, the casting of titanium remains as a significant challenge to industry and often leads to some deleterious defects, such as a) misruns, which arises if the melt has too low superheat, b) surface shrinkage due to the collapse of entrained bubbles, and c) hot-tearing and cracking during solidification and cooling (Harding 2001). Muraleedharan *et al.* (Muraleedharan 1996) showed that the cooling rate plays an important role in the quality of the castings. The variations of the cooling rates affects in the solidification structure, and thereby, in the resulting mechanical properties.

## 3.5 Conclusions

Several parameters and factors play a crucial role during the fabrication of titanium parts. In the melting stage, variations in any mentioned parameters influence the shape of melt meniscus, and as a result, flow pattern and energy balance.

There exist a plethora articles dedicated to the influence of the power, the filling level, and the frequency in the superheat and the efficiency of the process. However, there are not much works studying crucible design and coil design. Furthermore, depending upon the power values and frequencies used, the influence of the number and width of slits may affect differently to the efficiency.

It is clear that investment casting is the most usual casting process to melt titanium alloys. However, an efficient and cheap material for shell mould is not available. A great deal of attention has been focused on the influence of investment materials. Different casting technologies for the production of thin walled titanium alloy castings have been investigated, and experimental results demonstrate that it is rare for the titanium alloy melt to fill the thin walled cavities only with the help of gravity. In the casting of thin and complex sections, centrifugal casting seems necessary, together with a good mould temperature.

It is important to remark that there exist additional parameters affecting the soundness of castings. There are intrinsic parameters of any casting process. An adequate mould design is vital for a good filling of the mould, and the filling time (or cooling rate) decides the microstructure of the final product, and hence, its mechanical properties.

CHAPTER 4

# MATHEMATICAL FORMULATION OF THE PROBLEM

This chapter discusses the theory for the numerical modelling of magnetohydrodynamics. After describing a general approach to magnetohydrodynamic problems, the governing equations and boundary conditions of electromagnetic, heat transfer, and fluid mechanics fields are depicted and the coupling conditions explained. Finally, the main conclusions are presented.

## 4.1 Approach to magnetohydrodynamics

In the early 19th century, Faraday and his contemporaries were aware of the interaction between a magnetic field and an object moving through it. They knew that if an electrically conducting solid object or a fluid moves through a magnetic field, the generated magnetic field induced currents in the fluid or solid object. Hannes Alfvén introduced the magnetohydrodynamics (MHD) term in 1942 (Widlund 2000).

At the beginning, alternating currents (AC) magnetic fields were only used for heating and melting electrically conducting materials. However, magnetic fields are capable of achieving many other effects. Nowadays, alternating magnetic fields are commonly used in the metal industry to impart thermal and mechanical energies to a liquid metal. AC magnetic fields may be used to shape, to levitate, or to stir a fluid. Also for controlling the solidification of a metallic alloy. The various applications of electromagnetism presently in use in the metals industry include: CCIM, electromagnetic casting, induction stirring, levitation melting, induction melting, electromagnetic shaping, and electromagnetic braking (Yasuda 2007).

Several physical effects occur in MHD. When a liquid metal is subject to an AC magnetic field, eddy currents are induced in the metal, which is heated by resistive heating. Moreover, the induced eddy currents interact with the external magnetic field, creating Lorentz forces in the molten metal. These

forces originate a fluid flow by stirring and also modify the geometry of the surface of the molten metal. In addition, the currents induce a new magnetic field, which distorts the original field. The magnetic field at the boundary of the liquid metal can be viewed as a superposition of the external field supplied by the fixed AC coil with an oppositely directed field generated by the induced currents in the metal. These changes in the magnetic field make the problem highly non-linear.

In case of CCIM, when the metal is being melted, the magnetic confining force pushes the liquid radially inwards to the symmetry axis and upwards until a balance with gravity force is reached. With the inertial effects, this can lead to an oscillating interface motion and waves may appear, where the damping of the fluid depends on the effective turbulent viscosity.

In order to develop a suitable numerical model for CCIM, the fundamental laws of MHD have to be understood. The laws of magnetism and fluid flow are hardly a 20$^{th}$ century innovation, since MHD became a developed subject only in late 1930s. The development of MHD in engineering was slower and did not really become popular until 1960s.

## 4.2 Governing equations: partial differential equations and boundary conditions

In CCIM, the governing equations must represent several coupled phenomena: the electromagnetic interaction between the induction coil, the crucible, and the conducting metal charge within it, the turbulent fluid flow in the melt, the heat transfer, and the phase change. The additional challenge concerns the time dependent variation in the melt geometry.

### 4.2.1 Electromagnetic - Time and frequency domain

The problem of electromagnetic analysis on a macroscopic level is governed by Maxwell's equations subject to certain boundary conditions. Maxwell's equations are a set of first order partial differential equations establishing the relationships between the fundamental electromagnetic quantities:

- electric field intensity **E**,
- electric displacement or electric flux density **D**,
- magnetic field intensity **H**,
- magnetic flux density **B**,
- electric current density **J**, and
- electric charge density $\rho_e$.

The equations can be formulated in differential or integral form. The differential form is presented here because it leads to differential equations that the finite element method can handle. For general time-varying fields, Maxwell's equations can be written as:

$$\nabla \times \mathbf{H} = \mathbf{J} + \frac{\partial \mathbf{D}}{\partial t}, \tag{4.1}$$

$$\nabla \times \mathbf{E} = -\frac{\partial \mathbf{B}}{\partial t}, \tag{4.2}$$

$$\nabla \cdot \mathbf{B} = 0, \tag{4.3}$$

$$\nabla \cdot \mathbf{D} = \rho_e. \tag{4.4}$$

The first two equations are Maxwell-Ampère's law and Faraday's law, respectively. Equations (4.3) and (4.4) are two forms of Gauss' law: the electric and magnetic form, respectively.

Maxwell's equations can be written both in time and frequency domain. When the time variation is harmonic, the mathematical analysis of the Maxwell's equations can be analyzed in the Fourier's domain. In case of CCIM, it is interesting the use of frequency domain because alternating quantities are usually specified or measured in effective values.

Hence, Maxwell's equations in frequency domain may be rewritten after Fourier transformation as:

$$\nabla \times \mathbf{H} = \mathbf{J} + j\omega_f \mathbf{D}, \tag{4.5}$$

$$\nabla \times \mathbf{E} = -j\omega_f \mathbf{B}, \tag{4.6}$$

$$\nabla \cdot \mathbf{B} = 0, \tag{4.7}$$

$$\nabla \cdot \mathbf{D} = \rho_e, \tag{4.8}$$

where $j$ is the imaginary unit and $\omega_f = 2\pi f$, being $f$ the AC frequency.

In the numerical models developed in Chapter 5, the electromagnetic field is solved in frequency domain, meanwhile both the heat transfer and fluid dynamics are solved in time domain. This approach is extensively used in the literature (Lavers 2008).

In addition, Ohm's law states that:

$$\mathbf{J} = \sigma(\mathbf{E} + \mathbf{u} \times \mathbf{B}) + \mathbf{J_e}, \tag{4.9}$$

where $\mathbf{u}$ is the fluid velocity, $\sigma$ is the electrical conductivity, and $\mathbf{J_e}$ is the external current density.

The constitutive equations that describe the macroscopic properties of the medium are described as:

$$\mathbf{D} = \varepsilon_r \varepsilon_0 \mathbf{E} + \mathbf{P}, \tag{4.10}$$

$$\mathbf{B} = \mu_r \mu_0 (\mathbf{H} + \mathbf{M}), \tag{4.11}$$

where $\varepsilon_0$ is the permittivity of vacuum, $\varepsilon_r$ is the relative permittivity, $\mu_0$ is the permeability of vacuum, $\mu_r$ is the relative permeability, **P** is the electric polarization vector, and **M** is the magnetization vector. In the international system, the permeability of vacuum is $4\pi \cdot 10^{-7}$ H/m and the permittivity of vacuum is $8.85 \cdot 10^{-12}$ F/m.

The electric polarization vector **P** describes how the material is polarized when an electric field **E** is present. It can be interpreted as the volume density of electric dipole moments. **P** is generally a function of **E**. Some materials can have a nonzero **P** also when there is no electric field present. The magnetization vector **M** similarly describes how the material is magnetized when a magnetic field **H** is present. It can be interpreted as the volume density of magnetic dipole moments. **M** is generally a function of **H**. Permanent magnets, for instance, have a nonzero **M** also when there is no magnetic field present.

A full Maxwell's system can be simplified for magnetohydrodynamic (MHD) applications (Davidson 2001). Assuming that liquid metal is a non-magnetic material with large electrical conductivity (displacement currents are negligible by the comparison with the current density **J**), and accumulation of the electrical charge does not occur in the medium, simplifying Maxwell's equations to:

$$\nabla \times \mathbf{H} = \mathbf{J}, \tag{4.12}$$

$$\nabla \times \mathbf{E} = -j\omega_f \mathbf{B}, \tag{4.13}$$

$$\nabla \cdot \mathbf{B} = 0, \tag{4.14}$$

$$\nabla \cdot \mathbf{D} = 0. \tag{4.15}$$

In order to solve these equations, it is sometimes helpful to formulate the problems in terms of a magnetic vector potential **A**. The defining equation for the magnetic vector potential is a direct consequence of the magnetic Gauss' law:

$$\mathbf{B} = \nabla \times \mathbf{A}. \tag{4.16}$$

Combining Ohm's law (4.9), Maxwell-Ampere's law (4.12), and Faraday's law (4.13), together with (4.16):

$$(j\omega_f \sigma - \omega_f^2 \varepsilon_0 \varepsilon_r)\mathbf{A} + \nabla \times \left(\mu_0^{-1} \mu_r^{-1} \nabla \times \mathbf{A} - \mathbf{M}\right) - \sigma \mathbf{u} \times \left(\nabla \times \mathbf{A}\right) = \mathbf{J_e}. \tag{4.17}$$

The induced current density and the corresponding induction heat in the molten metal are calculated using magnetic vector potential.

The action of the electromagnetic field to the conducting medium has as a consequence the heating of the fluid and the generation of electromagnetic forces in the fluid. The magnetic force can be rewritten as:

$$\mathbf{F} = \mathbf{J} \times \mathbf{B} . \tag{4.18}$$

Magnetohydrodynamic Ampere's law yields to:

$$\nabla \times \mathbf{B} = \mu_r \mu_0 \mathbf{J} . \tag{4.19}$$

Replacing equation (4.19) into equation (4.18):

$$\mathbf{F} = \frac{\nabla \times \mathbf{B}}{\mu_r \mu_0} \times \mathbf{B} = -\nabla\left(\frac{1}{2\mu_r \mu_0}\mathbf{B}\cdot\mathbf{B}\right) + \left(\frac{1}{\mu_r \mu_0}\mathbf{B}\cdot\nabla\right)\mathbf{B} = -\nabla\left(\frac{\mathbf{B}^2}{2\mu_r \mu_0}\right) + \frac{1}{\mu_r \mu_0}(\mathbf{B}\cdot\nabla)\mathbf{B} . \tag{4.20}$$

The first term of the right hand side is the irrotational part ($-\nabla(\mathbf{B}^2/2\mu_r\mu_0)$), which leads to the development of a convex meniscus on the molten metal. This irrotational part is called electromagnetic pressure, and only affects to the free surface of the melt. The second term is the rotational part ($1/\mu_r\mu_0 \cdot (\mathbf{B}\cdot\nabla)\mathbf{B}$), which generates the stirring in the melt.

The action of the electromagnetic field has another consequence in the fluid: the temperature rise of the body due to the Joule heating. The resistive heating (ohmic heating) due to the electric current is:

$$Q = \frac{\mathbf{J}^2}{\sigma}, \tag{4.21}$$

where **J** is the electric current density and $\sigma$ is the conductivity of the fluid.

To solve all these equations, boundary conditions are necessary. The magnetic insulation has been used in all outer surfaces as boundary condition in the electromagnetic field:

$$\mathbf{n} \times \mathbf{A} = 0 , \tag{4.22}$$

where **n** is the direction of the normal vector and **A** is the magnetic vector potential.

The magnetic insulation boundary condition sets that the tangential components of the magnetic potential have to be zero at the boundary.

At interfaces between two media, the boundary conditions can be expressed mathematically as:

$$\mathbf{n}_2 \cdot (\mathbf{J}_1 - \mathbf{J}_2) = -j\omega_f \rho_s \,, \tag{4.23}$$

where $\rho_s$ denotes the surface charge density, $\mathbf{J}_1$ and $\mathbf{J}_2$ are the electric current density of the medium 1 and 2 respectively, and $\mathbf{n_2}$ is the outward normal vector from medium 2.

An important theoretical concept in electromagnetism is the skin depth ($\delta$). According to the value of the frequency of the applied electric current as well as the electrical conductivity of the materials, the induced electric current density does not penetrate deeply into the materials (Fautrelle 2009). The induced current is limited to a "skin" layer. The width of this skin layer is:

$$\delta = \sqrt{\frac{\sigma}{\pi \mu_r \mu_0 f}} \,, \tag{4.24}$$

where $\sigma$ is the electrical conductivity of the melt, $\mu_r$ is the relative magnetic permeability of the melt, $\mu_0$ is the magnetic permeability of vacuum, and $f$ is the operating frequency. Approximately 86% (1-1/e$^2$) of the energy transferred by the induction coil is deposited in the skin depth.

### 4.2.2 Heat transfer - Time domain

The fundamental law governing all heat transfer is the first law of thermodynamics, commonly referred to as the principle of conservation of energy. However, internal energy $U_e$ is a rather inconvenient quantity to measure and use in simulations. Therefore, the basic law is usually rewritten in terms of temperature, $T$. For a fluid, the resulting heat equation is (COMSOL 2013):

$$\rho C_p \left( \frac{\partial T}{\partial t} + (\mathbf{u} \cdot \nabla) T \right) = -(\nabla \cdot \mathbf{q}) + \boldsymbol{\tau} : \mathbf{S} - \frac{T}{\rho} \frac{\partial \rho}{\partial T}\bigg|_p \left( \frac{\partial p}{\partial t} + (\mathbf{u} \cdot \nabla) p \right) + Q \,, \tag{4.25}$$

where $\rho$ is the density, $C_p$ is the specific heat capacity at constant pressure, $T$ is absolute temperature, $\mathbf{u}$ is the velocity vector, $\mathbf{q}$ is the heat flux by conduction, $p$ is the pressure, $\boldsymbol{\tau}$ is the viscous stress tensor, $\mathbf{S}$ is the strain-rate tensor, and $Q$ contains heat sources other than viscous heating.

The conductive heat flux $\mathbf{q}$ is proportional to the temperature according to Fourier's law of heat conduction:

$$\mathbf{q} = -k_t \nabla T \,, \tag{4.26}$$

where $k_t$ is thermal conductivity.

In CCIM problem, the viscous heating and pressure work (second and third term of the equation (4.25)) are ignored. Substituting equation (4.26) into equation (4.25), we obtain:

$$\rho C_p \frac{\partial T}{\partial t} + \rho C_p \mathbf{u} \cdot \nabla T = \nabla \cdot (k_t \nabla T) + Q. \tag{4.27}$$

In contrast to electromagnetism, the heat transfer equation (4.27) is solved in time domain and is only analysed in the charge.

In the solid walls, we use the specified temperature boundary condition:

$$T = T_0, \tag{4.28}$$

where $T_0$ is the prescribed temperature on the boundary. The temperature is equal to the crystallization temperature of the molten material. In the case of titanium, the temperature will be 1600ºC.

In free surface, a radiation boundary condition has been used. The net inward heat flux from surface-to-ambient radiation is

$$q = e\sigma_B \left(T_{amb}^4 - T^4\right), \tag{4.29}$$

where $e$ is the surface emissivity, $\sigma_B$ is the Stefan-Boltzmann constant, and $T_{amb}$ is the ambient temperature.

In some three dimensional numerical models, due to the azimuthal periodicity of the problem around the vertical axis, it is possible to study only one sector of the real problem. In this case, a periodic condition has been used in the sides:

$$-\mathbf{n}_{dst} \cdot \left(k_t \nabla T\right)_{dst} = \mathbf{n}_{src} \cdot \left(k_t \nabla T\right)_{src}, \tag{4.30}$$

$$T_{dst} = T_{src}, \tag{4.31}$$

where **n** is direction of the normal vector and *dst* and *src* are the destination and source boundaries respectively. Equations (4.30) and (4.31) impose that the heat fluxes and temperatures in both sides are equals.

### 4.2.3 Navier-Stokes equations - Time domain

In MHD problems, the Lorentz forces generate a movement in the fluid. This movement may be laminar or turbulent. Reynolds number ($R_e$) measures the tendency of a laminar flow to become turbulent:

$$R_e = \frac{\rho U L}{\mu}, \tag{4.32}$$

where $L$ is the radius of the crucible, $\mu$ is the dynamic viscosity of the fluid, $\rho$ is the density of the fluid, and $U$ is the mean value velocity.

$R_e$ represents the ratio between inertial and viscous forces. At low $R_e$, viscous forces dominate and tend to reduces all disturbances, which lead to laminar flow. At high $R_e$, the damping in the system is very low, giving small disturbances the possibility to grow by nonlinear interactions. If the $R_e$ is high enough, the fluid flow field eventually ends up in a chaotic state called turbulence. Turbulence is a property of the flow field and it is mainly characterized by a wide range of flow scales: the largest occurring scales, depending upon the geometry, the smallest quickly fluctuating scales, and the scales between them.

One of the problems to calculate $R_e$ is the estimation on the mean value velocity $U$. Barbier *et al.* (Delage 1984) showed that the mean value velocity $U$ in the liquid metal is about a 10 to 20% of the Alfvén velocity ($U_A$), defined as:

$$U_A = \frac{B_{eff}}{(\mu_0 \rho)^{1/2}}, \tag{4.33}$$

where $B_{eff}$ is the magnetic field strength, $\mu_0$ is the magnetic permeability of vacuum, and $\rho$ is the density of the fluid.

If the Reynolds number achieves large values, the fluid flow becomes turbulent. In case of CCIM, the flow intensity can achieve several meters per second due to the large intensity of the electromagnetic field, which corresponds to Reynolds numbers greater than $10^4$. Therefore, liquid metal flows in induction furnaces are usually turbulent. These electromagnetically driven turbulent flows occur in a large variety of industrial applications such as continuous casting, liquid metal treatment stirring, aluminium electrolysis, induction melting, and magnetically stabilize crystal growth (Yasuda 2007, Fautrelle 2009).

Turbulence consists of a continuous spectrum of scales or vortices ranging from largest to smallest. These turbulent flow vortices receive energy from the macroscopic flow, participating in the energy transfer with ever decreasing vortices, which is called the spectral energy transfer (Baake 2007). In order to visualize a turbulent flow with a spectrum of scales, turbulent eddies are defined. A turbulent eddy can be thought of as a local swirling motion whose characteristic dimension is the local turbulence scale. Turbulence is composed of eddies of different sizes. The large eddies are unstable and break up, transferring their energy to smaller eddies. Turbulent flows contain eddies with a range of length and time scales that interact in a dynamically complex way. The kinetic energy is transferred from the largest eddies to the smallest ones. Ultimately, the smallest eddies dissipate into heat through the action of molecular viscosity.

The turbulence can introduce positive or negative effects into the melting process depending on the desired properties of the final product and construction of melting equipment. Turbulence can improve quality of the final alloy with the effective melt mixing and temperature homogenization. However, the

turbulence is often a reason for the rigorous crucible erosion. Moreover, the turbulent melt flow generates free surface instabilities, which means surface waves or oscillations that can introduce air bubbles into the melt.

Historically, the first turbulence study was performed by Reynolds in the end of the 19th century, but until now, the complete description of the turbulence is a fundamental unsolved problem of physics. The general theory of turbulence, which can provide analytical or exact solution of the problems, is not built yet. Numerous attempts to simulate the liquid metal flow in a cylindrical induction furnace both experimentally and numerically have been performed in the last decades.

Hence, we can define the movement of a fluid as laminar or turbulent.

- Laminar flow

Navier-Stokes equations describe the motion of any fluid. When the velocities of these flows are too small, the fluid retain an ordered layered structure. In these rare cases, the flows are considered laminar and the dynamic turbulent is constant. Hence, the Navier-Stokes equations for incompressible and Newtonian fluids are:

$$\rho \nabla \cdot \mathbf{u} = 0\,, \tag{4.34}$$

x-momentum
$$\frac{\partial(\rho u_x)}{\partial t} + \nabla \cdot (\rho u_x \mathbf{u}) = -\frac{\partial p}{\partial x} + \nabla \cdot (\mu \nabla u_x) + F_x\,, \tag{4.35}$$

y-momentum
$$\frac{\partial(\rho u_y)}{\partial t} + \nabla \cdot (\rho u_y \mathbf{u}) = -\frac{\partial p}{\partial y} + \nabla \cdot (\mu \nabla u_y) + F_y\,, \tag{4.36}$$

z-momentum
$$\frac{\partial(\rho u_z)}{\partial t} + \nabla \cdot (\rho u_z \mathbf{u}) = -\frac{\partial p}{\partial z} + \nabla \cdot (\mu \nabla u_z) + F_z\,, \tag{4.37}$$

where $\mathbf{u}$ is the fluid velocity, $u_x$ is the fluid velocity in $x$ direction, $u_y$ is the fluid velocity in $y$ direction, $u_z$ is the fluid velocity in $z$ direction, $\rho$ is the density of the fluid, $p$ is the pressure, $\mu$ is the dynamic viscosity, $F_x$ is external forces in $x$ direction, $F_y$ is external forces in $y$ direction, and $F_z$ is external forces in the $z$ direction.

Equation (4.34) is the continuity equation. In general form, the momentum equation is:

$$\rho \frac{\partial \mathbf{u}}{\partial t} + \rho \mathbf{u} \cdot \nabla \mathbf{u} = -\nabla p + \nabla \cdot \left[\mu\left(\nabla \mathbf{u} + (\nabla \mathbf{u})^T\right)\right] + \mathbf{F}\,. \tag{4.38}$$

These equations are calculated from the conservation laws of mass and momentum. The development of these equations can be found in (Versteeg 2007).

- Turbulent flow

When the $R_e$ exceeds a critical value, the fluid structure becomes increasingly perturbed by developing internal non-stabilities, whose energy is not dissipated into heat to a sufficient degree. The fluid flow becomes turbulent.

In principle, the time dependent three dimensional Navier-Stokes equation contains all of the physics of a given turbulent flow. Nevertheless, the smallest scales of turbulence are still extremely small. They are generally many orders of magnitude smaller than the largest scales of turbulence. Unfortunately, to make an accurate numerical simulation of a turbulent flow, all physically relevant scales must be resolved (Wilcox 1998).

Numerical experiments have shown that in some industrial engineering applications, a sufficient precision in calculations of the averaged flow velocities can be achieved even when assuming that the dynamic turbulent viscosity ($\mu_T$) is constant. An advantage of this approach is that the equation to be solved is precisely the same as in the case of a laminar flow (equations (4.34)-(4.37)), where the effective viscosity $\mu_{eff}$ ($\mu_{eff} = \mu + \mu_T$) should be taken to be 2-3 orders of magnitude greater than $\mu$ in order to take into account the additional turbulent dissipation. Its disadvantage is the inadequate description of dissipation in some regions of the flow, *e.g.* near the wall or in the zones with low intensity of the flow.

Hence, since in many practical problems the application of the constant turbulent viscosity gives results differing from experimental ones, a whole pallet of empirical and semi-empirical turbulence models have been developed. The transient nature of turbulent processes and three dimensional (3D) representation of the flow introduce particular difficulties for turbulence study. Computer methods for solving the differential equations of fluid dynamic are well advanced. However, there are no computer models of large turbulent flows because the necessary computer storage exceeds by many orders of magnitude what is currently available.

To overcome the problem, turbulence models have been invented. These consist of differential equations and associated algebraic equations and constants that in conjunctions the Navier-Stokes equations, closely simulate the behaviours of real turbulent fluids (Launder 1974).

The methods to solve turbulence can be grouped into the following three categories:

- Reynolds averaged Navier-Stokes (RANS).
- Large eddy simulation (LES).
- Direct numerical simulation (DNS).

4.2.3.1 Turbulence models for Reynolds averaged Navier-Stokes (RANS) equations

In order to analyse turbulent flows, its velocity is most often divided into several summands, using a filtering procedure (Baake 2007). The velocity of the flow (Figure 4.1) is decomposed into a steady mean value $U_x$ with a fluctuating component $u_x'(t)$ superimposed on it: $u_x(t) = U_x + u_x'(t)$. This is called the Reynolds decomposition.

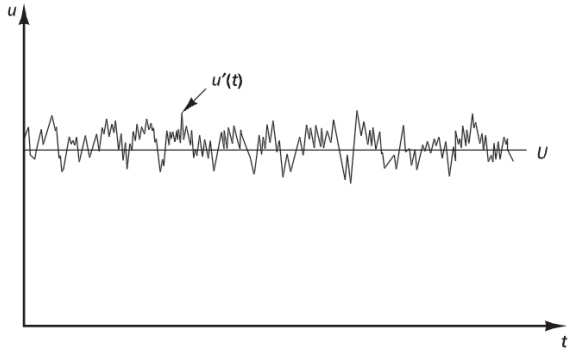


Figure 4.1. Typical point velocity measurement in turbulent flow (Versteeg 2007).

A turbulent flow can now be characterised in terms of the mean values of flow properties ($U_x$, $U_y$, $U_z$, and $P$) and some statistical properties of their fluctuations ($u_x'$, $u_y'$, $u_z'$, and $p'$) (Versteeg 2007). Thus, using the Reynolds decomposition and replacing the flow variables **u** (hence $u_x$, $u_y$, and $u_z$) and $p$ by the sum of a mean and fluctuating component:

$$\mathbf{u} = \mathbf{U} + \mathbf{u'}, \tag{4.39}$$

$$u_x = U_x + u_x', \tag{4.40}$$

$$u_y = U_y + u_y', \tag{4.41}$$

$$u_z = U_z + u_z', \tag{4.42}$$

$$p = P + p'. \tag{4.43}$$

Replacing equations (4.40)-(4.43) in the Navier-Stokes equations (4.34)-(4.37) and developing these equations:

$$\rho \nabla \cdot \mathbf{U} = 0, \tag{4.44}$$

$$\frac{\partial(\rho U_x)}{\partial t} + \nabla \cdot (\rho U_x \mathbf{U}) + \left[ \frac{\partial(\overline{\rho u_x'^2})}{\partial x} + \frac{\partial(\overline{\rho u_x' u_y'})}{\partial y} + \frac{\partial(\overline{\rho u_x' u_z'})}{\partial z} \right] = -\frac{\partial p}{\partial x} + \nabla \cdot (\mu \nabla U_x) + F_x, \tag{4.45}$$

$$\frac{\partial(\rho U_y)}{\partial t}+\nabla\cdot(\rho U_y\mathbf{U})+\left[\frac{\partial(\overline{\rho u_x' u_y'})}{\partial x}+\frac{\partial(\overline{\rho u_y'^2})}{\partial y}+\frac{\partial(\overline{\rho u_y' u_z'})}{\partial z}\right]=-\frac{\partial p}{\partial y}+\nabla\cdot(\mu\nabla U_y)+F_y, \quad (4.46)$$

$$\frac{\partial(\rho U_z)}{\partial t}+\nabla\cdot(\rho U_z\mathbf{U})+\left[\frac{\partial(\overline{\rho u_x' u_z'})}{\partial x}+\frac{\partial(\overline{\rho u_x' u_y'})}{\partial y}+\frac{\partial(\overline{\rho u_z'^2})}{\partial z}\right]=-\frac{\partial p}{\partial z}+\nabla\cdot(\mu\nabla U_z)+F_x. \quad (4.47)$$

The equation set (4.44)-(4.47) is called the Reynolds-averaged Navier–Stokes equations (Versteeg 2007). In a general form, we obtain:

$$\rho\nabla\cdot\mathbf{U}=0, \quad (4.48)$$

$$\rho\frac{\partial\mathbf{U}}{\partial t}+\rho\mathbf{U}\cdot\nabla\mathbf{U}+\nabla\left(\overline{p\mathbf{u}'\otimes\mathbf{u}'}\right)=-\nabla P+\nabla\cdot\left[\mu\left(\nabla\mathbf{U}+(\nabla\mathbf{U})^T\right)\right]+\mathbf{F}, \quad (4.49)$$

where **U** is the averaged velocity field and $\otimes$ is the outer vector product.

Comparing equations (4.45)-(4.47) and (4.49) in relation to the analogous equations of laminar flow, the only difference is the appearance of the last term on the left hand side of these equations. This term represents the interaction between the fluctuating velocities and is called the Reynolds stress tensor.

These extra terms are modelled with different classical turbulence models. Since these models and especially empirical constants contained in them were mostly used for a narrow range of problems, at the current stage of their development they can be classified as follows:

- Algebraic or zero equation models,
- One equation models, and
- Two equation models.

The computing resources required for a reasonably accurate flow computation are modest, so this approach has been the mainstay of engineering flow calculations over the last three decades.

*4.2.3.1.1 Algebraic or zero equation model*

The earliest attempt at developing a mathematical description of turbulent stresses was made by Boussinesq, when he introduced the concept of eddy viscosity. Prandtl, introduced the mixing length and a straightforward prescription for computing the eddy viscosity in terms of the mixing length. Algebraic turbulence models do not require the solution of any additional equations, and are calculated directly from the flow variables. As a consequence, zero equation models may not be able to properly account for history effects on the turbulence, such as convection and diffusion of turbulent energy. A mixing length model is an algebraic turbulence model.

*4.2.3.1.2 One equation models*

To improve the ability to predict properties of turbulent flows and to develop a more realistic mathematical description of the turbulent stresses, Prandtl postulated a model in which the eddy viscosity depends upon the kinetic energy of turbulent fluctuations, *k*. He proposed a modelled differential equation approximating the exact equation for *k*. This improvement, on a conceptual level, takes into account that the eddy viscosity is affected by the previous location of the flow.

*4.2.3.1.3 Two equation models*

While having an eddy viscosity that depends upon flow history provides a more physically realistic model, the need to specify a turbulence length scale remains. Since the length scale can be thought of as a characteristic eddy size and since such scales are different for each flow, turbulence models that do not provide a length scale are incomplete (Wilcox 1998).

Kolmogorov introduced the first complete model of turbulence. In addition to having a modelled equation for *k*, he introduced a second parameter $\omega$, which is the rate of dissipation of energy in unit volume and time. The reciprocal of $\omega$ serves as turbulence time scale, while $k^{1/2}/\omega$ serves as the analogue of the mixing length. In this model, known as $k$-$\omega$ model, $\omega$ satisfies a differential equation similar to the equation *k*. The model is thus termed a "two equation model of turbulence". While this model offered great promise, it went with virtually no applications for the next quarter century because of the unavailability of computers to solve its nonlinear differential equations.

Launder's $k$-$\varepsilon$ model, where $\varepsilon$ is proportional to the product of *k* and $\omega$, is as well-known as the mixing-length model, and it is the most widely used two-equation model. In the 80-90s, versatile modifications of this model were developed in order to adapt to diverse practical situations, from which the following could be mentioned:

- Small Reynolds number model, which modifies the calculations of turbulent viscosity in the regions with relatively lower flow intensity.

- Renormalization group (RNG) model, which accounts more precisely for general features of chaotic processes and better describes the transport processes in rotating flows and the cases of multiple vortices;

- Momentum models of the 2nd and higher orders. These are mainly designed for flows with an expressed turbulence anisotropy which cannot in principle be described by $k$-$\varepsilon$ type models.

4.2.3.2 Large eddy simulation (LES)

In case of large eddy simulation, the velocity of the flow is not decomposed into a steady mean value with fluctuating components. The large eddies of the turbulence are resolved and the smallest eddies are modelled. The underlying premise is that the largest eddies are directly affected by the boundary

conditions and must be computed. By contrast, the small scale turbulence is more nearly isotropic and has universal characteristic.

The method involves space filtering of the unsteady Navier-Stokes equations prior to the computations, which passes the largest eddies and rejects the smallest ones. The large scale turbulent flow is computed directly with time-dependent simulation and the influence of the small scales is taken into account by appropriate subgrid scale models.

4.2.3.3 Direct numerical simulation (DNS)

In direct numerical simulations, the unsteady Navier-Stokes equations are solved on spatial grids that are sufficiently fine to resolve the Kolmogorov length scales at which energy dissipation takes place and with time steps sufficiently small to resolve the period of the fastest fluctuations. These calculations are costly in terms of computing resources, so the method is not used for industrial flow computations.

An extensive catalogue of turbulence models and detailed explanations of each model can be found in the literature (Wilcox 1998, Versteeg 2007).

In CCIM, the flow is highly turbulent. In the numerical models developed in Chapter 5, Wilcox revised $k$-$\omega$ RANS model has been used to solve the Reynolds stresses (Wilcox 1998). Navier-Stokes equations are solved in time domain. Hence, for an incompressible and Newtonian fluid

$$\nabla \cdot (\rho \mathbf{u}) = 0, \tag{4.50}$$

$$\rho \frac{\partial \mathbf{u}}{\partial t} + \rho \mathbf{u} \cdot \nabla \mathbf{u} = -\nabla p + \nabla \cdot \left[ (\mu + \mu_T)\left(\nabla \mathbf{u} + (\nabla \mathbf{u})^T\right)\right] + \frac{2}{3}\rho k \mathbf{I} + \mathbf{F}, \tag{4.51}$$

$$\rho C_p \frac{\partial T}{\partial t} + \rho C_p \mathbf{u} \cdot \nabla T = \nabla \cdot ((k_t + k_T)\nabla T) + Q, \tag{4.52}$$

where $\mathbf{u}$ is the fluid velocity, $\rho$ is the density of the fluid, $p$ is the pressure, $\mu$ is the dynamic viscosity, $\mu_T$ is the dynamic turbulent viscosity, $k$ is the turbulent kinetic energy, $\mathbf{F}$ is the external forces, $C_p$ is the specific heat capacity at constant pressure, $T$ is absolute temperature, $k_t$ is the thermal conductivity, $k_T$ is thermal turbulent conductivity, and $Q$ contains heat sources other than viscous heating. $k_T$ is defined as:

$$k_T = \mu_T \frac{C_p}{Pr_T}, \tag{4.53}$$

where $Pr_T$ is turbulent Prandtl number.

Equations (4.50), (4.51), and (4.52) are the laws of conservation of mass, conservation of momentum, and conservation of energy, respectively.

The Wilcox revised *k*-$\omega$ RANS model introduces two additional transport equations and two dependent variables: the turbulent kinetic energy *k*, and specific dissipation rate, $\omega$.

$$\rho\frac{\partial k}{\partial t}+\rho\mathbf{u}\cdot\nabla k=P_k-\rho\beta^*k\omega+\nabla\cdot\left(\left(\mu+\sigma^*\mu_T\right)\nabla k\right), \tag{4.54}$$

$$\rho\frac{\partial \omega}{\partial t}+\rho\mathbf{u}\cdot\nabla \omega=\alpha\frac{\omega}{k}P_k-\rho\beta\omega^2+\nabla\cdot\left(\left(\mu+\sigma_1^*\mu_T\right)\nabla \omega\right). \tag{4.55}$$

The turbulent viscosity, the production term, and the different model constants are defined as:

$$\mu_T=\rho\frac{k}{\omega}, \tag{4.56}$$

$$P_k=\mu_T\left[\nabla\mathbf{u}:\left(\nabla\mathbf{u}+(\nabla\mathbf{u})^T\right)\right], \tag{4.57}$$

$$\alpha=\frac{13}{25},\qquad \beta_0=\frac{9}{125},\qquad \beta_0^*=\frac{9}{100},\qquad \sigma^*=\frac{1}{2},\qquad \sigma_1^*=\frac{1}{2}. \tag{4.58}$$

The development of these equations can be found in (Wilcox 1998).

In turbulent flows, close to solid wall, there are inevitably regions where the local Reynolds number of turbulence is so small that viscous effects predominate over turbulent ones. There are two methods to account for these regions in numerical methods when computing turbulent flow: the wall function method and the low Reynolds number modelling method (Launder 1974). The wall function method is the one which has been most widely used for many practical purposes.

In solid walls, we use the wall condition:

$$\mathbf{u}\cdot\mathbf{n}=0, \tag{4.59}$$

$$\left[\left(\mu+\mu_T\right)\left(\nabla\mathbf{u}+(\nabla\mathbf{u})^T\right)-\frac{2}{3}\rho k\mathbf{I}\right]\mathbf{n}=-\rho\frac{u_\tau}{\delta_w^+}\mathbf{u}_{\mathbf{tang}}, \tag{4.60}$$

$$\mathbf{u}_{\mathbf{tang}}=\mathbf{u}-(\mathbf{u}\cdot\mathbf{n})\mathbf{n}, \tag{4.61}$$

$$\nabla k\cdot\mathbf{n}=\mathbf{0}, \tag{4.62}$$

$$\omega=\rho\frac{k}{k_v\delta_w^+\mu}, \tag{4.63}$$

where $u_\tau$ is the friction velocity, $k_v$ is is the von Kárman constant, and $\delta_w^+$ is the distance from the wall to the computational domain.

In free surface, we use the following open boundary conditions:

$$\left[-p\mathbf{I}+(\mu+\mu_T)\left(\nabla\mathbf{u}+(\nabla\mathbf{u})^T\right)-\frac{2}{3}\rho k\mathbf{I}\right]\mathbf{n}=-f_0\mathbf{n}, \tag{4.64}$$

$$\nabla k\cdot\mathbf{n}=0 \qquad \nabla\omega\cdot\mathbf{n}=0 \qquad \text{if } \mathbf{u}\cdot\mathbf{n}\geq 0, \tag{4.65}$$

$$k=\frac{3}{2}\left(U_{ref}I_T\right)^2 \quad \omega=\frac{k^{1/2}}{\left(\beta_0^*\right)^{1/4}L_T} \quad \text{if } \mathbf{u}\cdot\mathbf{n}<0, \tag{4.66}$$

where $f_0$ is the normal stress of the boundary. $U_{ref,}$ $I_{T,}$ and $L_T$ has been assumed 1, 0.005 m/s, and $L_T$ 0.1m respectively.

In some three dimensional numerical models, it is possible to study only one sector of the real problem due to the azimuthal periodicity of the problem around the vertical axis. In this case, we use the flow periodic condition in the sides:

$$\mathbf{u}_{dst}=\mathbf{u}_{src}, \tag{4.67}$$

$$p_{dst}=p_{src}, \tag{4.68}$$

$$k_{dst}=k_{src}, \tag{4.69}$$

$$\omega_{dst}=\omega_{src}, \tag{4.70}$$

where the subscripts *dst* and *src* are the destination and source boundaries respectively. This boundary condition set that these parameters must have the same values in both boundaries.

The equations of Navier-Stokes are solved in time domain.

## 4.3 Coupling conditions

The characteristics of the melting process in a CCIM are a function of multiple fields and effects that are coupled to produce a quasi-steady state condition. These include electromagnetic, temperature, and hydrodynamics, as well as temperature-dependent material properties such as thermal conductivity, electrical resistivity, specific heat, viscosity, and density. These effects are coupled and interdependent.

The temperature field depends on the behaviour of the energy deposition due to the electromagnetic field. In turn, the characteristics of this energy value depend on the electrical resistivity of the charge. The electrical resistivity can vary by several orders of magnitude within the melt volume due to temperature dependence.

Furthermore, in relation to the heat transfer, properties such as thermal conductivity, specific heat, viscosity, and density are also temperature dependent. In case there is turbulence, the thermal conductivity is related to turbulent viscosity with the Prandtl number. In addition, the heat transfer is significantly affected by the turbulent nature of the fluid flow, the melting front motion, and the associated latent heat.

In the other hand, the electromagnetic field is dependent of the geometry of the charge. The Lorentz forces modify the geometry. This geometrical change affect to the original electromagnetic field, modifying again the Lorentz forces that act in the charge.

Figure 4.2 summarizes all these coupling conditions.

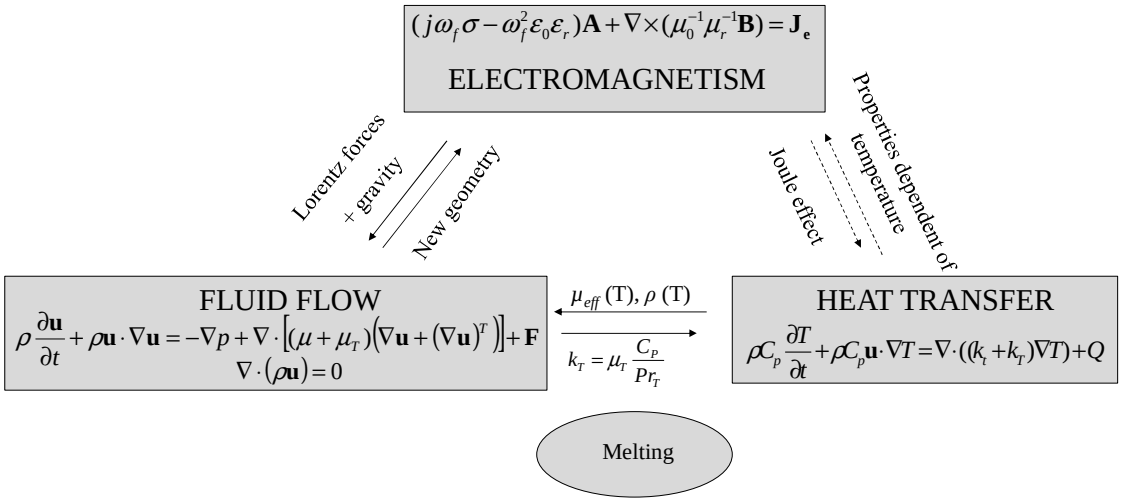


Figure 4.2. Coupling conditions.

## 4.4 Conclusions

The mathematical formulations of electromagnetic field, heat transfer, and fluid flow are well known. The problem can come from the selection of a suitable turbulence model of CCIM. The theoretical formulation when simulating the flows is determined by the problems to be solved, the flow conditions, and the geometry of the melt regions. But the choice of a suitable model and its complexity is limited by the availability of numerical methods, the software, and computational resources. The latter one is especially important for engineering and technical applications, when it is necessary to obtain results as soon as possible.

CHAPTER 5

# NUMERICAL MODELLING

This chapter describes the numerical modelling method developed for CCIM problem. First, we give a literature review of numerical methods used for modelling CCIM and we introduce the one used in our simulations. Then, we explain the assumptions applied for the numerical modelling and we describe both two and three dimensional models. Finally, we detail the advantages and limitations of our simulation methodology.

## 5.1 Numerical modelling (Literature Review)

Induction processes for heating, melting, stirring, and confinement applications have become a subject of numerical modelling. Lavers (Lavers 2008) presented an excellent state of the art of numerical modelling of induction processes. He listed the references in categories that cover a broad range of induction modelling and application issues.

### 5.1.1 Numerical modelling of induction furnaces

Papers describing mathematical models developed for electromagnetically driven flow in induction furnaces appeared in the mid 70s (Tarapore 1976, Tarapore 1977, El Kaddah 1983). The electromagnetic field and the fluid dynamic fields were solved using the mutual inductance and finite difference technique, respectively. These fluid numerical models applied two equation turbulence models. The $k$-$\varepsilon$ model has long served as the basis for turbulent flow calculations in electromagnetically stirred systems. Baake *et al.* (Baake 1995) reported that the calculations of the mean velocity with the aid of the $k$–$\varepsilon$ standard model reveal good quantitative agreement with the experimentally determined values. However, the $k$–$\varepsilon$ model fails to correctly describe the heat and mass transfer processes between the main vortices (Baake 2003b, Baake 2000).

The results of $k$-$\varepsilon$ simulations predict the highest values of turbulent viscosity in the eddy centers and the lowest between the eddies. Such distribution is characteristic for the $k$-$\varepsilon$ model even in the case of 3D

transient simulations. Since the effective thermal conductivity directly depends on the turbulent viscosity, this leads to the underestimation of the heat transfer between the eddies (Baake 2009).

Large Eddy Simulation (LES) numerical technique is an alternative for *k-ε* models. The results of the transient 3D LES simulation of the turbulent melt flows reveal large scale periodic flow instabilities and a homogeneous temperature distribution in the melt, which both are in good agreement with the expectations based on the data from the experiments (Baake 2009, Umbrashko 2006).

LES and *k-ε* approach utilize different turbulence modelling. Therefore, the calculated viscosity distribution behaves differently. The highest values of the LES viscosity are located in the zone of eddies interaction in the near wall region. The turbulent viscosity in the case of LES is one order of magnitude below the one predicted by the *k-ε* model (Figure 5.1) (Baake 2003b).

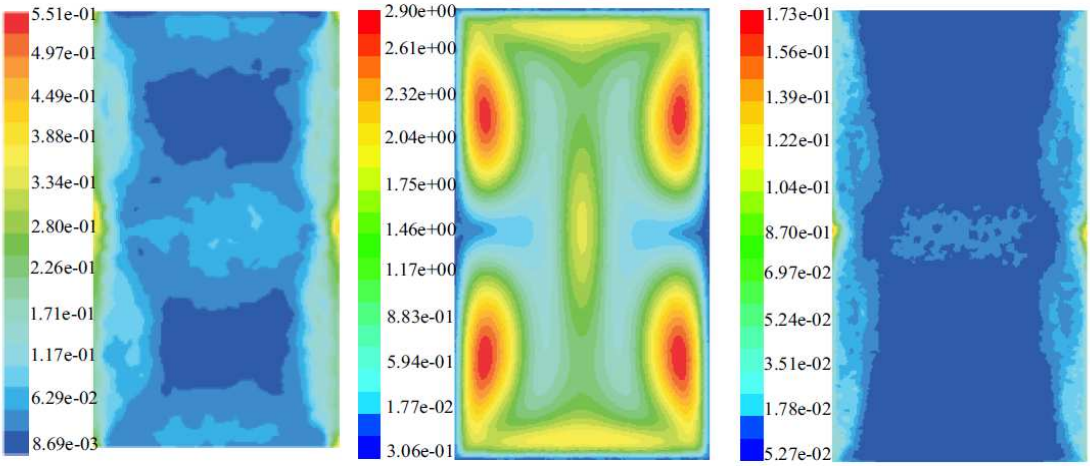


Figure 5.1.Turbulent viscosity distribution (Pa·s) in case of *k-ε* (middle) and LES 3D modelling on mesh with $0.25 \cdot 10^6$ (left) and $3.5 \cdot 10^6$ (right) elements (Umbrashko 2006).

An alternative *k-ω* turbulence model is also shown to be potentially adequate for complex turbulent flows (Bojarevics 1999a). The *k-ω* model accounts for nearly laminar fluid regions where $\mu_T$ is effectively zero, and at the same time, highly intense turbulence is being generated, *e.g.*, in the regions where the rotational body force is applied and at the wall layers (Pericleous 2001). The general flow structure is reproduced well and the local velocities and turbulence intensity levels are in good agreement.

Although the finite difference was the most common numerical method to solve Navier-Stokes equations, nowadays the finite volume method has the broadest applicability (Bakker 2013).

In relation to the electromagnetism, the earliest papers describing the numerical solution of eddy current for induction heating problem were presented in 1963. These papers based on finite difference method to solve the problem (Lavers 2008). Currently, the vast majority of induction applications are modelled using the finite element method (Lavers 2008, Bermudez 2005).

### 5.1.2 Numerical modelling of free surface

It is important to include the actual shape of the molten metal free surface in induction melting modelling. Sneyd and Moffat (Sneyd 1982) provided the first practical model to simulate the free surface meniscus. They developed a "global" method for calculating the free surface shape in electromagnetic levitation, converting the equilibrium boundary condition (without hydrodynamic pressure) into a variational energy principle. Subsequently, similar approaches were developed. Gagnoud *et al.* (Gagnoud 1988) analyzed the shape of the melt in the cold crucible using both a local and a global method. Meanwhile, Onishi and Etay (Onishi 1992) solved the problem using a local method with constant segments. Evans *et al.* (Sakane 1988, Li 1994, Li 1993, Li 1991) simulated the meniscus shape in electromagnetic casting using the mutual inductance method to calculate the electromagnetic field. According to the pressure imbalance, the peripheral surface elements were moved radially inwards or outwards until equilibrium was reached on the boundary. Lavers *et al.* (Lavers 1988a) were the first to use the boundary element technique to calculate the meniscus shape in melting and casting by seeking equilibrium between the electromagnetic and hydrostatic pressures. Bhamidipati *et al.* (Bhamidipati 1991) applied the volume integral method to calculate the electromagnetic field and tackled the free surface shape in the semi levitation induction melting process by displacing the melt boundary in the radial direction. Fukumoto *et al.* (Fukumoto 1991) developed a model using FEM that included the melt flows. Kawase *et al.* (Kawase 1993) used a 3D FEM to obtain the free surface.

### 5.1.3 Numerical modelling of CCIM

Historically, this complex problem has been studied extensively both experimentally and numerically. Delage *et al.* (Delage 1981, Delage 1983) studied electromagnetic and thermal characteristics of a cylindrical crucible. The approach led to the determination of the resistance and the self-inductance equivalent crucible. They ignored the meniscus shape. Gagnoud *et al.* (Gagnoud 1988) studied the magnetic flux density and the shape of the melt in the cold crucible using the distributed system. Tanaka *et al.* (Tanaka 1991) developed a model using the volume element method with an axisymmetric geometry. Bhamidipati *et al.* (Bhamidipati 1991) published a simplified solution of CCIM providing quasi-static solutions that only take into account the irrational magnetic pressure term of the Lorentz force. Gagnoud *et al.* (Gagnoud 1991) developed an early numerical simulation coupling electromagnetism, fluid mechanics, and heat transfer. Bhamidipati *et al.* (Bhamidipati 1992, Bhamidipati 1995) employed a mutual inductance technique to calculate the electromagnetic field and a control volume technique for the temperature and flow fields. Zhu *et al.* (Zhu 1999) developed a CCIM model considering the effect of the melt flow in the free surface shape in 2D. They developed an iterative model to integrate the calculations of electromagnetic field, flow field, and free surface shape.

In recent years, Bojarevics (Bojarevics 1999), Baake (Baake 2007, Umbrashko 2006), and Spitans (Spitans 2013) also performed intensive research in this issue.

Bojarevics *et al.* (Bojarevics 1999) model is based in a continuous coordinate transformation method that maps a deformed boundary to a sphere. The equations and boundary conditions that govern the heat and

Navier-Stokes fields are expressed in spherical coordinates and then transformed to the new coordinates with the appropriate expressions for the derivatives. The transformed equations are solved numerically with a spectral-collections method (Pericleous 1997). The electromagnetic field is numerically solved with a volume integral method. The electromagnetic field force is calculated at each time step (Pericleous 1997). The two equation *k-ω* time-dependent turbulence model is used to compute the effective viscosity and turbulent heat transport. The most significant approximation for the magnetic induction melting is that the problem can be considered as axisymmetric. In reality, three dimensional perturbations are always present, especially with the waves at the free surface. However, in a time average sense, the problem can be approximated by an axisymmetric model (Bojarevics 1999).

Baake *et al.* (Baake 2009) resolve the electromagnetic part of cold crucible with the commercial software ANSYS (ANSYS 2013) using a 3D model representing the half-slit wide sector-cut of the complete geometry. The shape of the free melt surface is calculated using an *in-house* program based on the equilibrium equations between electromagnetic and hydrostatic pressure in the melt. The Navier-Stokes equations are calculated using LES turbulence modelling method in a fixed shape domain (Umbrasko 2008). This model assumes a low magnetic Reynolds number, which allows to split the problem in electromagnetic and hydrodynamic/heat transfer parts and solve them sequentially.

Spitans *el al.* (Spitans 2013) solve the electromagnetic and hydrodynamic parts sequentially. The calculation of free surface dynamics is performed by means of ANSYS Classic (FEM) for the electromagnetic part and ANSYS/CFX (VOF) for the hydrodynamic part and their external coupler. The hydrodynamic analysis uses the VOF numerical technique in combination with *k-ω* turbulence description. For free dynamics calculation, they assumed that for a sufficiently small time interval the change in shape is so insignificant that during one time step, the Lorentz force distribution can be considered constant (Spitans 2013).

## 5.2 Method and hypothesis

We have used the commercial finite element package COMSOL Multiphysics® (COMSOL 2013) for the modelling of CCIM. The partial equations that govern the electromagnetic, heat transfer, and fluid dynamics fields can be solved with different numerical methods. COMSOL Multiphysics® implements a finite element method (FEM) for solving the partial differential equations (PDE) governing electromagnetism, heat transfer, and fluid dynamics.

The modelled cold cooper crucible has the same dimensions as the crucible of the CCIM installation at Mondragon Unibertsitatea, which is able to melt 1kg of titanium. Its inner diameter is 65 mm and its height 105 mm. The crucible has 16 sectors and the slits are 0.5 mm thick (Figure 5.2).

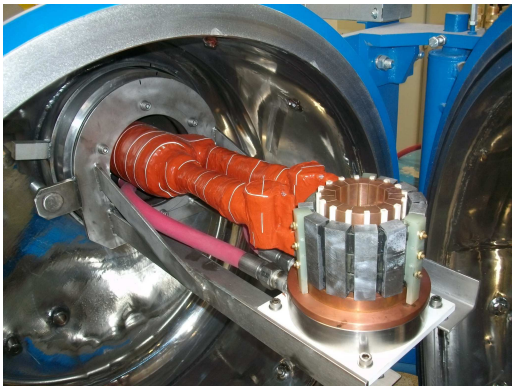

Figure 5.2. Crucible of the CCIM installation at Mondragon Unibertsitatea.

To obtain the flow field, the pressure distribution, the temperature, the solution of Maxwell's equations for the electromagnetic field, we assume the following hypothesis:

- The charge is in molten state. The change from solid state to liquid state is ignored. The solidification front is also neglected.

- The properties of the charge are constant. The dependence of some properties of the charge with respect to the temperature is neglected. The titanium alloy Ti-6Al-4V has been selected for our models. Table 5-1 shows the thermophysical properties of Ti-6Al-4V (COMSOL 2013, Mills 2002, Boivineau 2006).

Table 5-1. Properties of Ti-6Al-4V.

| | Symbol | Units | Ti-6Al-4V |
|---|---|---|---|
| Relative permeability | $\mu_r$ | - | 1 |
| Relative permittivity | $\varepsilon_r$ | - | 1 |
| Electrical conductivity | $\sigma$ | S/m | 7.407e5 |
| Heat capacity | $C_p$ | J/(kg·K) | 710 |
| Density | $\rho$ | kg/m$^3$ | 4940 |
| Thermal conductivity | $k_t$ | W/(m·K) | 7.5 |
| Dynamic viscosity | $\mu$ | Pa·s | 4.2e-3 |
| Surface tension | $\gamma$ | N/m | 1.7 |
| Emissivity | $e$ | - | 0.4 |

- The fluid is incompressible and Newtonian.

- The oscillating part of the Lorentz forces is negligible (Spitans 2013, Umbrashko 2006, Felten 2004). We have imposed the time averaged Lorentz as the source terms into the fluid model (Fautrelle 2009).

- The electromagnetic forces are higher than the natural convection (buoyancy forces induced by temperature differences). Thus, buoyancy forces are neglected.

- Thermocapillary (Marangoni effect) convection, which results from the temperature dependence of the surface tension, is neglected.

- In the energy equation of the heat transfer analysis, the viscous heating and pressure are negligible.

- We ignore the coil helicity.

- We determine the meniscus shape of the melt with a 2D axisymmetric model because of the good electromagnetic transparency of the slitted crucible wall (Bojarevics 2003a, Westphal 1995, Muiznieks 1999, Enokizono 1993).

- The magnetic Reynolds number characterizes the interaction between the fluid flow and the magnetic field:

$$R_m = \mu_0 \sigma U L \ , \tag{5.1}$$

where $U$ is the characteristic velocity of the flow, $L$ is the length scale of the flow, $\mu_0$ is the permeability of vacuum, and $\sigma$ is the electric conductivity of the fluid. In induction furnaces, $L$ is often considered as the crucible radius. The magnetic field behaves very differently depending on the conductivity of the medium. If $R_m$ is much less than unity, the magnetic diffusion dominates over magnetic convection. Hence, the velocity of the flow has little influence in the external magnetic field, since the field induced by the induced currents is negligible in comparison with the imposed field. In this case, the magnetic field is dissipative, and it damps the mechanical motion by converting kinetic energy into heat via Joule dissipation (Davidson 2001). Hence, electromagnetic field can be decoupled from the hydrodynamic problem (Xhu 1996). In our case, as in most industrial and laboratory scales, $R_m$ is very low ($R_m << 1$).

## 5.3 Description of the discretization method for 2D numerical models

2D numerical models serve for the calculation of the free surface of the melt. For the calculation of the meniscus shape, we assume that the crucible has a good electromagnetic transparency.

The deformation of the free surface is due to the electromagnetic forces generated by the coil. We have modelled this deformation using an Arbitrary Lagrangian-Eulerian (ALE) formulation. ALE is a hybrid combination of the classical Lagrangian and Eulerian approaches. The Lagrangian approach is useful for mechanical problems or “contained fluids” in which the boundary displacement is relatively small. Its main disadvantage lies in its inability to follow large distortions without avoiding a highly contorted mesh. The Eulerian approach is suitable for fluid flow when there are no free surfaces or moving boundaries. The ALE method combines the best features of these approaches using a moving grid whose velocity is neither zero (Eulerian) nor equal to the velocity of the fluid (Lagrangian).

The electromagnetic forces are defined as:

$$\mathbf{F} = -\nabla\left(\frac{\mathbf{B}^2}{2\mu_r\mu_0}\right) + \frac{1}{\mu_r\mu_0}(\mathbf{B}\cdot\nabla)\mathbf{B}, \tag{5.2}$$

where $\mu_0$ is the permeability of vacuum, $\mu_r$ is the relative permeability, and **B** is the magnetic vector potential.

The first term of the right hand side ($-\nabla(\mathbf{B}^2/2\mu_r\mu_0)$) is the irrotational part. The second term ($1/\mu_r\mu_0\cdot(\mathbf{B}\cdot\nabla)\mathbf{B}$) is the rotational part.

The free surface can be simulated taking into account only the irrotational part (hydrostatic steady state free surface model) or both parts (hydrodynamic free surface model).

### 5.3.1 2D hydrostatic steady state free surface model

There exist multiple articles describing the calculation of steady state meniscus shape for induction furnace taking into account only the irrotational part of the Lorentz force and neglecting the whirling part, which corresponds to recirculating alloy movement. The irrotational part is called electromagnetic pressure and is defined as (Davidson 2001):

$$P_{EM} = \frac{B_0^2}{4\mu_r\mu_0}, \tag{5.3}$$

where $B_0$ is the magnetic field in the surface, $\mu_0$ is the permeability of vacuum, and $\mu_r$ is the relative permeability of the fluid.

Since the electromagnetic field, the melt flow, and the free surface shape of the liquid are highly coupled, iterations are necessary to search for the equilibrium position of the metal free surface. In hydrostatic steady state (equilibrium state), the hydrostatic pressure ($P_{HS}$), the surface tension pressure ($P_{ST}$), the magnetic pressure ($P_{EM}$), and the hydrodynamic pressure ($P_{HD}$) must be in balance. Hence,

$$P_{HS} + P_{ST} + P_{EM} + P_{HD} = 0, \tag{5.4}$$

$$\rho g h_s + \gamma K + \frac{B_0^2}{4\mu_r\mu_0} + \frac{\rho}{2}(\mathbf{u}\cdot\mathbf{u}) = 0, \tag{5.5}$$

where $\rho$ is the density of the fluid, $g$ is the gravity, $h_s$ is melt head from the topmost point to the point under consideration, $\gamma$ is the surface tension, $K$ is the sum of the principal curvatures of the free surface, $B_0$ is the magnetic field amplitude in the surface, $\mu_0$ is the permeability of vacuum, $\mu_r$ is the relative permeability of the fluid, and **u** is the velocity of the flow.

At high frequencies, the hydrodynamic and surface tension pressure are negligible comparing to the hydrostatic and electromagnetic pressure (Sakane 1988, Xhu 1996, Lavers 1989). Their contribution in the surface geometry is small. Hence, along a free surface, the hydrostatic pressure and magnetic pressure have to be balanced. The result is a convex meniscus. Hence, from the equation (5.5), the time averaged deformation ($h_s$) of each point of the free surface can be written as,

$$h_s = -\frac{B_0^2}{4\mu_r\mu_0\rho g}. \tag{5.6}$$

We calculate the deformation of the free surface iteratively. In each iteration, we first calculate the electromagnetic field. Then, we estimate the displacement at each point of the surface according to:

$$dz = z_{00} + Z + h_s, \tag{5.7}$$

where $z_{00}$ is the maximum height of the free surface, Z is the height of the free surface before deformation, and $dz$ is the displacement at each iteration.

At each iteration, the nodes of the free surfaces move upwards and downwards according to the free surface equation (5.7). The geometry changes due to these movements of the nodes. Then, we calculate the magnetic field again for the new geometry. This process continues until the entire surface fulfills equation (5.6). We ensure the mass conservation with ordinary differential equations.

### 5.3.2 2D hydrodynamic free surface model

The use of full Lorentz forces gives a more precise free surface shape. Due to the low magnetic Reynolds number ($R_m$), the hydrodynamic calculation of the free surface can be solved sequentially. For the initial geometry, we calculate the electromagnetic field and the Lorentz force distribution. We use full Lorentz forces as mechanical momentum source for hydrodynamics calculation. We use ALE formulation to force the mesh nodes of the liquid surface to move with respect to the charge velocity.

In order to follow the motion of the fluid with the moving mesh, it is necessary to equate the mesh motion to the fluid normal to the surface. Hence, we apply the following kinetic condition on the free surface:

$$u_n = u_x \cdot n_x + u_y \cdot n_y, \tag{5.8}$$

where $u_x$ and $u_y$ are the components of the fluid velocity in $x$ and $y$ direction and $n_x$ and $n_y$ are the components of the normal vector.

The calculation of free surface is performed for a sufficiently small time step. Subsequently, the new shape of the free surface is used for the new electromagnetic calculation (Figure 5.3). The calculation of free dynamics is based on the assumption that for a sufficiently small time interval, the change in shape is so insignificant that during one time step the Lorentz force distribution can be considered stationary.

We have selected the *k-ω* turbulent model for the calculation of the melt flow. For the region of the calculation where the melt touches the crucible bottom and the crucible, we use the wall function boundary condition. In the free surface, we use the open boundary condition. We have implemented the surface tension according to the approach described by Carin (Carin 2012) using the weak form of the boundary condition:

$$\left[-\mathrm{p}\,\mathbf{I}+\mu\left(\nabla\mathbf{u}+(\nabla\mathbf{u})^{T}\right)\right]\mathbf{n}=0-P_a\mathbf{n}+\Gamma\gamma\mathbf{n}, \tag{5.9}$$

where **n** is the outward unit normal, $P_a$ is the surrounding pressure ($P_a$=0), Γis the curvature of the free surface, and $\gamma$ is the surface tension.

We have used MATLAB® (MATLAB 2012) integrated with COMSOL Multiphysics® in order to automatize this coupling. For that purpose, we have programed our own code in MATLAB environment.

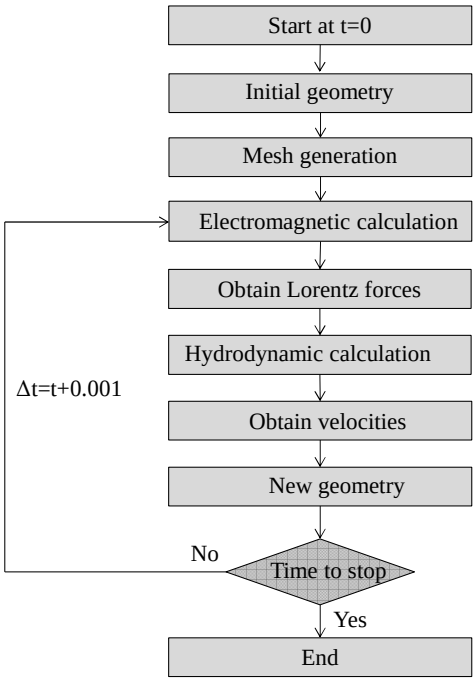


Figure 5.3. Algorithm for coupled electromagnetic and hydrodynamic free surface dynamic calculation.

## 5.4 Description of the discretization method for 3D numerical models

In theory, it is not possible to use two dimensional (2D) models to simulate CCIM problems due to:

a) The slits of the crucible make the problem no axisymmetric.

b) Three dimensional nature of turbulence in CCIM.

Hence, 3D models are necessary to suitably simulate the CCIM problem. In our 3D numerical models, we have exported the free surface from 2D hydrostatic steady state models.

As the magnetic Reynolds number is small, the magnetic field can be calculated previous to the flow and temperature calculation. Hence, the numerical modelling developed is divided into two steps: in the first step, we calculate the heat source generated by induced currents and the electromagnetic forces due to the magnetic field in the frequency-domain. In the second step, we introduce these values as input data in the numerical modelling and we calculate the variables of the heat transfer (temperature) and fluid flow (velocity components and pressure) fields.

The 3D numerical models are computationally intensive. However, it is possible to model only a sixteenth part of the real problem due to its geometrical periodicity. As it can be observed in figure 5.4, the model has four different domains: the charge, the crucible, a three turns coil, and the air.

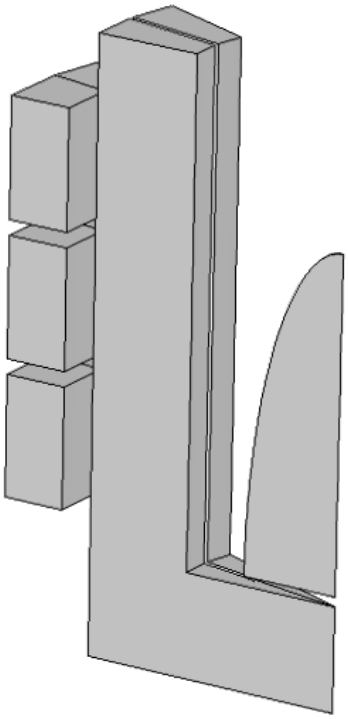

Figure 5.4. Model geometry.

We solve the electromagnetic equations in the entire computational domain (including the air, crucible, coil, and charge). The input data are the external current that crosses through the three turns coil and the working frequency.

An important feature in any electromagnetic analysis is the concept of skin depth. For example, for a working frequency of 9 kHz and titanium conductivity of 7.407e5 S/m, the skin depth is equal to 3.4 mm. Thus, we use 3.4 mm long elements to mesh the charge.

The Lorentz forces accelerate the fluid in the direction of the magnetic field gradient. Due to the confinement of the magnetic field to the skin depth, the Lorentz forces are restricted to this region and acceleration only takes place in a boundary.

In the outer boundaries of the computational domain, we use the magnetic insulation boundary condition, which imposes that the normal component of the magnetic field has to be zero.

The Navier-Stokes equations are only activated in the charge. We use a periodic flow condition for the exterior boundaries, wall function for the solid walls, and an open boundary condition at the free surface.

The temperature analysis is only activated in the charge. For the temperature boundary conditions, we use the periodic heat condition for exterior boundaries. The temperature boundary conditions for heat transfer analysis also include constant temperature setting (corresponding the melting point of Ti) on the surfaces that are in contact with the water cooled crucible walls, and radiation from the free surface of the melt.

## 5.5 Simulation advantages/limitations

One of the advantages of the selected methodology is that using a finite element method to calculate the different equations of each field makes easier the coupling among different physical quantities. Moreover, the numerical models are suitable for different geometry and parameters without any substantial changes in the model, and without including any correction factor.

The formation of inverted mesh elements and the rendering of the shape of the free surface between elements edge points are the biggest challenges of this methodology. In case of hydrostatic steady state free surface models, we are unable to obtain a solution of the free surface when the current is too high, because the free surface deforms too much. For high currents, the deformation leads to inverted mesh elements and the divergence of the solution. Coarser meshing made deformation for higher electric currents possible but reduce the shape resolution of the free surface drastically. In this case, the current has to be incremented in different steps.

The mesh size is a crucial parameter for the quality of the results and for the computational time. It is convenient to carry out the meshing under manual control.

## 5.6 Conclusions

In this chapter, we have shown the methodology used in our models. We have also provided a brief literature review on the subject.

There exist different numerical methods for solving electromagnetic, heat transfer, and fluid dynamic equations. Among the numerical methods found in the literature to approximate Maxwell equations, the

finite element method is the most extended one. Its main advantages are its geometric flexibly and the richness in theoretical mathematical tools useful to analyse the approximation of the problem. In the case of pure levitation melting, relatively high frequencies are typically used ($10^4$-$10^5$ Hz), which justifies the use of different electromagnetic skin-layer based theories. However, a typical frequency used in CCIM process is an order of magnitude lower and the magnetic field penetration is significant. In relation to the heat transfer analysis, both finite element method and finite difference method are the most used numerical methods. In fluid dynamics, until the finite volume method was developed, the fluid dynamics were calculated using the finite element method. Nowadays, the finite volume method is the most common method for fluid dynamic problems.

Softwares to model induction processes have advanced to the point where, today, several very sophisticated packages are available commercially that are capable of taking into account most, if not all, of the various factors noted in this dissertation.

In our case, we use the commercial finite element package COMSOL Multiphysics® for the modelling of CCIM. As the finite element method is used to solve electromagnetic, heat transfer, and fluid dynamic equations, the same mesh is used for all physics. Thus, there is no additional complexity associated to the heat source and electromagnetic forces calculated in the first step as input data for the second step.

Despite the use of 2D axisymmetric models by some authors to simulate CCIM, 3D computations seem to be necessary to reproduce the slits of the crucible and the three dimensional nature of turbulence in CCIM. There exists a wide range of turbulence modelling approaches for the simulation of the turbulent melt flow and the heat and mass transfer processes. But up to now, an universal and always reliable modeling approach that can be used for the development and design of industrial metallurgical applications is not available. The well-known $k$-$\varepsilon$ model is not able to simulate well the heat transfer. Both $k$-$\omega$ and LES turbulent models give better results. In our case, since COMSOL Multiphysics® does not have the possibility to implement LES, we have used the $k$-$\omega$ model.

CHAPTER 6

# NUMERICAL RESULTS

In this chapter, we first validate our numerical models comparing the numerical results with experimental results carried out by other authors. Then, we present additional numerical results in 2D and 3D. It can be observed that increasing the current and the frequency the superheat in the melt rises. The stronger inductor current also increases the amplitude of initial perturbation and the steady state meniscus height. An increasing of current leads also to higher maximum flow velocities. The frequency has a limited influence in the velocity. In relation to the surface deformation, the increasing frequency produces a sharp surface deformation only very close to the crucible wall. Around the symmetry axis, the surface is flat.

## 6.1 Validation of numerical models

In order to validate our numerical models, comparisons of the numerical results with experiments are necessary. During this dissertation, besides the development of a numerical modelling of CCIM, we have performed the setting up of an installation of CCIM and the melting of titanium parts. The installation does not have any device to measure CCIM parameters such as temperature, velocity, or efficiency. For this reason, we have validated our models by comparing our numerical results with the results obtained from experiments performed by other researchers. The parameters that have been compared are:

- Meniscus shape,
- temperature, and
- efficiency.

### 6.1.1 Meniscus shape

The free surface of 2D hydrostatic steady state and 2D hydrodynamic free surface models have been compared with appropriate experimental results.

The experimental measurements used for the comparison were carried out by Kirpo *et al.* (Kirpo 2008) in the induction furnace at the Institute of Electrotechnology of Hannover. The induction furnace crucible (Figure 6.1) has an inner radius of 158 mm and a height of 756 mm, where the inductor height is 570 mm. The material used is the one called Wood's metal, which has a melting point of 72ºC, a dynamic viscosity of 4.2 $10^{-3}$ kg/m· s, a density of 9.700 kg/m$^3$, and a conductivity of $10^6$ S/m.

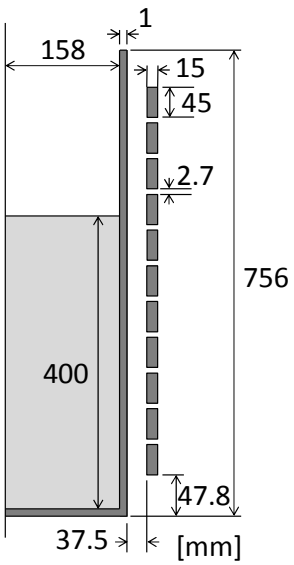


Figure 6.1. Induction furnace at the Institute of Electrotechnology of Hannover (Spitans 2013).

The experiment had an effective inductor current $I$=2 kA, an alternating current frequency $f$=385 Hz, and an initial crucible filling $h_0$=400 mm. Figure 6.2 shows the comparison of our 2D hydrostatic steady state and 2D hydrodynamic free surface models meniscus shape with experimental data (Kirpo 2008).

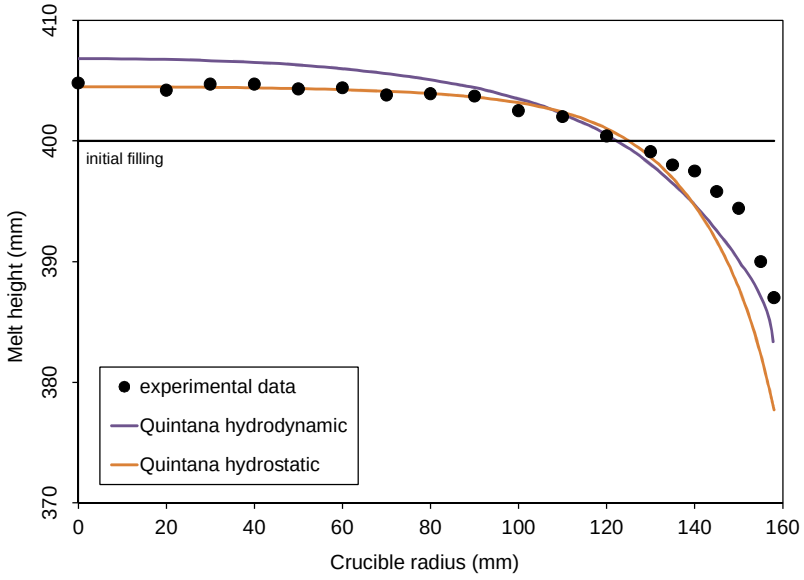


Figure 6.2. Meniscus shape comparison among different models and experimental data.

The hydrostatic model shows a better agreement with the experimental data (points) in comparison with the hydrodynamic model.

In Kirpo *et al.* experiment, the free surface deformation is insignificant if compared with the initial crucible filling $h_0$. For this reason, we have also compared the hydrostatic free model meniscus shape with Lavers and Ahmed experiments (Lavers 1988b). The crucible inner diameter is 124 mm, the coil inner diameter is 195 mm, the coil length is 180 mm, and the melt is aluminum. The inside bottom surface of the crucible is aligned with the bottom of the coil (Figure 6.3).

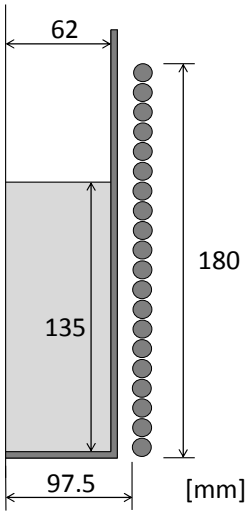


Figure 6.3. Lavers *et al*. experiments crucible geometry (Lavers 1988b).

The shape of the surface has been predicted at values of frequency 1330 Hz and current of 400 A, where the level of the melt is 135 mm (Bojarevics 1999). In this experiment, a considerable meniscus shape is produced due to the Lorentz force acting on the fluid (Figure 6.4).

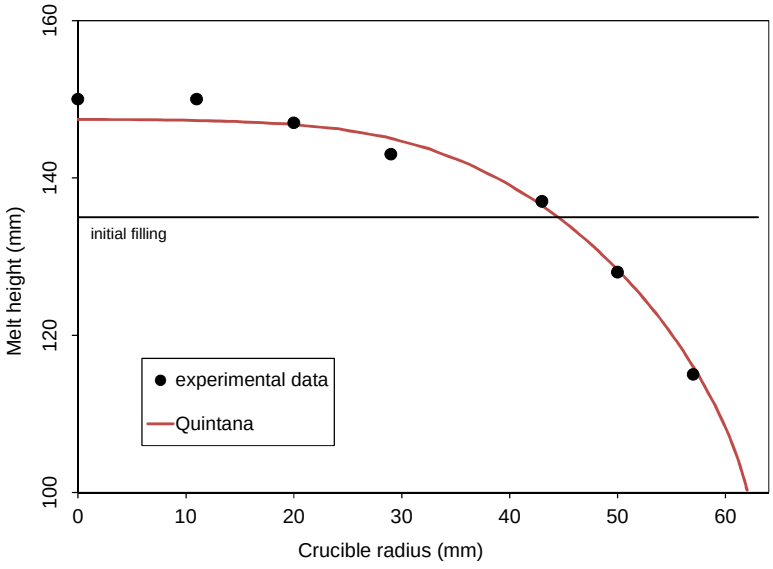


Figure 6.4. Meniscus shape.

The meniscus shape of the 2D hydrostatic steady state model shows a good agreement with the experimental data. A slight difference can be observed in the surface nearest to the crucible wall.

### 6.1.2 Temperature

We have validated the temperature distribution in the melt with the experimental investigations carried out in the laboratory induction furnaces of Institute of Electrotechnology of Hannover (Baake 2007). The experimental investigations were performed using a 6 kg pure aluminium piece in a cold crucible with an inner radius of 78 mm and a height of 260 mm (Figure 6.5). The output power of the generator was 200 kW at a frequency range of 8-10 kHz. The CCIM is composed of 14 segments. The five inductors coil height is about 200 mm (Umbrasko 2008).

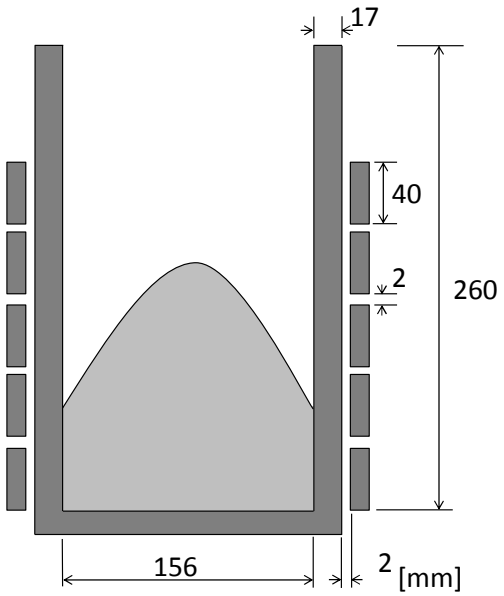


Figure 6.5. Sketch of the induction furnace with cold crucible (Baake 2007).

Figure 6.6a shows the time-averaged temperature measured by Baake *et al.* (Baake 2007). The maximum superheat is located near the crucible wall above the wall skull. At this point, the melt is close to the crucible wall but without direct contact to the skull, thus the ratio between the induced power density and the heat losses is maximum. In the region of the melt center, the temperature distribution is quite homogeneous due to the good turbulent mixing of the melt. The lowest temperature value is located near the bottom skull, where no power is directly induced and high heat conduction losses are located. The radiation losses from the free surface lead to the formation of a relatively cold area at the top.

Figure 6.6b shows the temperature distribution in the melt of our 3D numerical model. A good agreement can be observed among the measured and calculated temperature distribution. There is a slight difference in the top. In the numerical modelling, the top area is not as cold as in the measured calculation that could be due to boundary conditions.

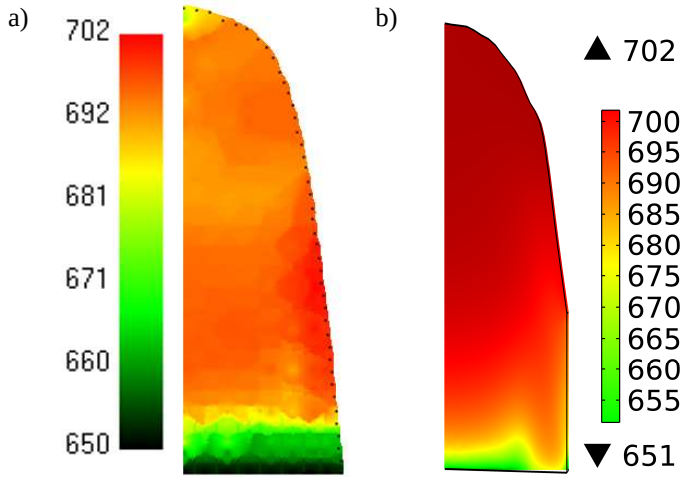


Figure 6.6. a) Measured (Baake 2007) and b) simulated temperature (ºC) distribution.

### 6.1.3 Power efficiency

The efficiency of CCIM is a crucial parameter of the process. It is essential that the numerical models accurately estimate this quantity. We have compared the efficiency with Ernst *et al.* (Ernst 2009) experiments (Figure 6.7). The installation has a 16 sector hemispherical cold crucible. The slit thickness between sectors is 350 μm. The 200 g ellipsoidal shaped charge is pure titanium corresponding a volume of 45 $cm^3$. The measurement is applied with the generator at a given power of 20 kW and frequency of 93.3 kHz.

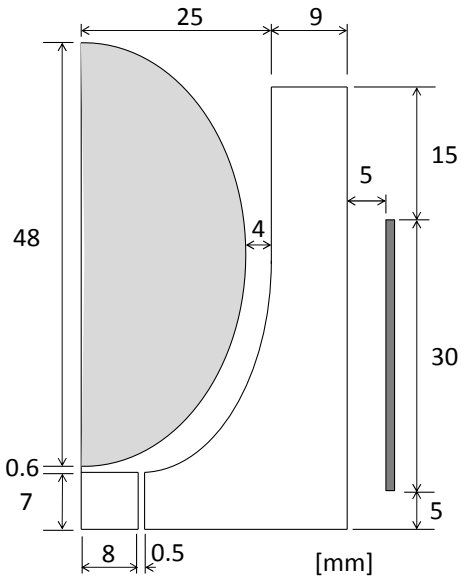


Figure 6.7. Sketch of cold crucible induction furnace (Ernst 2009).

The second column of table 6-1 contains the experimental Joule power values from different sub-assemblies of CCIM installation. The third column displays the Joule power values of our numerical model.

Table 6-1. Comparison among experimental and modelling results.

| Elements of CCIM | $P_{exp}$ (Ernst 2009) (kW) | Our model (kW) |
|---|---|---|
| Inductor+capacity | 5.86 | 5.98 |
| Crucible+casting finger | 12.14 | 11.57 |
| Charge | 2.8 | 3 |
| Total | 20.8 | 20.55 |

There is good approximation among the results. The error between the numerical results and experimental data of the inductor, crucible, and charge are 2%, 4.6%, and 7% respectively. Hence, this model is able to predict qualitatively the tendencies and permit to study the influence of electrical parameters.

The 2D numerical approach for free surface calculation is formulated and it verification approves the model accuracy. Inevitable imprecisions in geometry or material properties might lead to insensible deviations of meniscus shape. Both 3D numerical models temperature and efficiency results show good agreement with experimental measurements.

## 6.2 2D simulations

We have used 2D models to calculate the free surface deformations. The free surface of the melt affects directly to the superheat. Hence, a good accuracy of the meniscus shape is vital. The deformation of the free surface is affected by the electromagnetic forces generated by the coil. In order to visualize the effect of the current in the meniscus shape, we have calculated the steady state meniscus shapes for different currents for the installation of CCIM at Mondragon Unibertsitatea (MU) (Figure 5.2). Figure 6.8 shows the meniscus shape for 2D hydrostatic steady state free surface model for different current intensities with a frequency $f$=9 kHz and an initial crucible filling $h_0$=70 mm. Increasing the current magnifies the electromagnetic force that squeezes the alloy radially and leads to a greater surface deformation.

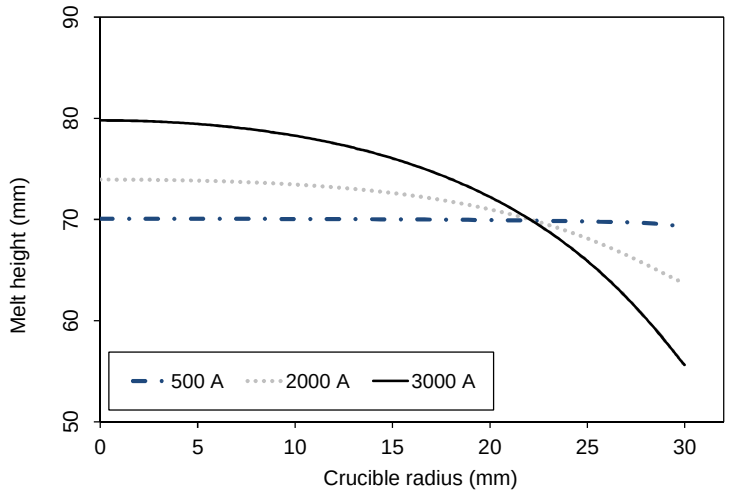


Figure 6.8. Free surfaces for different inductor effective currents $I_{ef}$ : 500, 2000, and 3000 A.

After deformation, the magnetic and hydrostatic pressures should coincide along the free surface. Figure 6.9 shows the difference between the magnetic and hydrostatic pressures at the surface before and after deformation for a 3000A current. After deformation, magnetic and hydrostatic pressures are almost equal, as presumed.

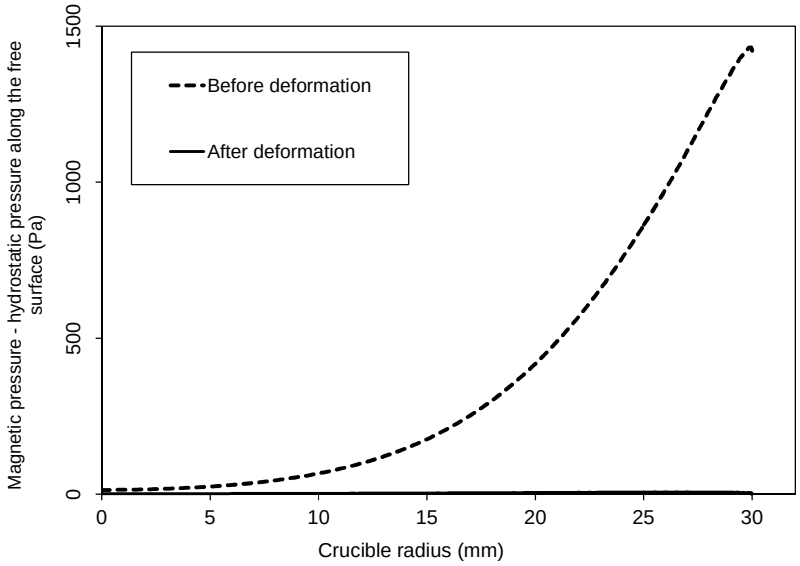


Figure 6.9. Difference between magnetic and hydrostatic pressure along the free surface before and after deformation for a current of 3000 A.

In case of hydrodynamic meniscus shape, figure 6.10 shows the transient free surface shapes at different times for a current $I$=2000 A, $f$=385 Hz, and initial crucible filling $h_0$=400 mm for a crucible geometry of the Institute of Electrotechnology of Hannover (Figure 6.1). The vertical axis represents the height of the melt (mm) and the horizontal axis indicates the crucible radius (mm). It can be observed the dynamics of the process. When the current starts flowing through the coil, the meniscus height increases and reaches a maximal value. Then, the height of the meniscus decreases. This fluctuation continues until the free surface reaches a quasi-steady state. From this moment, the free surface only oscillates slightly around this geometry.

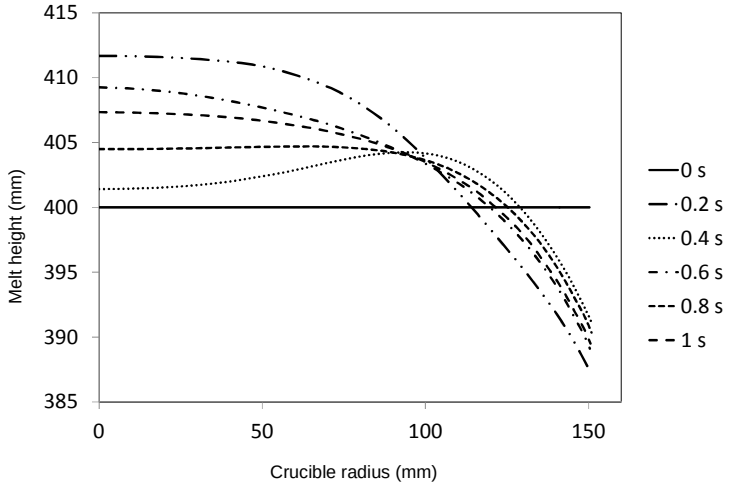


Figure 6.10. Free surface shapes at different time moments for a current $I$=2000 A and $f$=385 Hz.

As example, figure 6.11 illustrates the meniscus shape at $t$=0.255 s. The flow pattern in these installations is formed by the influence of electromagnetic forces and usually comprises two or more toroidal dominating recirculating vortices.

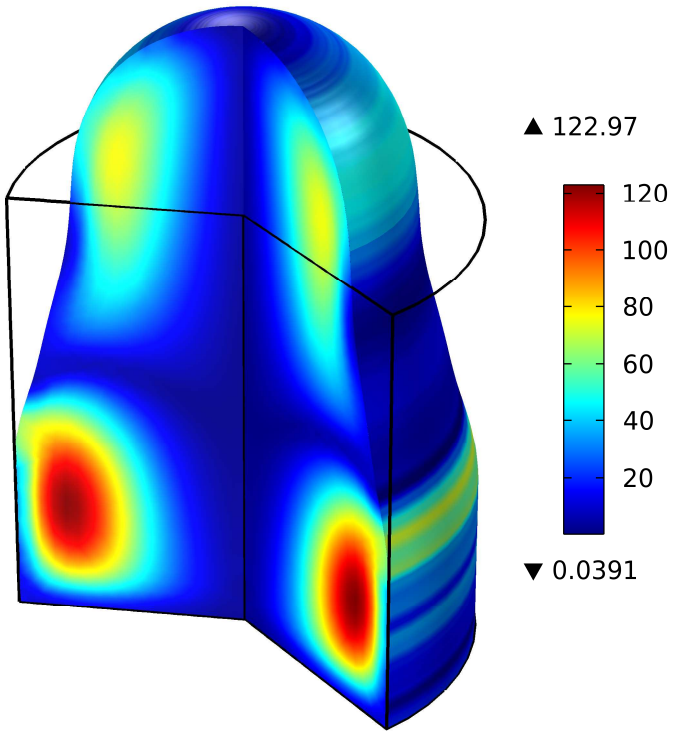


Figure 6.11. Vorticity in the melt (1/s) at $t$=0.255 s for a current $I$=4500 A and a frequency $f$=2 kHz for a crucible geometry of CCIM at MU.

## 6.3 3D simulations

In the results shown in this section, we have exported the free surface from 2D hydrostatic steady state models. We select a current of 3000 A and a frequency of 6.7 kHz, which are the parameters corresponding to the CCIM installation we have in MU.

The following pictures illustrate the most important characteristics of CCIM, such as the magnetic flux, the current density in the melt, the Lorentz forces in the melt, the velocity pattern in the melt, and the temperature in the melt.

Figure 6.12 shows a simulated numerical example of the effects of a cold crucible on the magnetic field distribution. It is possible to see how the magnetic flux passes through the air gap between two adjacent copper wall segments and penetrates in the charge a distance similar to the skin depth. It can be seen from the figure that the flux density is maximum near the coil and almost zero at the boundary of the enclosed domain.

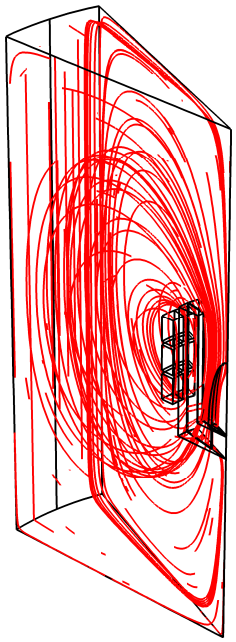

Figure 6.12. Magnetic flux lines.

Figure 6.13 presents the induced current density inside the charge. It can be clearly seen from the figure that the induced current density is higher at the surface of the charge due to the skin depth. According to the equation (4.24), the induced current density penetrates 3.98 mm in the melt.

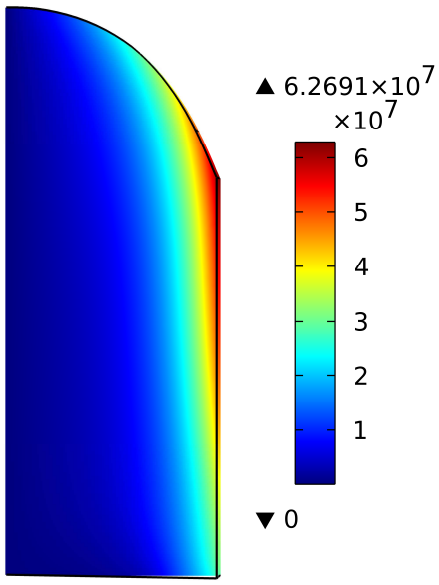


Figure 6.13. Normal component of the current density ($A/m^2$).

Figure 6.14 shows both the radial and axial electromagnetic forces. Due to the rotational Lorentz forces, in the middle height of the melt the fluid is accelerated in inward direction.

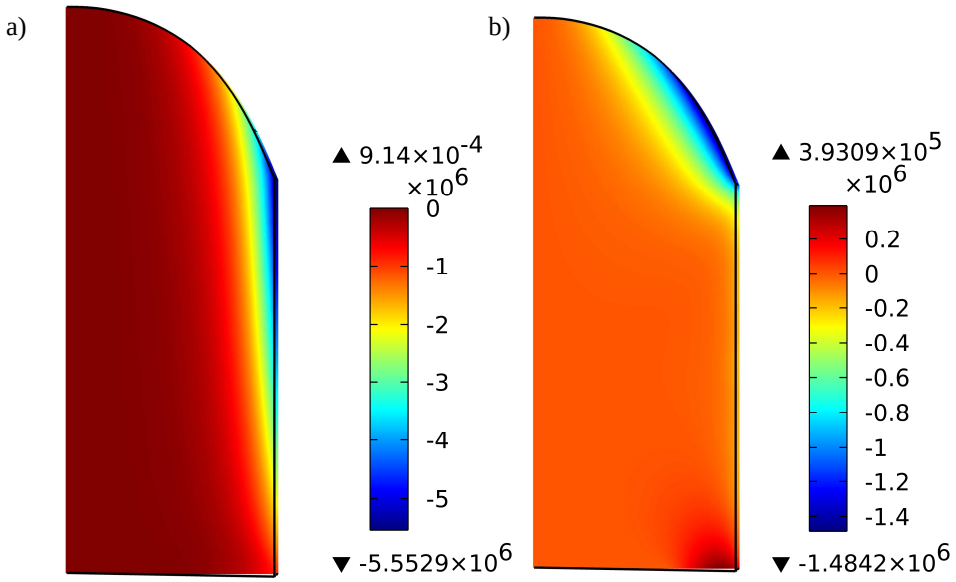


Figure 6.14. a) Radial Lorentz forces (N/m$^3$) and b) axial Lorentz forces (N/m$^3$).

Figure 6.15 shows the velocity in the melt. The time-averaged flow pattern consists of two vortexes. Time averaged flow patterns simulated with the present magnetohydrodynamic flow model appear to be correct, since similar mean flow patterns have been found, both experimentally (Pericleous 2001) and in other numerical studies (Umbrasko 2008).

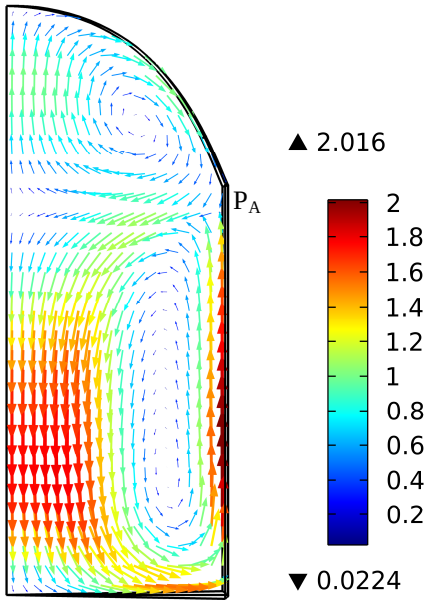


Figure 6.15. Velocity vector (m/s).

Averaged flow consists of two toroidal vortices, which are placed symmetrically in the melt. The inward direction of the flow in the middle region is determined by the Lorentz forces distribution in the melt. Lorentz forces are concentrated in the near wall zone of the melt and have a maximum value in the region where the free surface and the crucible wall approach each other (Figure 6.15, point $P_A$). At this location, the flow moves towards the centre of the crucible from all sides, dividing it into two parts. One moves towards the top and another towards the bottom along the symmetry axis and, in the middle near the crucible, they join together. It can be perceived as a collision of two fluid jets, which come from opposite directions. The flow achieves its maximal velocity near the crucible wall.

Figure 6.16 illustrates the temperature in the melt after 20 seconds. The temperature distribution is influenced by the thermal boundary conditions. The maximum superheat is attained near the crucible wall and above the wall skull ($P_B$). In the center region of the melt, the temperature distribution is homogenous. The lowest temperature values are attained near the skull. The radiation losses from the surface lead to the formation of a relatively cold area at the top, around 1692ºC ($P_C$).

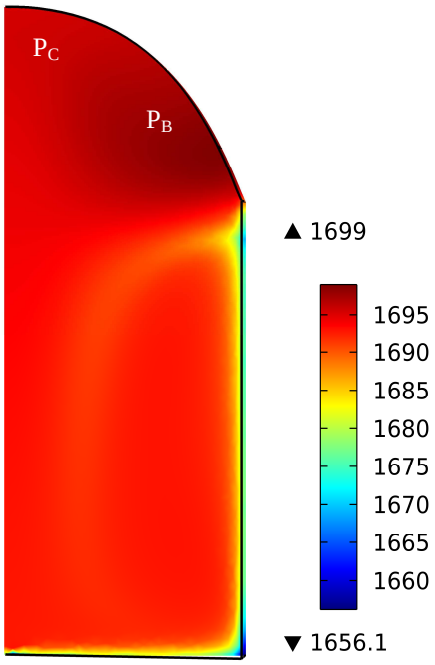


Figure 6.16. Temperature (ºC) in the melt after 20 seconds.

### 6.3.1 Influence of the current in the meniscus shape and the superheat

An increased current magnifies the electromagnetic force, which squeezes the alloy radially and causes greater surface deformation (Figure 6.17). Three different current amplitudes are employed to analyze the influence of the inductor current in the meniscus dome: 500 A, 2000 A, and 3000 A. The selected frequency is $f$=9 Hz.

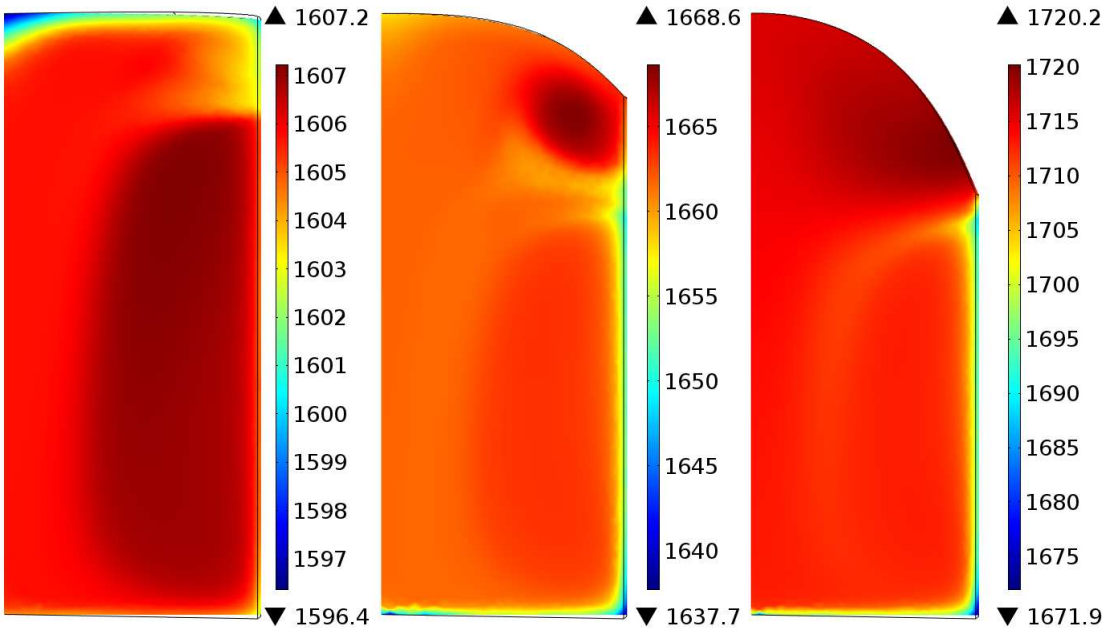


Figure 6.17.Influence of the current in the meniscus shape and the temperature (ºC) for different inductor effective currents $I_{ef}$; $I_{ef}$ =500 A (left), $I_{ef}$ =2000 A (center), and $I_{ef}$ =3000 A (right).

Increasing the current (power) leads to a higher power induced in the melt. Therefore, the temperature increases. Furthermore, the free surface deformation is higher and the contact zone between the melt and the cooled crucible decreases.

On the other hand, an increase of the induced power leads to higher maximum flow velocities in the melt (Figure 6.18), as physically expected.

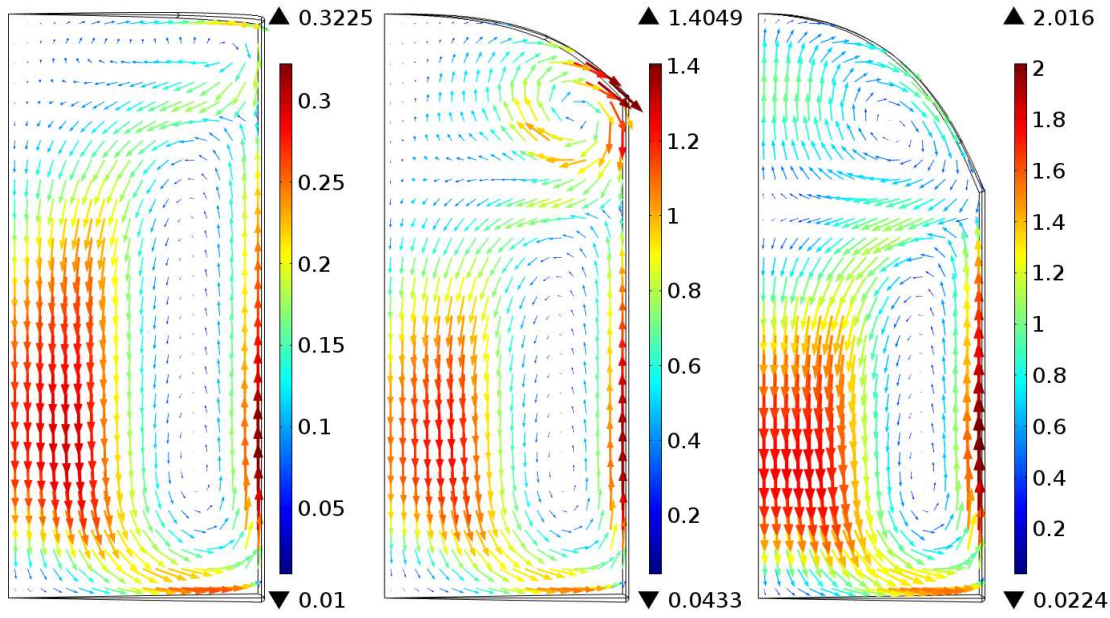


Figure 6.18. Influence of the current in the meniscus shape and the velocity (m/s) for different inductor effective currents $I_{ef}$; $I_{ef}$ =500 A (left), $I_{ef}$ =2000 A (center), and $I_{ef}$ =3000 A (right).

### 6.3.2 Influence of the frequency in the meniscus shape and the superheat for a given current

According to theoretical principles, the power released within an inductively heated charge increases proportionally with the square root of the AC frequency for a fixed current magnitude in the exciting coil. In order to see the influence of the frequency, we have used three different frequencies: 1 kHz, 5 kHz, and 9 kHz. The current in all of them is 2000 A.

Figure 6.19 shows the influence of the operating frequency on the surface deformation and temperature of the melt. The superheat increases with the frequency.

The deformation augments when increasing the frequency from 1 kHz to 5 kHz. However, there is no noticeable increment in the deformation when increasing the frequency from 5 kHz to 9 kHz. An increase on the frequency squeezes out the field, leading to a sharp surface deformation in the proximity of the crucible wall. Around the symmetry axis, the surface is flat.

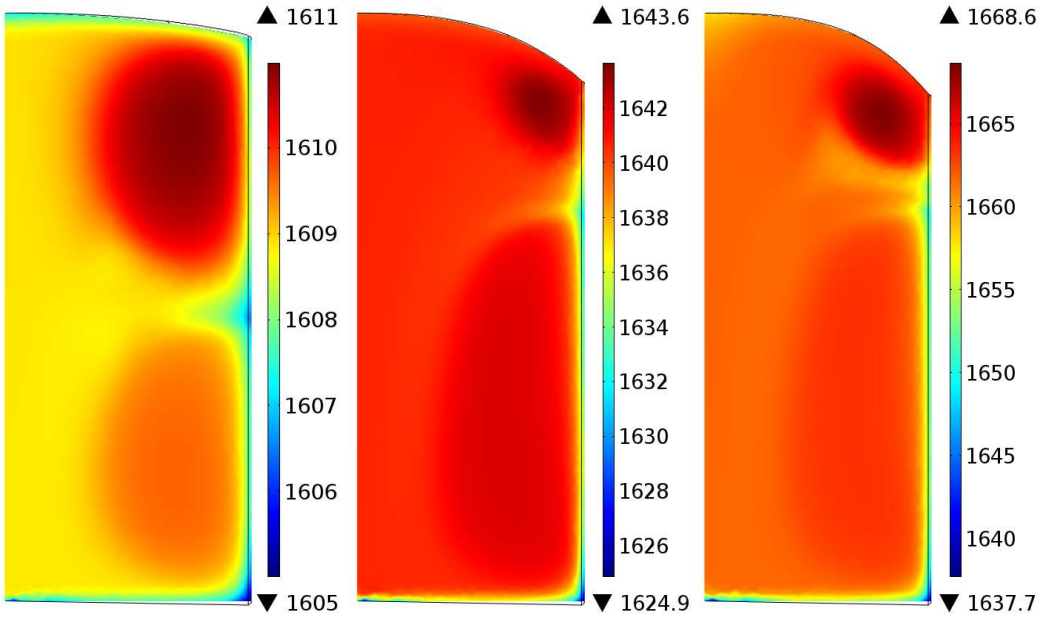


Figure 6.19. Influence of the current in the meniscus shape and the temperature (ºC) at different frequencies; $f$ =1 kHz (left), $f$ =5 kHz (center), and $f$ =9 kHz (right).

Figure 6.20 depicts the influence of the frequency in the velocity. The frequency has a limited influence in the velocity.

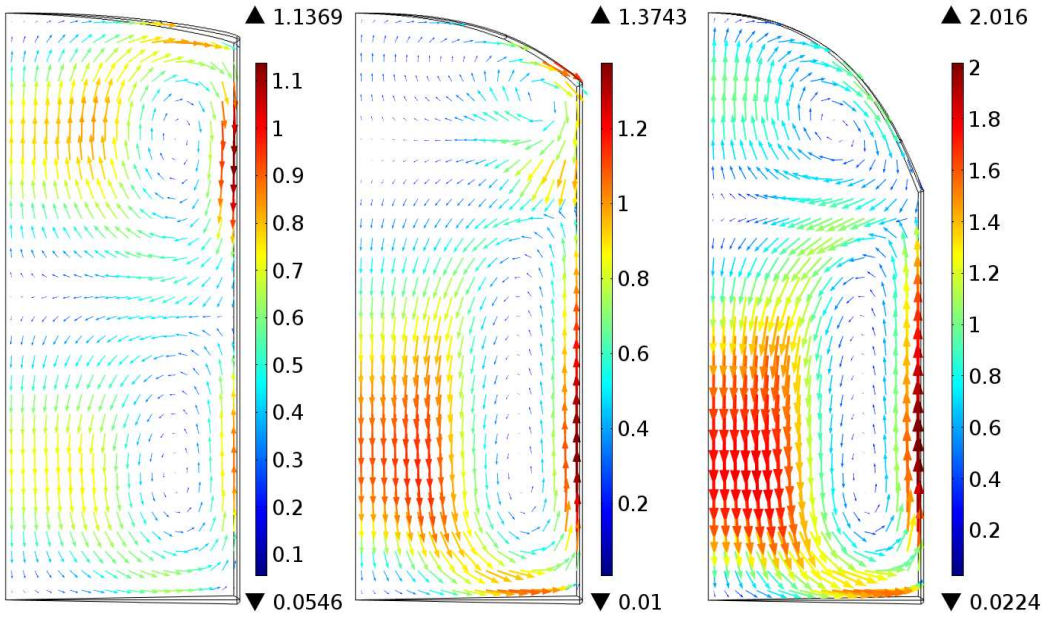


Figure 6.20. Influence of the frequency in the meniscus shape and the velocity (m/s) for different frequencies; $f$ =1 kHz (left), $f$ =5 kHz (center), and $f$ =9 kHz (right).

### 6.3.3 Influence of the slit thickness in the efficiency

The power induced in the melt strongly depends on the width of the slits. The heat losses in the copper fingers are significant due to the copper high thermal and electric conductivities. Therefore, the goal is to optimize the number and position of the cooper sectors in the crucible in order to minimize these losses. Table 6-2 shows the influence of the slit thickness in the different elements of CCIM for a current $I$=3980 A and $f$=1000 Hz.

Table 6-2. Power losses in each element of CCIM.

| | 1 mm | 2 mm | 3 mm |
|---|---|---|---|
| Charge (kW) | 1.27 | 1.35 | 1.4 |
| Crucible(kW) | 2.93 | 2.64 | 2.42 |
| Coil (kW) | 5.92 | 5.7 | 5.52 |
| Total (kW) | 10.12 | 9.7 | 9.35 |
| Efficiency (%) | 12.57 | 13.93 | 15.02 |

Increasing the slit thickness, the power losses in the crucible decrease and increase in the charge. Hence, there is a significant improvement of the efficiency.

## 6.4 Conclusions

In this chapter, we have first validated our numerical models and we have presented relevant numerical results. The numerical results of the electromagnetism, thermal, and hydrodynamics behaviour of the cold

crucible induction furnace are in good agreement with the experimental data from different authors. Moreover, the 2D numerical approach for melt free surface calculation provides a sufficient model accuracy. Hence, the generally good agreement between the model and the experimental measurements gives confidence that the model is realistic. The employed $k$-$\omega$ turbulence model seems to be suitable for CCIM problems.

Also, our understandings of the complex interactions that occur inside the crucible have increased due to the numerical results. These results give useful insights about the CCIM process. We have noticed that increasing the current and the frequency, the superheat in the melt rises. The stronger inductor current also increases the amplitude of initial perturbation and the steady state meniscus height. The height of the steady state meniscus contributes to flow pattern formation and vortex positional relationship. The models provide useful information about the efficiency of the process, predicting the power released in the crucible, coil, and charge. Increasing the slit thickness, the power losses in the crucible decrease and increase in the charge. Hence, there is a significant improvement of the efficiency.

This model produces fast good quantitative results for the velocity, and it also describes the heat transfer quantities in the melt. Thus, our numerical models are capable of predicting the superheat of the melt. This is crucial because one of the most important parameter of titanium casting is the pouring temperature. Hence, our numerical models are a powerful tool for optimizing the design and operational parameters of CCIM furnaces.

CHAPTER 7

# EXPERIMENTAL RESULTS

In the first part of this chapter, we present the cold crucible induction melting (CCIM) furnace of Mondragon Unibertsitatea (MU). We state the characteristics of the facility and the problems that we have overcome during the setting-up of the installation, which is capable of melting 1 kg of Ti-6Al-4V. In the second part of this chapter, we explain the experiments that we have performed.

## 7.1 CCIM facility

The main part of the thesis is focused on the development of a numerical modelling of CCIM to help in the optimization of the main parameters of the process. The other part deals with the setting-up of a CCIM installation and the fabrication of high added value components. Figure 7.1 shows an overall view of the equipment of CCIM available at MU.


Figure 7.1. CCIM installation.

The installation of CCIM consists in a vacuum chamber, a pumping system, a power supply, and a cooling system. Figure 7.2 illustrates a simplified sketch of the installation of CCIM.

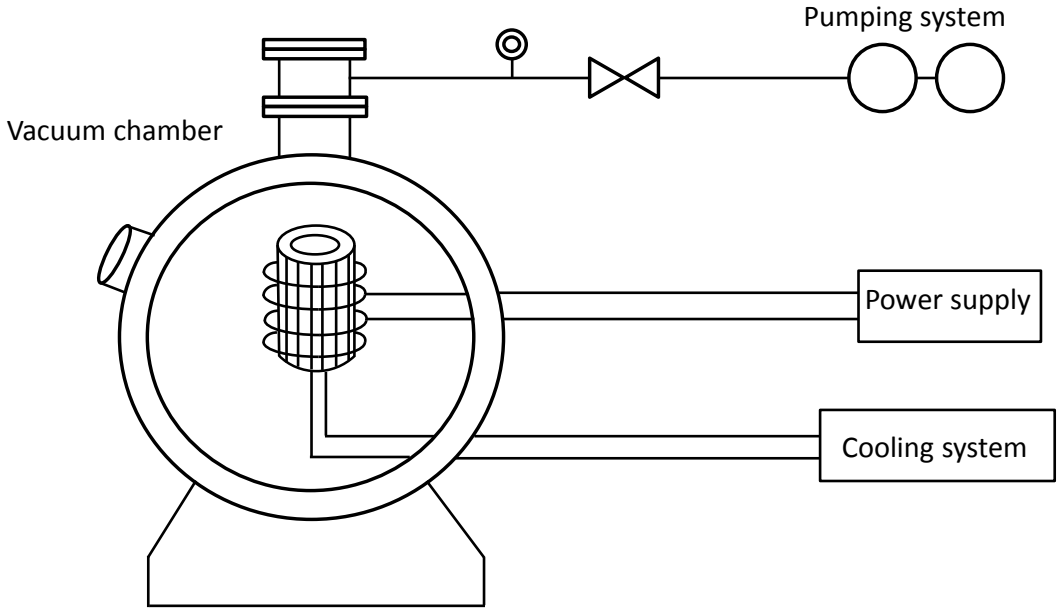


Figure 7.2. CCIM sketch.

The vacuum chamber is equipped with ports to accommodate the pumping system, the cooling system, the coaxial type power feedthrough, and the pumping system. The coaxial type power feedthrough is made of copper. The chamber is double wall and water cooled. The internal surface is polished to improve vacuum conditions. Furthermore, the furnace has a turn table for centrifugal casting. The induction coil and the water cooled copper crucible are attained inside the chamber. The crucible is tilted using an electrical motor-reducer controlled by a joystick installed on the operator's pulpit.

The CCIM installation at MU is able to melt 1kg of titanium (350 $cm^3$). The crucible must contain the material prior to initiation of melting as well as the molten pool during processing. The heat exchange capacity of the crucible must be sufficient to remove heat rapidly enough to maintain a metal skull at the external surface of the melt and maintain the crucible temperature below the material melting point. After these prerequisites are fulfilled, the crucible must be designed to allow a varying magnetic field associated with eddy current heating to pass through in a known and predictable way. It is also desirable that electrical energy losses in the crucible be minimal. There are mainly two types of cold crucibles: the first one has an inner wall of hemispherical (or conical) shape for a given quantity of material. The second one has a vertical straight cylindrical inner wall allowing the continuous casting of a solidified ingot thanks to a downward mechanical pulling device at the bottom. The crucible of MU installation is of the first type (Figure 7.3). Its inner diameter is 65 mm and its height 105 mm. The crucible has 16 sectors and the slits are 0.5 mm thick.

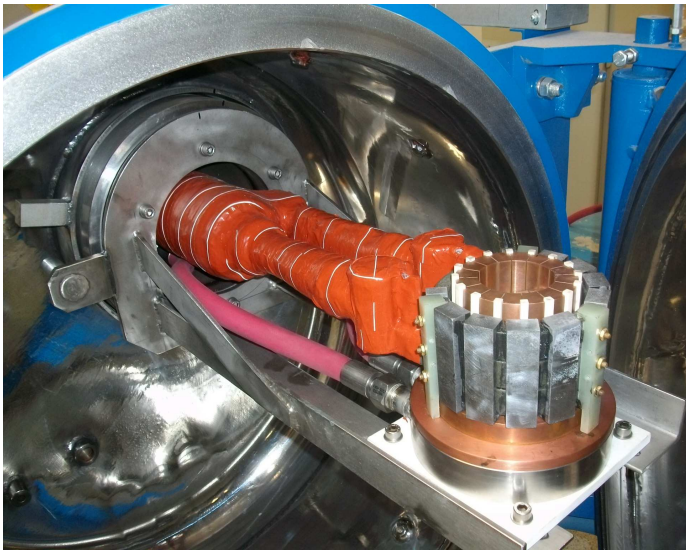

Figure 7.3. Crucible.

The associated coil is also cylindrical with a fixed diameter. Conventional designs have a uniform spacing between the induction coil and the exterior walls of the crucible. There are two reasons why a cylindrical geometry has been adopted as common. First, the cylinder exhibits a very low ratio of surface area to volume relative to other geometries, reducing the heat loss. Second and perhaps more important, the cylindrical shape simplifies calculations and most closely matches the geometry of inductors for which much theoretical work has been used. The coil has an equal spacing among the wires. The coil should be configured (diameter, number, and spacing of turns) to maximize efficiency of energy transfer from the generator to the melt. The design is constrained by the physical dimensions of the crucible, the electrical properties and volume of the melt, and the output electrical properties of the generator. The inductance of the coil increases with the area and the number of windings. High impedance does not allow passing sufficiently high currents through the coil. The induction coil is wound from a copper tube that is coated with a silicon thermal resistant insulating fiber jacket. The induction coil is internally provided with a cooling water circulation passage to communicate at the two ends with external water inlet and water outlet made of cooper tubes. The power supply is connected to the coil via busbars, flexible leads, and a coaxial port which feeds the power through the wall of the vacuum vessel and allows the crucible to be tilted. Moreover, the coaxial port allows water to be supplied to the coil. The power supply gives a maximum current of 3 kA at a frequency of 6 kHz.

The pump system is composed of a rotary piston pump MICROVAC 149H and a mechanical booster MB43 (Figure 7.4). The pumps are capable of achieving a 5 $10^{-2}$ mbar vacuum in the chamber. The CCIM installation has also a partial pressure system installation that permits to melt in argon.

Figure 7.4. Rotary piston pump H149 (left) and mechanical booster MB43 pump (right).

Another important element of CCIM installation is the cooling system. The aim of the cooling circuit is to cool the crucible, the coil, the power supply, the pumps, and the chamber. The cooling system has a closed loop water-cooling circuit. The chiller pumps ionised water from the buffer tank to the cooling circuit. The water is then split to cool all elements of the installation. After cooling, the water is returned to the buffer tank. The water chiller is a Hyperchill ICE 116, with a capacity of 500 liter and a cooling capacity of 116 kW. Drain lines of the crucible and vacuum chamber are equipped with a flow sensor. The flow sensors are interlocked with an audio/visual alarm system to provide advanced warning of potentially serious furnace malfunctions. To protect the critical circuit in the event of line power failure, the system has an emergency supply of cooling.

## 7.2 CCIM facility's set-up

During the setting-up of the CCIM installation, we faced with various problems. One of the first problems was the high voltage in the coil. This problem happened because the coil was designed for an original CAMI 50 kW power supply. The installation supplier designed the coil based on the original characteristics of the power supply. However, the power supply existent on MU is second handed and it has some modification in its capacitors and transformers. Specifically, it did not have the matching box that in theory it should have. The result was a higher voltage than the maximum accepted output voltage of the coil, which is 110 V. Since this high voltage could cause a breakdown, the power supply was not turned on.

We tried to solve the problem with the acquisition of an external matching box. With the matching box, the voltage in the coil was lower than the maximum output voltage of the coil. However, it was too small, 46 V, due to the large resistance of the leads. With this voltage it was impossible to melt the charge.

The solution to overcome this problem was to minimize the resistance of the leads buying more efficient ones. The old leads had a voltage drop of 100 V. On the other hand, the new efficient leads have a voltage drop of 50 V. Hence, the voltage in the coil is 70.7 V. Although the voltage was correct, it was not possible to melt the charge because the inlet water temperature of the power supply attained a high value. As consequence, the power supply switched off automatically. The reason of the heating of the water of the power supply was that the chiller was not capable of cooling enough to keep the water temperature below 30ºC. Finally, we decided to buy a new power supply and chiller. The new power supply has been designed to 'match' with the load. This load means the coil, the crucible, and the metal to be melted in the crucible. With the acquisition of the new power supply of 100 kW and a Hyperchill ICE 116 water chiller, it has been possible to start melting titanium.

We needed 28 months for the setting-up of the installation.

## 7.3 Experiments

After the setting-up of the installation, we have cast different parts. One of them has been a turbine blade (Figure 7.5). Turbine blades are structural applications ideally suited for the use of titanium parts. General dimensions of the part are 25 mm x 36 mm x 137 mm. The thinnest section of this thin walled component is 1.5 mm. Investment casting is a suitable process to obtain such complex and high quality components because of its repeatability, high dimensional accuracy, and surface finishing.

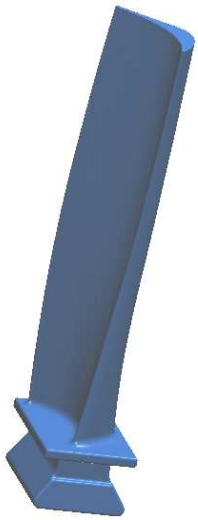

Figure 7.5. Turbine blade.

The first step of the investment casting process is the design of the mould. In order to fabricate a good mould design, we have used the commercial software Flow3D® (FLOW-3D 2013). It is an essential strategy the employment of filling and solidification simulation software as Flow3D® to optimize the feeding systems of the mould. The filling of thin walled elements with titanium is quite challenging due to its low fluidity. Flow3D® software has been used to validate the filling of the mould, as well as to

identify the process parameters required for the casting of the thin-walled complex parts. We have designed several gating and feeding systems before reaching an appropriate mould design. Finally, for the first experiments, we have used the gravity top gated casting method, which consists of pouring the metal downhill from the crucible into the mould.

After designing the mould, we have produced a wax pattern with the same geometry of the final product (Figure 7.6a). For that purpose, we have used the ProJet™ 3000 3D printer. After the production of the turbine blade, the wax assembly is attached (Figure 7.6b). The elements of the mould and gating system were mostly handmade and hand assembled, which implies long construction times for each mould. All the investment moulds were constructed at MICROFUSIÓN ALFA, S.L.

a) b)

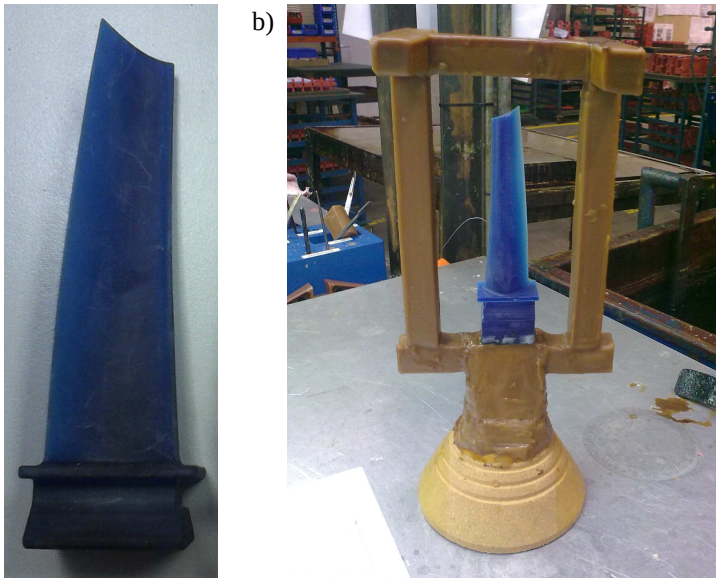

Figure 7.6. a) Wax turbine blade and b) mould design.

For the first experiments, we have selected silica as refractory because it is the material that it was available and it was sufficiently good for our first trials (Figure 7.7). We have also used colloidal silica as a binder.

Figure 7.7. Ceramic mould.

The ceramic mould has been placed inside the vacuum chamber, below the crucible. Inside the cooper crucible we have placed a billet. We have used as raw material a commercial Ti-6Al-4V alloy billet of Ø60 mm and 90 mm length.

The melting process is performed from the operator's pulpit. Before starting melting, an adequate vacuum is necessary. The furnace chamber has been evacuated to $\leq 5\ 10^{-2}$ mbar in order to reduce the risk of oxygen contamination during the melting and casting of titainum. Then, the melting of titanium is performed. Once the charge appeared to be fully molten, it is held under the selected holding power and then the titanium is tilted to the ceramic mould.

We have recorded the melting process using a UI-5240CP camera of IDS with GMHR31614MCN optic of GOYO OPTICAL INC (Figure 7.8). It is essential to filter the wavelengths near the red spectrum. For that purpose, we have used an ISP570 filter of Midpot in order to avoid that IR emission of the metal reach the sensor and saturate it. During the trials, it has not been possible to measure neither the temperature nor the efficiency nor the meniscus.

Figure 7.8. Melting of titanium.

Besides the commercial Ti-6Al-4V alloy billets, we have used titanium pucks fabricated in MU (Figure 7.9). The aid is to melt the chip generated in the workshop of MU. However, due to the bad electromagnetic coupling, it was not possible to melt these chips. In order to improve this electromagnetic coupling, we have fabricated a die in order to generate titanium pucks. These titanium pucks made of titanium chips are possible to melt.

Figure 7.9. Titanium pucks.

In the first trials, we have not used the centrifugal casting.

## 7.4 Results

The first trials performed in the installation of MU have shown the possibility to fabricate Ti-6Al-4V parts. Figure 7.10 shows some of the fabricated parts: a turbine blade and a stepped geometry. A turbine blade is a structural component while the stepped geometry is used to analyse the effect of the cooling rate in the microstructure. It can be observed in both parts that mould have been filled correctly.

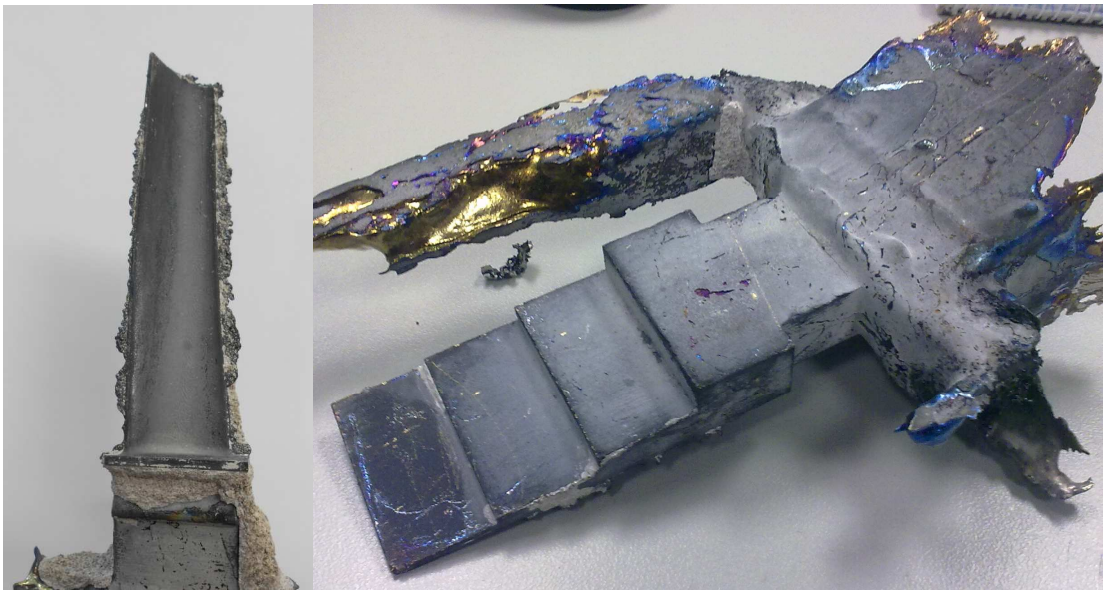

Figure 7.10. Fabricated parts.

As these parts have been cast with gravity top gated casting method, the theory predicts that they will have castings defects. However, it is not the objective of this dissertation the analysis of the microstructure and the mechanical properties. Hence, further experiments are necessary to optimize the process.

## 7.5 Conclusions

Although the installation of CCIM may seem easy, indeed we have encountered many difficulties. One of the most challenges issues of the CCIM installation is the electrical configuration. If an electrical parameter of the oscillating circuit (capacitor + transformer + power leads + coil + crucible) changes, the electrical parameter of the system have to be verified in order to ensure a correct voltage in the coil. The design of the pumping system and the cooling system do not need such rigorous dedication. The unique requisite of the pumping system is that the chiller has to be able to cool all the CCIM installation. In relation of the pumping system, the selection of the pumps depends on the vacuum level and the time to reach this vacuum level.

We have performed some experiments. The melting of the charge is not easy. An adequate heating speed is necessary in order to minimize the skull in the crucible. A highly heating speed can shorten the melting down time, but it causes splash of the melt even thermal temperature and composition homogeneity. A slow heating speed, although can avoid the shortages of high heating speed, can also cause the over evaporation loss of alloying elements. We have cast some parts using top gated gravity casting because it is the easiest way to fill the mould. The preliminary results have shown the possibility to melt Ti-6Al-4V. However, it is possible that the parts have a great amount of porosity. If it is the case, it will be necessary the use of bottom gated gravity casting method or centrifugal casting method.

We have carried out experiments using silica moulds. It is necessary the analysis of the surface layer in order to see the appearance of α-case. In case of the appearance of the α-case, a mould material with higher stability will be selected to avoid, or minimize, the reactions between the cast metal and the ceramic itself.

It would be interesting to mount an optical pyrometer on a port assembly of the vacuum chamber in order to measure the temperature and validate our numerical model.

# CHAPTER 8
# MAIN ACCOMPLISHMENTS

The main accomplishments achieved in this dissertation are:

1) Learning: I have acquired knowledge about:
    a) titanium and titanium alloys,
    b) induction furnaces,
    c) CCIM,
    d) magnetohydrodynamics,
    e) finite element method,
    f) COMSOL Multiphysics®,
    g) simulation of magnetohydrodynamics problems,
    h) simulation of induction heating problems,
    i) MATLAB®,
    j) Flow3D®, and
    k) design of investment casting moulds.
2) Scientific developments:
    a) I have used MATLAB® to simulate hydrodynamic free surface,
    b) I have developed a numerical model to simulate CCIM problem using finite element method,

c) I have developed the 2D numerical approach for free surface calculation,

d) I have set up CCIM facility, and

e) I have cast complex geometries as turbine blade using top gated gravity casting method.

3) Dissemination and transfer of knowledge:

a) I have published the following works:

- Quintana, I.; Azpilgain, Z.; Hurtado. I. "Cold crucible induction melting de aleaciones de titanio". Proceedings of the XI Congreso Nacional de Materiales, Zaragoza, 2010.

- Quintana, I.; Azpilgain, Z.; Pardo, D.; Hurtado. I; "Numerical modeling of cold crucible induction melting". Proceedings of COMSOL Conference, Stuttgart, 2011.

- Quintana, I.; Azpilgain, Z.; Pardo, D.; Hurtado. I; "Calentamiento por inducción de la aleación de aluminio A356: modelización y validación del proceso". Proceedings of the XII Congreso Nacional de Materiales, Alicante, 2012.

- Quintana, I.; Azpilgain, Z.; Pardo, D.; "Numerical Modelling of Cold Crucible Induction Melting." Metallurgical and Materials Transactions B: Process Metallurgy and Materials Processing Science (under review).

b) I have taken part in the following industry researches:

- INNOTEK : "TiCast: Fusión y colada de aleaciones de titanio de aleaciones de titanio biocompatible bajo vacío para la fabricación de piezas del sector de salud". Basque Government Industry Project: IT-2009/0000208.

- Universidad-Empresa: "CASTI: Fusión por inducción de aleaciones de titanio bajo vacío y proceso de cera perdida para la obtención de prótesis maxilofaciales". Basque Government Education, Universities, and Research Project: UE2010-2.

- Universidad-Empresa extraordinario: "SIMUFIC: Simulación multifísica del proceso de fusión por inducción". Basque Government Education, Universities, and Research Project: UE09+/111.

- GAITEK: "TITAERO: aplicaciones avanzadas de aleaciones de titanio para componentes estructurales eficientes y de alto valor añadido del sector aeronáutico". Basque Government Industry Project: IG-2012/00189.
- Universidad-Empresa: "TITAFLIGHT: Proceso de fabricación de piezas de aleaciones de titanio de alto valor añadido mediante Induction Skull Melting para el sector aeronáutico". Basque Government Education, Universities, and Research Project: UE2012-06.

CHAPTER 9

# CONCLUSIONS AND FUTURE RESEARCH

This chapter describes the conclusions of this dissertation and some ideas for the future work.

## 9.1 Concluding remarks

In the first part of this dissertation, we have performed a wide research in relation of the existing melting and casting processes of titanium, cold crucible induction melting, and the mathematical formulation of CCIM. In those chapters, we have realized that there exist a plethora of melting and casting process for titanium and its alloys. The selection of the process depends on the composition, shape, size, economics, and working factors of the parts wish to fabricate. We have selected CCIM as the most suitable melting process for the fabrication of high value added components such as turbine blades. We have also described the main features of CCIM and we have realized that the mathematical formulations of the physics that are involved in CCIM process are well-known.

In the next chapter, we have observed that there exist different methods for the numerical modelling of CCIM. Our methodology, based in the finite element method, gives correct results. We have obtained the following conclusions:

- We have developed a numerical model to simulate CCIM problem using finite element method. With some modifications, this model can be used for other magnetohydrodynamic problems.

- Comparing with other models of CCIM, our simulation method is suitable for any geometry. Moreover, the time necessary for the calculation of temperature and efficiency is relatively small.

- Results from numerical simulations show good agreement with experimental measurements.

- The 2D numerical approach for free surface calculation is formulated and it verification approves the model accuracy.

- The influence of electrical properties respect temperature are not significant.

- 3D numerical models temperature and efficiency results show good agreement with experimental measurements.

- The $k$-$\omega$ turbulence model is appropriate for CCIM problems.

- The numerical models can be used to predict the power released in the coil, crucible, and charge.

- The numerical models can be used to predict temperature in the charge.

- This model usually produces good quantitative results for the time-averaged velocity distribution.

- Influence of CCIM parameters were numerically analyzed. Results showed that when increasing the inductor current, the height of the free surface, the superheat, and the velocity in the melt increase. Increasing the frequency for a given current, the superheat increases. However, there is not a noticeable change in the meniscus height and velocity. The inductor current frequency requires further investigations. Increasing the slit thickness, the power losses in the crucible decrease and increase in the charge. Hence, there is a significant improvement of the efficiency.

- The height of the steady state meniscus contributes to flow pattern formation and vortex positional relationship.

- Large inductor currents and current frequencies magnify the non-linear effects of free surface dynamics.

- The numerical models developed are not able to describe low-frequency pulsations. The main reason is that RANS equations are unable to describe low-frequency pulsations, which arise due to the large scale flow dynamics.

- The mesh is shown to have a significant influence in the numerical results, as expected.

- The formation of inverted mesh elements and the rendering of the shape of the free surface between element edge points are the biggest challenges. For higher currents, the deformation led to inverted mesh elements and divergence of the solution. Coarser meshing made deformation for higher electric currents possible but it reduced drastically the shape resolution of the free surface drastically.

- The assumption of decoupling the electromagnetic part front the hydrodynamic and heat problem part seems to be valid.

- Unsteady 3D computer simulations are very time and resource consuming, even on modern computer systems.

In the second part of the dissertation, we have described the setting-up of the installation and the experimental work carried out. We have achieved the following conclusions:

- CCIM machine of MU is able to melt about 1 kg of titanium alloys.
- The electrical configuration is a delicate issue. If an electrical parameter of the oscillating circuit changes, the electrical parameter of the system have to be verified in order to ensure a correct voltage in the coil.
- We have cast complex geometries as a turbine blade using top gated gravity casting method.
- The charge geometry is very important for melting. Billets are easier to melt than scraps.
- The heating strategy is also important.

To summarize, in this dissertation, we have developed numerical models capable of reproducing the CCIM process parameters such as temperature and efficiency. Furthermore, we have set up a CCIM installation and we have cast Ti-6Al-4V parts.

We have shown that it is possible to melt high reactivity materials such titanium and titanium alloys using CCIM. Moreover, it is possible manufacture complex geometry parts with the use of ceramics moulds using as raw material new or recycled alloys. We have also developed numerical models capable of simulating different industrials technologies such as CCIM and induction heating. These models help to understand, develop, optimize, and control designs and processes in a cost effective way. From a scientific point of view, the numerical models developed allow for a better understanding of the magnetohydrodynamics problems. For example, they enable us to understand the influence of the magnetic fields in liquid metals.

## 9.2 Future research

This dissertation has provided new insight on the CCIM process. However, further research work is recommended in order to completely understand some open questions outlined in this dissertation. Some future works respect to the numerical modelling include:

- In the numerical models developed, the charge has been considered in liquid state. It would be very interesting to study the interaction between the melt flow and the growing mushy zone. The mushy zone, which is the transition from the purely liquid state to a complete solid state, plays an important role in the melt flow pattern. This would allow optimize the process.

- Calculation of 3D free surface (both static and dynamic) could lead to a more realistic result.
- Implementation of the buoyancy and the Marangoni effect in the numerical models in order to analyze the influence of these phenomena.
- It would be interesting the analysis of particle transport within the melt.
- The use of LES to describe the turbulence.
- Strong coupling among the electromagnetism, heat transfer, and fluids.

Regarding to experimental works, we have performed the preliminary tests. There is long way to go in order to acquire a full knowledge of the titanium casting. The next steps could include the following tasks:

- It would be interesting to measure the temperature and efficiency in order to have additional information of the process.
- Further experiments are necessary to optimize key parameters of the melting process, including: superheat of the melt, control of melt composition and possible evaporation of some elements of the alloy, reduction of skull formation, and to increase the efficiency of the process.
- It would be interesting to use a bottom gated gravity casting method or a centrifugal casting method to prove which methods deliver better results.
- It would also be interesting to analyze the α-case, the mechanical properties of the parts, and perform material characterization.
- Regarding ceramics, further experiments should be performed using different ceramics materials.

# REFERENCES


(Aguilara 2011) Aguilara, J.; Schievenbuschb, A.; Kattlitzc, O. "Qualification of a casting technology for production of titanium aluminide components for aero-engine applications". *Advanced Materials Research*, vol. 278, p. 563-568, 2011.

(Ald 2012) Ald. "Vacuum systems and technologies for". *http://web.ald-vt.de/cms/fileadmin/pdf/prospekte/ALD_Bibel_full.pdf*, 2012.

(Altindis 2011) Altindis, M.; Hagemann, K.; Polaczek, A. B.; Krupp, U. "Investigation of the effects of different types of investments on the alpha-case layer of Ti6Al7Nb castings". *Advanced Engineering Materials*, vol. 13, n. 4, p. 319-324, 2011.

(ANSYS 2013) ANSYS. *V14*, *http://www.ansys.com*, 2013.

(Aoyama 2005) Aoyama, T.; Kawamura, H.; Kotake, S.; Suzuki, Y. "Influence of containerless solidification on hardness in multifunctional titanium based alloys". *Key Engineering Materials*, vol. 297-300, p. 495-499, 2005.

(Arellano 2007) Arellano, I.; Plascencia, G.; Carrillo, E.; Barron, M. A.; Sanchez, A.; Gutierrez, J. "Design of an induction glass melting furnace by means of mathematical modelling using the finite element method". *Materials Science Forum*, vol. 553, p. 124-129, 2007.

(ASM 1988) ASM, Handbook. "ASM handbook volume 15: Casting", Ed. ASM International, 1988.

(Baake 1995) Baake, E.; Muehlbauer, A.; Jakowitsch, A.; Andree, W. "Extension of the k-ε model for the numerical simulation of the melt flow in induction crucible furnaces". *Metallurgical and Materials Transactions B: Process Metallurgy and Materials Processing Science*, vol. 26B, n. 3, p. 529-536, 1995.

(Baake 2000) Baake, E.; Nacke, B.; Jakovics, A.; Umbrashko, A. "Heat and mass transfer in turbulent flows with several recirculated flow eddies". *Proceedings of the Fourth International PAMIR Conference on Magnetohydrodynamic*, vol. 1, p. 71-6, 2000.

(Baake 2003a) Baake, E.; Nacke, B.; Bernier, F.; Vogt, M.; Muhlbauer, A.; Blum, M. "Experimental and numerical investigations of the temperature field and melt flow in the induction furnace with cold crucible". *COMPEL - The International Journal for Computation and Mathematics in Electrical and Electronic Engineering*, vol. 22, n. 1, p. 88-97, 2003.

(Baake 2003b) Baake, E.; Nacke, B.; Umbrashko, A.; Jakovics, A. "Large eddy simulation modeling of heat and mass transfer in turbulent recycled flows". *Magnetohydrodynamics*, vol. 39, n. 3, p. 291-299, 2003.

(Baake 2007) Baake, E.; Umbrashko, A.; Nacke, B.; Jakovics, A. "Simulation of turbulent metal flows". *GAMM-Mitteilungen 30*, n. 1, p. 133-148, 2007.

(Baake 2009) Baake, E.; Umbrashko, A.; Jakovics, A. "Numerical simulation and analysis of heat and mass transfer processes in metallurgical induction applications". *IEEE EUROCON 2009*, p. 1578-1583, 2009.

(Bakker 2013) Bakker, A. "Applied computational fluid dynamics". *http://www.bakker.org*, 2013.

(Bermingham 2007) Bermingham, M. J.; McDonald, S. D.; Dargusch, M. S.; StJohn, D. H. "Microstructure of cast titanium alloys". *Materials Forum*, vol. 31, p. 84-89, 2007.

(Bermudez 2005) Bermudez, A.; Rodriguez, R.; Salgado, P. "FEM for 3D eddy current problems in bounded domains subject to realistic boundary conditions.an application to metallurgical electrodes". *Archives of computational methods in engineering*, vol. 12, n. 1, p. 67-114, 2005.

(Bernier 2000) Bernier, F.; Vogt, M.; Muehlbauer, A. "Numerical calculations of the thermal behaviour and the melt flow in induction furnace with cold crucible". *Int Symp Electromagn Process Materials*, p. 283-288, 2000.

(Bhamidipati 1991) Bhamidipati, J. R.; El Kaddah, N. "Calculation of electromagnetic field and melt shape in the magnetic suspension melting process". *Magnetohydrodynamics in Process Metallurgy*, p. 69-74, 1991.

(Bhamidipati 1992) Bhamidipati, J. R.; El Kaddah, N. "Mathematical modeling of electromagnetic and heat transfer phenomena in the magnetic suspension melting process". *Vide, les Couches Minces*, n. 261, p. 19-22, 1992.

(Bhamidipati 1995) Bhamidipati, J. R.; El Kaddah, N. "Modeling of electromagnetic, fluid flow, and heat transfer phenomena in electromagnetic casting of aluminium". *Modelling of casting, welding and advanced solidification processes VII*, p. 181-188, 1995.

(Bi 1997) Bi, Y. J.; Abell, J. S. "Aluminium segregation of TiAl during single crystal growth". *Scripta Materialia*, vol. 37, n. 6, p. 743-752, 1997.

(Birben 2007) Birben, G. "Vacuum induction melting for investment casting". *Industrial Heating*, vol. 74, n. 11, p. 63-5, 2007.

(Boettinger 2000) Boettinger, W. J.; Williams, M. E.; Coriell, S. R.; Kattner, U. R.; Mueller, B. A. "Alpha case thickness modeling in investment castings". *Metallurgical and Materials Transactions B: Process Metallurgy and Materials Processing Science*, vol. 31, n. 6, p. 1419-1427, 2000.

(Boivineau 2006) Boivineau, M.; Cagran, C.; Doytier, D.; Eyraud, V.; Nadal, M. H.; Wilthan, B.; Pottlacher, G. "Thermophysical properties of solid and liquid ti-6Al-4V (TA6V) alloy". *International Journal of Thermophysics*, vol. 27, n. 2, p. 507-529, 2006.

(Bojarevics 1999a) Bojarevics, A.; Bojarevics, V.; Gelfgat, Y.; Pericleous, K. "Liquid metal turbulent flow dynamics in a cylindrical container with free surface: Experiment

and numerical analysis". *Magnetohydrodynamics*, vol. 35, n. 3, p. 205-222, 1999.

(Bojarevics 2006) Bojarevics, A.; Cramer, A.; Gelfgat, Y.; Gerbeth, G. "Experiments on the magnetic damping of an inductively stirred liquid metal flow". *Experiments in Fluids*, vol. 40, n. 2, p. 257-266, 2006.

(Bojarevics 1999) Bojarevics, V.; Pericleous, K.; Cross, M. "Dynamics of an axisymmetric electromagnetic crucible melting". *Transfer phenomena in magnetohydrodynamic and electroconducting flows*, p. 345-357, 1999.

(Bojarevics 2003a) Bojarevics, V.; Djambazov, G.; Harding, R. A.; Pericleous, K.; Wickins, M. "Investigation of the cold crucible melting process: Experimental and numerical study". *Magnetohydrodynamics*, vol. 39, n. 4, p. 395-403, 2003.

(Bojarevics 2003b) Bojarevics, V.; Pericleous, K.; Harding, R.; Wickins, M. "Induction skull-melting dynamics for different materials: Numerical modeling and comparisons with experiments". *Modelling of casting, welding and advanced solidification processes X*, p. 591-598, 2003.

(Bojarevics 2004) Bojarevics, V.; Harding, R. A.; Pericleous, K.; Wickins, M. "The development and experimental validation of a numerical model of an induction skull melting furnace". *Metallurgical and Materials Transactions B: Process Metallurgy and Materials Processing Science*, vol. 35, n. 4, p. 785-803, 2004.

(Bojarevics 2011) Bojarevics, V.; Roy, A.; Pericleous, K. "Numerical model of electrode induction melting for gas atomization". *COMPEL - The International Journal for Computation and Mathematics in Electrical and Electronic Engineering*, vol. 30, n. 5, p. 1455-1466, 2011.

(Campbell 1991) Campbell, J. "Castings", Ed. Elsevier, 1991.

(Carin 2012) Carin, M. "Square drop oscillation under surface tension". *www.comsol.com*, 2012.

(Choudhury 1996) Choudhury, A.; Blum, M. "Economical production of titanium-aluminide automotive valves using cold wall induction melting and centrifugal casting in a permanent mold". *Vacuum*, vol. 47, n. 6-8, p. 829-831, 1996.

(Choudhury 1997) Choudhury, A.; Blum, M.; Jarczyk, G.; Scholz, H.; Busse, P. "Low cost production of TiAl automotive valves using cold wall induction melting and permanent mold centrifugal casting". *Proceedings of the TMS Fall Meeting*, p. 259-269, 1997.

(Cingoski 1994) Cingoski, V.; Yamashita, H. "Analysis of induction skull melting furnace by edge finite element method excited from voltage source". *IEEE Transactions on Magnetics*, vol. 30, p. 3459-3462, 1994.

(CMP 1987) CMP. "Vacuum induction melting technology: A unique electrical method for production of high quality and reliable alloys needed in critical applications". *http://infohouse.p2ric.org/ref/09/08921.pdf*, 1987.

(COMSOL 2013) COMSOL. *V4.3. documentation*, *www.comsol.com*, 2013.

(Cruz 2005) Cruz, R. V. B.; Sayeg, I. J.; Mutarelli, P. S.; Pinedo, C. E. "Effect of the ceramic mould composition on the surface quality of as-cast titanium alloy". *Journal of Materials Science*, vol. 40, n. 22, p. 6041-6043, 2005.

(Da Rocha 2005) Da Rocha, S. S.; Adabo, G. L.; Vaz, L. G.; Henriques, G. E. P. "Effect of thermal treatments on tensile strength of commercially cast pure titanium and ti-6Al-4V alloys". *Journal of Materials Science: Materials in Medicine*, vol. 16, n. 8, p. 759-766, 2005.

(Davidson 2001) Davidson, P. A. "An introduction to magnetohydrodynamics", Cambridge University Press, 2001.

(Delage 1981) Delage, D.; Ernst, R.; Driole, J. "Theoretical study of heating by induction to calculate electrical orders of grandeur of a cloud crucible system". *IEEE Industry Applications Society*, p. 957-961, 1981.

(Delage 1983) Delage, D.; Ernst, R. "Modelisation electrique d'un systeme de fusion par induction en creuset froid". *Revue Generale de l'Electricite*, p. 266-272, 1983.

(Delage 1984) Delage, D.; Ernst, R.; Driole, J. "Induction melting cold crucible". *Metallurgical Applications of Magnetohydrodynamics, Proceedings of a Symposium of the International Union of Theoretical and Applied Mechanics*, p. 108-119, 1984.

(Dlouhy 2003) Dlouhy, A.; Zemecik, L.; Valek, R. "Near-gamma TiAl investment casting and its optimization". *Gamma Titanium Aluminides*, p. 291-296, 2003.

(El Kaddah 1983) El Kaddah, N.; Szekely, J. "The turbulent recirculating flow field in a coreless induction furnace, a comparison of theoretical predictions with measurements". *Journal of Fluid Mechanics*, vol. 133, p. 37-46, 1983.

(Enokizono 1993) Enokizono, M.; Todaka, T.; Matsumoto, I.; Wada, Y. "Levitation-melting apparatus with flux concentration cap". *IEEE Transactions on Magnetics*, vol. 29, n. 6, p. 2968-2970, 1993.

(Ernst 2009) Ernst, R.; Dumont, M.; Petitpas, P. "Recent progresses in optimizing inductive cold crucible processes". *6th. Int. Conf. on EPM-2009*, p. 513-516, 2009.

(Fautrelle 2009) Fautrelle, Y.; Ernst, R.; Moreau, R. "Magnetohydrodynamics applied to materials processing". *International Journal of Materials Research*, vol. 100, n. 10, p. 1389-1398, 2009.

(Felten 2004) Felten, F.; Fautrelle, Y.; Du Terrail, Y.; Metais, O. "Numerical modelling of electromagnetically-driven turbulent flows using LES methods". *Applied Mathematical Modelling*, vol. 28, n. 1, p. 15-27, 2004.

(FLOW-3D 2013) FLOW-3D. *V10.1*, http://www.flow3d.com/, 2013.

(Frueh 1997) Frueh, C.; Poirier, D. R.; Maguire, M. C. "Effect of silica-containing binders on the titanium/face coat reaction". *Metallurgical and Materials Transactions B: Process Metallurgy and Materials Processing Science*, vol. 28, n. 5, p. 919-926, 1997.

(Fukumoto 1991) Fukumoto, H.; Hosokawa, Y.; Ayata, K.; Morishita, M. "Numerical simulation of meniscus shape considering internal flow effects". *Proceedings of a Symposium on Magnetohydrodynamics in Process Metallurgy*, p. 21-26, 1991.

(Gagnoud 1985) Gagnoud, A.; Delage, D.; Garnier, M. "Electromagnetic modelization of cold crucibles". *Progress in Astronautics and Aeronautics*, vol. 100, p. 634-651, 1985.

(Gagnoud 1988) Gagnoud, A.; Etay, J.; Garnier, M. "Levitation melting process using cold crucible technique". *Transactions of the Iron and Steel Institute of Japan*, vol. 28, n. 1, p. 36-40, 1988.

(Gagnoud 1991) Gagnoud, A.; Maestrali, B.; Masse, P. "Modelling of motion in liquid metal limited by a free surface and a solidification front". *European Journal of Mechanics, B/Fluids*, vol. 10, n. 5, p. 552-562, 1991.

(Gombert 2003) Gombert, D.; Richardson, J. R. "Cold-crucible induction melter design and development". *Nuclear Technology*, vol. 141, n. 3, p. 301-308, 2003.

(Gomes 2011) Gomes, F.; Puga, H.; Barbosa, J.; Ribeiro, C. S. "Effect of melting pressure and superheating on chemical composition and contamination of yttria-coated ceramic crucible induction melted titanium alloys". *Journal of Materials Science*, vol. 46, n. 14, p. 4922-4936, 2011.

(Gomes 2013) Gomes, F.; Barbosa, J.; Ribeiro, C. S. "Aluminium evaporation during ceramic crucible induction melting of titanium aluminides". *Materials Science Forum Vols.*, vol. 730-732, p. 697-702, 2013.

(Gross 1999) Gross, C.; Assmus, W.; Muiznieks, A.; Raming, G.; Muehlbauer, A.; Stenzel, C. "Power consumption of skull melting, part I: Analytical aspects and experiments". *Crystal Research and Technology*, vol. 34, n. 3, p. 319-328, 1999.

(Guillemot 2004) Guillemot, F.; Prima, F.; Bareille, R.; Gordin, D.; Gloriant, T.; Porte-Durrieu, M. C.; Ansel, D.; Baquey, C. "Design of new titanium alloys for orthopaedic applications". *Medical & Biological Engineering & Computing*, vol. 42, n. 1, p. 137-141, 2004.

(Guo 1999) Guo, J.; Su, Y.; Liu, Y.; Ren, Z.; Jia, J. "Optimization of processing parameters during ISM process of ti-15-3". *Transactions of Nonferrous Metals Society of China (English Edition)*, vol. 9, n. 1, p. 17-21, 1999.

(Guo 2000) Guo, J.; Liu, Y.; Su, Y.; Ding, H.; Jia, J. "Skull formation and change during ISM process of ti-15-3 alloy". *Transactions of Nonferrous Metals Society of China (English Edition)*, vol. 10, n. 1, p. 14-18, 2000.

(Guo 2005) Guo, J.; Liu, G.; Su, Y.; Ding, H.; Jia, J.; Fu, H. "Skull variation during the induction skull melting processing of γ-TiAl alloy". *Materials Science Forum*, vol. 475-479, p. 809-812, 2005.

(Harding 2001) Harding, R. A.; Wickins, M.; Li, Y. G. "Progress towards the production of high quality γ-TiAl castings". *Structural Intermetallics*, p. 181-189, 2001.

(Harding 2003) Harding, R. A.; Wickins, M. "Temperature measurements during induction skull melting of titanium aluminide". *Materials Science and Technology*, vol. 19, n. 9, p. 1235-1246, 2003.

(Harding 2004) Harding, R. A. "Recent developments in the induction skull melting and investment casting of titanium aluminides". *Kovove materialy*, vol. 42, p. 225-241, 2004.

(Harding 2005) Harding, R. A.; Wickins, M.; Keough, G.; Roberts, R. J.; Pericleous, K.; Bojarevics, V. "The use of combined DC and AC fields to increase superheat in an induction skull melting furnace". *LMPC 2005 - Proceedings of the 2005 International Symposium on Liquid Metal Processing and Casting*, vol. 2005, p. 201-210, 2005.

(Harding 2006) Harding, R. "Towards more reliable investment casting". *International Journal of Cast Metals Research*, vol. 19, n. 5, p. 289-301, 2006.

(Harding 2011) Harding, R. A.; Wickins, M.; Wang, H.; Djambazov, G.; Pericleous, K. A. "Development of a turbulence-free casting technique for titanium aluminides". *Intermetallics*, vol. 19, n. 6, p. 805-813, 2011.

(Hero 1993) Hero, H.; Syverud, M.; Waarli, M. "Porosity and mould filling of titanium castings". *Journal of Materials Science: Materials in Medicine*, vol. 4, n. 3, p. 296-299, 1993.

(Hongsheng 2005) Hongsheng, D.; Ruirun, C.; Jingjie, G.; Weisheng, B.; Daming, X.; Hengzhi, F. "Directional solidification of titanium alloys by electromagnetic confinement in cold crucible". *Materials Letters*, vol. 59, n. 7, p. 741-745, 2005.

(Hung 2003) Hung, C. C.; Hou, G. L.; Tsai, C. C.; Huang, C. C. "Effect of zirconia-modified magnesia investment on the casting of pure titanium". *The Kaohsiung Journal of Medical Sciences*, vol. 19, n. 3, p. 121-125, 2003.

(Hung 2004) Hung, C. C.; Hou, G. L.; Tsai, C. C.; Huang, C. C. "Pure titanium casting into zirconia-modified magnesia-based investment molds". *Dental Materials*, vol. 20, n. 9, p. 846-851, 2004.

(Ida 1982) Ida, K.; Togaya, T.; Tsutsumi, S.; Takeuchi, M. "Effect of magnesia investments in the dental casting of pure titanium or titanium alloys". *Dental Materials Journal*, vol. 1, n. 1, p. 8-21, 1982.

(Iiyama 2009) Iiyama, K.; Doi, H.; Hanawa, T. "Effect of mold temperature on the mechanical durability of titanium casting clasp model". *Dental Materials Journal*, vol. 28, n. 5, p. 610-619, 2009.

(Iwai 1995) Iwai, K.; Asai, S. "Effect of design parameters on the magnetic field distribution around a cold crucible and the heat generation rate in it". *Modelling and Simulation in Materials Science and Engineering*, vol. 3, n. 4, p. 473-484, 1995.

(Jha 2008) Jha, M. N.; Sahashrabuddhe, S. N.; Murthy, P. S. S.; Bapat, A. V.; Das, A. K. "450 kW plasma melting system". *Journal of Physics: Conference Series*, vol. 114, p. 1-11, 2008.

(Jia 2006) Jia, Q.; Cui, Y. Y.; Yang, R. "A study of two refractories as mould materials for investment casting TiAl based alloys". *Journal of Materials Science*, vol. 41, n. 10, p. 3045-3049, 2006.

(Jingjie 2002) Jingjie, G.; Guizhong, L.; Yanqing, S.; Hongsheng, D.; Jun, J.; Hengzhi, F. "The critical pressure and impeding pressure of al evaporation during induction skull melting processing of TiAl". *Metallurgical and Materials Transactions A (Physical Metallurgy and Materials Science)*, vol. 33A, n. 10, p. 3249-3253, 2002.

(Jones 2003) Jones, S.; Yuan, C. "Advances in shell moulding for investment casting". *Journal of Materials Processing Technology*, vol. 135, p. 258-265, 2003.

(Jouan 1996) Jouan, A.; Moncouyoux, J. P.; Merlin, S.; Roux, P. "Multiple applications of cold crucible melting". *Radwaste Magazine*, vol. 3, n. 2, p. 77-81, 1996.

(Jovanovic 2006) Jovanovic, M. T.; Tadic, S.; Zec, S.; Miskovic, Z.; Bobic, I. "The effect of annealing temperatures and cooling rates on microstructure and mechanical

properties of investment cast ti-6Al-4V alloy". *Materials and Design*, vol. 27, n. 3, p. 192-199, 2006.

(Kampe 1994) Kampe, S. L.; Sadler, P.; Christodoulou, L.; Larsen, D. E. "Room-temperature strength and deformation of $TiB_2$-reinforced near-γ titanium aluminides". *Metallurgical and Materials Transactions A (Physical Metallurgy and Materials Science)*, vol. 25A, n. 10, p. 2181-2197, 1994.

(Kawase 1993) Kawase, Y.; Yamaguchi, T.; Hayashi, N. "3-D finite element analysis for molten metal shapes in an electromagnetic melting system". *IEEE Transactions on Magnetics*, vol. 29, n. 2, p. 1554-1557, 1993.

(Keller 1997) Keller, M. M.; Jones, P. E.; Porter, W. J. I.; Eylon, D. "Development of low-cost TiAl automotive valves". *JOM*, vol. 49, n. 5, p. 42-44, 1997.

(Kikuchi 2001) Kikuchi, H.; Onouchi, M.; Hsu, H. C.; Kurotani, T.; Nishiyama, M. "Titanium casting: The surface reaction layer of castings obtained using ultra low temperature molds". *Journal of Oal Science*, vol. 43, n. 1, p. 27-33, 2001.

(Kim 2002) Kim, M. G.; Kim, Y. J. "Investigation of interface reaction between TiAl alloys and mold materials". *Metals and materials international*, vol. 8, n. 3, p. 289-293, 2002.

(Kim 2007) Kim, B. H.; Shin, J. S.; Lee, S. M.; Moon, B. M. "The effect of crucible configuration on joule and pinch effects in EMCC process of silicon". *Materials Science Forum*, vol. 539-543, p. 3179-3183, 2007.

(Kirpo 2008) Kirpo, M. "Modeling of turbulence properties and particle transport in recirculated flows". Ph.D. Thesis, University of Latvia, Riga, 2008.

(Kostov 2005) Kostov, A.; B.Friedrich, B. "Selection of crucible oxides in molten titanium and titanium aluminum alloys by thermo-chesmistry calculations". *Mining and Metallurgy*, vol. 41, p. 113-125, 2005.

(Kuang 2001) Kuang, J. P.; Harding, R. A.; Campbell, J. "A study of refractories as crucible and mould materials for melting and casting gamma-tial alloys". *International Journal of Cast Metals Research*, vol. 13, p. 277-292, 2001.

(Kudrman 2007) Kudrman, J.; Fousek, J.; Brezina, V.; Míková , R.; Veselì, J. "Titanium alloys for implants in medicine". *Kovove materialy*, vol. 45, p. 199-208, 2007.

(Larsen 1996) Larsen, D. E. J. "Status of investment cast gamma titanium aluminides in the USA". *Materials Science & Engineering A: Structural Materials: Properties, Microstructure and Processing*, vol. A213, n. 1-2, p. 128-133, 1996.

(Launder 1974) Launder, B. E.; Spalding, D. B. "The numerical computation of turbulent flows". *Computer Methods in Applied Mechanics and Engineering*, vol. 3, n. 2, p. 269-289, 1974.

(Lavers 1988a) Lavers, J. D.; Ahmed, M. R. "A boundary element method to predict the shape of a molten metal free surface in EM confinement field". *IEEE Transactions on Magnetics*, vol. 24, n. 6, p. 2521-2523, 1988.

(Lavers 1988b) Lavers, J. D.; Ahmed, M. R. "Mathematical modeling of electromagnetic confinement". *Casting of Near Net Shape Products*, p. 395-410, 1988.

(Lavers 1989) Lavers, J. D. "Computational methods for the analysis of molten metal electromagnetic confinement systems". *ISIJ Int*, vol. 29, n. 12, p. 993-1005, 1989.

(Lavers 2008) Lavers, J. D. "State of the art of numerical modeling for induction processes". *COMPEL: The International Journal for Computation and Mathematics in Electrical and Electronic Engineering*, vol. 27, n. 2, p. 335-349, 2008.

(Li 1991) Li, B. O.; Evans, J. W.; Cook, D. P. "Improved mathematical model for electromagnetic casters and testing by a physical model". *Metallurgical transactions.B, Process metallurgy*, vol. 22, n. 1, p. 121-134, 1991.

(Li 1993) Li, B. Q. "The magnetothermal phenomena in electromagnetic levitation processes". *International Journal of Engineering Science*, vol. 31, n. 2, p. 201-220, 1993.

(Li 1994) Li, B. Q. "The transient magnetohydrodynamic phenomena in electromagnetic levitation processes". *International Journal of Engineering Science*, vol. 32, n. 8, p. 1315-1336, 1994.

(Li 2010) Li, C.; Wang, H.; Wu, S.; Xu, L.; Wang, K.; Fu, H. "Research on mould filling and solidification of titanium alloy in vertical centrifugal casting". *Xiyou Jinshu Cailiao Yu Gongcheng/Rare Metal Materials and Engineering*, vol. 39, n. 3, p. 388-392, 2010.

(Lin 1999) Lin, K. F.; Lin, C. C. "Interfacial reactions between ti-6Al-4V alloy and zirconia mold during casting". *Journal of Materials Science*, vol. 34, n. 23, p. 5899-5906, 1999.

(Lütjering 2007) Lütjering, G.;Willians. J.C. "Titanium", Ed. Springer Berlin Heidelberg, 2007.

(MATLAB 2012) MATLAB. *R2012a*, *http://www.mathworks.es/*, 2012.

(Mills 2002) Mills, K. C. "Recommended values of thermophysical properties for selected commercial alloys", Ed. National Physical Laboratory, 2002.

(Mitchell 1992) Mitchell, A. "Melting and refining of superalloys and titanium alloys". *ISIJ International*, vol. 32, n. 5, p. 557-562, 1992.

(Mitchell 1994) Mitchell, A. "Recent developments in specialty melting processes". *Materials Technology*, vol. 9, n. 9-10, p. 201-206, 1994.

(Mitchell 2009) Mitchell, A.; Reed, R. C. "The influence of remelting processes on the mechanical properties of forged alloys". *High Temperature Materials and Processes*, vol. 28, n. 5, p. 285-297, 2009.

(Miyakawa 1989) Miyakawa, O.; Watanabe, K.; Okawa, S.; Nakano, S.; Kobayashi, M.; Shiokawa, N. "Layered structure of cast titanium surface". *Dental Materials Journal*, vol. 8, n. 2, p. 175-185, 1989.

(Mohammadi 2001) Mohammadi, S.; Esposito, M.; Wictorin, L.; Aronsson, B. O.; Thomsen, P. "Bone response to machined cast titanium implants". *Journal of Materials Science*, vol. 36, n. 8, p. 1987-1993, 2001.

(Mueller 2005) Mueller, B. "Investment casting trends". *Advanced Materials & Processes*, vol. 163, n. 3, p. 30-32, 2005.

(Muiznieks 1999) Muiznieks, A.; Raming, G.; Muehlbauer, A.; Gross, C.; Assmus, W.; Stenzel, C. "Power consumption of skull melting, part II: Numerical calculation of the shape of the molten zone and comparison with experiment". *Crystal Research and Technology*, vol. 34, n. 3, p. 329-338, 1999.

(Muraleedharan 1996) Muraleedharan, K.; Rishel, L. L.; De Graef, M.; Cramb, A. W.; Pollock, T. M.; Gray III, G. T. "The effect of cooling rate during casting on microstructural development in ti-48Al-2Cr-2Nb type alloys". *Structural Intermetallics 1997. Proceedings of the Second International Symposium on Structural Intermetallics*, p. 215-224, 1996.

(Nastac 2006) Nastac, L.; Gungor, M. N.; Ucok, I.; Klug, K. L.; Tack, W. T. "Advances in investment casting of ti-6Al-4V alloy: A review". *International Journal of Cast Metals Research*, vol. 19, n. 2, p. 73-93, 2006.

(Nelson 1992) Nelson, O. E. "Advances in cost effective processing of titanium". *Key Engineering Materials*, vol. 77-78, p. 103-114, 1992.

(Niinomi 2003a) Niinomi, M. "Titanium alloys for medical and dental applications". *Medical Device Materials - Proceedings of the Materials and Processes for Medical Devices Conference 2003*, p. 417-422, 2003.

(Niinomi 2003b) Niinomi, M. "Recent research and development in titanium alloys for applications and healthcare goods". *Science and Technology of Advanced Materials*, vol. 4, n. 5, p. 445-454, 2003.

(Niinomi 2007) Niinomi, M. "Recent research and development in metallic materials for biomedical, dental and healthcare products applications". *Materials Science Forum*, vol. 539-543, p. 193-200, 2007.

(Niinomi 2008) Niinomi, M. "Mechanical biocompatibilities of titanium alloys for biomedical applications". *Journal of the Mechanical Behavior of Biomedical Materials*, vol. 1, n. 1, p. 30-42, 2008.

(Nikiforova 1984) Nikiforova, N. V.; Pavlov, S. I.; Tir, L. L. "Calculation of electromagnetic, hydrodynamic, and energy characteristics of induction furnace with cold crucible on basis of two-dimensional model". *Magnetohydrodynamics*, vol. 20, n. 2, p. 191-199, 1984.

(Nikiforova 1990) Nikiforova, N. V.; Pavlov, S. I.; Tir, L. L.; Yakovich, A. T. "Numerical determination of melt circulation in an induction furnace with segmented conducting crucible involving the utilization of a meridional section model". *Magnetohydrodynamics (English translation of Magnitaya Gidrodinamika)*, vol. 26, n. 2, p. 215-221, 1990.

(Niu 2012) Niu, H. Z.; Xiao, S. L.; Kong, F. T.; Zhang, C. J.; Chen, Y. Y. "Microstructure characterization and mechanical properties of $TiB_2$/TiAl in situ composite by induction skull melting process". *Materials Science and Engineering A*, vol. 532, p. 522-527, 2012.

(Oliveira 2006) Oliveira, P. C. G.; Adabo, G. L. Ribeiro, R. F.; Rocha, S. S. "The effect of mold temperature on castability of CP ti and ti-6Al-4V castings into phosphate bonded investment materials". *Dental Materials*, vol. 22, n. 12, p. 1098-1102, 2006.

(Onishi 1992) Onishi, A.; Etay, J. "Numerical calculation of the free surfaces of a liquid metal domain controlled by an alternating magnetic field in presence of solid boundaries". *Engineering Analysis with Boundary Elements*, vol. 10, n. 3, p. 225-229, 1992.

(Papadopoulos 1999) Papadopoulos, T.; Zinelis, S.; Vardavoulias, M. "Metallurgical study of the contamination zone at the surface of dental ti castings, due to the phosphate-bonded investment material: The protection efficacy of a ceramic coating". *Journal of Materials Science*, vol. 34, n. 15, p. 3639-3646, 1999.

(Papadopoulos 2009) Papadopoulos, T. D.; Spyropoulos, K. D. "The effect of a ceramic coating on the cpTi-porcelain bond strength". *Dental Materials*, vol. 25, n. 2, p. 247-253, 2009.

(Pei-Ling 2011) Pei-Ling, L.; Wen-Cheng, C.; Jen-Chyan, W.; Ta-Ko, H.; Chun-Cheng, H. "A newly developed calcia/titanium modified magnesia-based investment mold for titanium casting". *Materials Science & Engineering: C (Materials for Biological Applications)*, vol. 31, n. 2, p. 144-150, 2011.

(Pericleous 1997) Pericleous, K.; Bojarevics, V.; Cross, M.; Tinios, G. "The development of dynamic CFD model of the magnetic semi levitation of liquids metals". *Proc. Int. Conference on Computational Fluid Dynamics in Mineral & Metal Procesing and Power Generation*, p. 55-62, 1997.

(Pericleous 2001) Pericleous, K. A. "Computing the dynamic interaction of magnetic fields and turbulent conducting fluids in metals processing". *Computational modeling of materials, minerals and metals processing*, p. 5-22, 2001.

(Peters 1996) Peters, D. M. "Casting titanium at duriron". *Foundry Management & Technology*, vol. 124, n. 10, p. 3, 1996.

(Reed 1990) Reed, D. S. "Induction skull melting of titanium aluminides and other reactive metals". *Industrial Heating*, vol. 57, n. 1, p. 20-23, 1990.

(Reed 2003) Reed, S.; Narayan, J. "Investment casting of titanium". *Foundry Trade Journal*, vol. 177, n. 3610, p. 24-26, 2003.

(Reed 2004) Reed, S.; Narayan, J. "Investment casting of titanium using the induction skull melting process". *Aluminium International Today*, vol. 16, n. 3, p. 7-8, 2004.

(Renjie 2010) Renjie, C.; Ming, G.; Hu, Z.; Shengkai, G. "Interactions between TiAl alloys and yttria refractory material in casting process". *Journal of Materials Processing Technology*, vol. 210, n. 9, p. 1190-1196, 2010.

(Riemer 2011) Riemer, B.; Lange, E.; Hameyer, K. "Investigation of the skull melting method for the generation of particulate material of inorganic compounds". *Archives of Electrical Engineering*, vol. 60, n. 2, p. 197-209, 2011.

(Ruirun 2012) Ruirun, C.; Jieren, Y.; Hongsheng, D.; Feng, H.; Yanqing, S.; Jingjie, G.; Hengzhi, F. "Effect of power parameter and induction coil on magnetic field in cold crucible during continuous melting and directional solidification". *China Foundry*, vol. 9, n. 1, p. 15-19, 2012.

(Sakamoto 1992) Sakamoto, K.; Yoshikawa, K.; Kusamichi, T.; Onoye, T. "Changes in oxygen contents of titanium aluminides by vacuum induction, cold crucible induction and electron beam melting". *ISIJ International*, vol. 32, n. 5, p. 616-624, 1992.

(Sakane 1988) Sakane, J.; Li, B.; Evans, J. W. "Mathematical modeling of meniscus profile and melt flow in electromagnetic casters". *Metallurgical Transactions B*, vol. 19, n. 3, p. 397-408, 1988.

(Semiatin 2004) Semiatin, S. L.; Ivanchenko, V. G.; Akhonin, S. V.; Ivasishin, O. M. "Diffusion models for evaporation losses during electron-beam melting of alpha/beta-

titanium alloys". *Metallurgical and Materials Transactions B: Process Metallurgy and Materials Processing Science*, vol. 35, n. 2, p. 235-245, 2004.

(Si-Young 2007) Si-Young, S.; Young-Jig, K. "Melting and casting of titanium alloys". *Materials Science Forum*, vol. 539-543, p. 3601-3606, 2007.

(Sneyd 1982) Sneyd, A. D.; Moffatt, H. K. "Fluid dynamical aspects of the levitation-melting process". *Journal of Fluid Mechanics*, vol. 117, p. 45-70, 1982.

(Spitans 2010) Spitans, S.; Jakovics, A.; Baake, E.; Nacke, B. "Numerical modelling of free surface dynamics of melt in induction crucicble furnace". *Magnetohydrodynamics*, vol. 46, n. 4, p. 317-328, 2010.

(Spitans 2013) Spitans, S.; Jakovics, A.; Baake, E.; Nacke, B. "Numerical modeling of free surface dynamics of melt in an alternate electromagnetic field: Part I. implementation and verification of model". *Metallurgical and Materials Transactions B: Process Metallurgy and Materials Processing Science*, vol. 44, n. 3, p. 593-605, 2013.

(Su 2005) Su, Y.; Liu, G.; Peng, J.; Guo, J.; Jia, J.; Fu, H. "Melting throughout time and energy consumption for TiAl alloys during ISM process". *Transactions of the Nonferrous Metals Society of China*, vol. 15, n. 1, p. 1-6, 2005.

(Sugilal 2007) Sugilal, G.; Sengar, P. B. S.; Misra, S. D. "Cold crucible induction melter: Technology development for HLW vitrification". *Barc newsletter*, n. 276, p. 14-22, 2007.

(Sung 2007) Sung, S.; Choi, B.; Noh, S.; Hahn, C.; Ryu, Y.; Han, B.; Kim, Y. "Thermodynamic calculation of alpha-case formation in titanium alloys". *Advanced Materials Research*, vol. 26-28, p. 519-522, 2007.

(Sung 2008) Sung, S. Y.; Choi, B. J.; Han, B. S.; Oh, H. J.; Kim, Y. J. "Evaluation of alpha-case in titanium castings". *Journal of Materials Science and Technology*, vol. 24, n. 1, p. 70-74, 2008.

(Suzuki 1997) Suzuki, K. i.; Nishikawa, K.; Watakabe, S. "Stability of yttria for titanium alloy precision casting mold". *Materials Transactions, JIM*, vol. 38, n. 1, p. 54-62, 1997.

(Suzuki 2003) Suzuki, K.; Watakabe, S. "Melting and precision casting of ti-6Al-4V alloy by use of electron beam furnace". *Metals and materials international*, vol. 9, n. 4, p. 359-367, 2003.

(Tanaka 1991) Tanaka, T.; Kurita, K.; Kuroda, A. "Mathematical modelling for electromagnetic field and shaping of melts in a cold crucible". *ISIJ International*, vol. 31, n. 4, p. 350-357, 1991.

(Tarapore 1976) Tarapore, E. D.; Evans, J. W. "Fluid velocities in induction melting furnaces. I. theory and laboratory experiments". *Metallurgical Transactions B (Process Metallurgy)*, vol. 7B, n. 3, p. 343-351, 1976.

(Tarapore 1977) Tarapore, E. D.; Evans, J. W.; Langfeldt, J. "Fluid velocities in induction melting furnaces. II. large scale measurements and predictions". *Metallurgical Transactions B (Process Metallurgy)*, vol. 8B, n. 1, p. 179-184, 1977.

(Tetsui 2011) Tetsui, T. "Manufacturing technology for gamma-TiAl alloy in current and future applications". *Rare Metals*, vol. 30, p. 294-299, 2011.

(Tir 1984) Tir, L. L.; Gubchenko, A. P.; Prostyakov, A. A.; Brutskus, Y. "Increasing the technical and economic indexes of induction furnaces with a cold crucible". *Soviet Electrical Engineering*, vol. 55, n. 2, p. 37-41, 1984.

(Tsutsumi 2010) Tsutsumi, H.; Niinomi, M.; Akahori, T.; Nakai, M.; Takeuchi, T.; Katsura, S. "Mechanical properties of a β-type titanium alloy cast using a calcia mold for biomedical applications". *Materials Transactions*, vol. 51, n. 1, p. 136-142, 2010.

(Umbrashko 2005) Umbrashko, A.; Baake, E.; Nacke, B.; Jakovics, A. "Experimental investigations and numerical modelling of the melting process in the cold crucible". *COMPEL - The International Journal for Computation and Mathematics in Electrical and Electronic Engineering*, vol. 24, n. 1, p. 314-323, 2005.

(Umbrashko 2006) Umbrashko, A.; Baake, E.; Nacke, B.; Jakovics, A. "Modeling of the turbulent flow in induction furnaces". *Metallurgical and Materials Transactions B: Process Metallurgy and Materials Processing Science*, vol. 37, n. 5, p. 831-838, 2006.

(Umbrasko 2008) Umbrasko, A.; Baake, E.; Nacke, B.; Jakovics, A. "Thermal and hydrodynamic analysis of the melting process in the cold crucible using 3D modeling". *Heat Transfer Research*, vol. 39, n. 5, p. 413-421, 2008.

(Versteeg 2007) Versteeg, H. K.; Malalasekera, W. "An introduction to computational fluid dynamics", Ed. Pearson Education Limited, 2007.

(Wang 2011) Wang, H.; Djambazov, G.; Pericleous, K. "Numerical study of crucial parameters in tilt casting for titanium aluminides". *China Foundry*, vol. 8, n. 3, p. 274-281goo, 2011.

(Wang 2012) Wang, H.; Djambazov, G.; Pericleous, K.; Harding, R. A.; Wickins, M. "Numerical modelling of tilt casting process for γ-TiAL alloys". *International Journal of Cast Metals Research*, vol. 25, n. 2, p. 65-74, 2012.

(Westphal 1995) Westphal, E.; Muehlbauer, A.; Muiznieks, A.; Virbulis, J. "Study of the heat fluxes in an induction furnace with cold crucible". *Advances in Engineering Heat Transfer*, p. 471-480, 1995.

(Wetzel 2008) Wetzel, S. "The hip, knee, elbow, toe and shoulder movement". *Modern Casting*, vol. 98, n. 3, p. 38-41, 2008.

(Widlund 2000) Widlund, O. "Modeling of magnetohydrodynamic turbulence". Ph.D. Thesis, Royal Institute Of Technology, Stockholm, 2000.

(Wilcox 1998) Wilcox, D. C. " Turbulence modeling for CFD", Ed. DCW Industries, La Canada, CA, 1998.

(Xhu 1996) Xhu, Z. R.; Harding, R. A.; Campbell, J.; Lavers, J. D. "Electromagnetic field and Lorentz force calculations in an induction furnace". *Software for Electrical Engineering Analysis and Design*, p. 395-404, 1996.

(Xue 2009) Xue, G.; Wang, T.; Su, Y.; Cai, S.; Xu, J.; Li, J.; Guo, J.; Li, T. "Numerical simulation of thermal and flow fields in induction skull melting process". *Xiyou Jinshu Cailiao Yu Gongcheng/Rare Metal Materials and Engineering*, vol. 38, n. 5, p. 761-765, 2009.

(Yanqing 2001) Yanqing, S.; Yuan, L.; Jingjie, G.; Guizhong, L.; Daming, X.; Jun, J. "Molding of temperature field for the induction skull melting process of ti-47Ni-nb". *Metallurgical and Materials Transactions A (Physical Metallurgy and Materials Science)*, vol. 32A, n. 11, p. 2895-2902, 2001.

(Yasuda 2007) Yasuda, H. "Applications of High Magnetic Fields in Materials Processing". *Magnetohydrodynamics – Historical Evolution and Trends*, Ed. Springer, vol. 80, p. 357-374, 2007.

(Yongliang 2008) Yongliang, G.; Shulong, X.; Lijuan, X. "Numerical simulation of process of cavity filling and solidifying in TiAl alloy investment casting". *Materials Science Forum*, vol. 575-578, p. 1489-1494, 2008.

(Yu 2010) Yu, G.; Li, N.; Li, Y.; Wang, Y. "Study on surface reaction layer of titanium cast with $Al_2O_3$-based investment materials". vol. 97-101, p. 1029-1032, 2010.

(Zanner 2004) Zanner, F. J. "Vacuum melting", Ed. Elsevier, 2004.

(Zhao 2011) Zhao, E. T.; Kong, F. T.; Chen, Y. Y.; Li, B. H. "Interfacial reactions between ti-1100 alloy and ceramic mould during investment casting". *Transactions of Nonferrous Metals Society of China (English Edition)*, vol. 21, p. s348-s352, 2011.

(Zhu 1999) Zhu, X. R.; Harding, R. A.; Campbell, J. "Electromagnetic confinement including the dynamic effect due to melt flow". *ISIJ International*, vol. 39, n. 1, p. 1-9, 1999.

(Zinelis 2000) Zinelis, S. "Effect of pressure of helium, argon, krypton, and xenon on the porosity, microstructure, and mechanical properties of commercially pure titanium castings". *The Journal of Prosthetic Dentistry*, vol. 84, n. 5, p. 575-582, 2000.